ChemSusChem

Chemistry Europe
European Chemical Societies Publishing
ChemSusChem

REVIEW

Recent Progress in Prussian Blue Analog Nanomaterials: Structural Engineering and Functional Applications

Ke Wu[1,2] | Guangxun Zhang[1] | Bingyi Yan[1] | Huan Pang[1]

[1]School of Chemistry and Chemical Engineering, Yangzhou Key Laboratory of Smart Materials and Clean Energy, Yangzhou University, Yangzhou P. R. China | [2]Zhejiang Key Laboratory for Industrial Solid Waste Thermal Hydrolysis Technology and Intelligent Equipment, Huzhou Key Laboratory of Environmental Functional Materials and Pollution Control, Department of Materials Engineering, Huzhou University, Huzhou, China

Correspondence: Huan Pang (huanpangchem@hotmail.com)

Received: 26 August 2025 | **Revised:** 24 October 2025 | **Accepted:** 4 November 2025

Keywords: architectures | batteries | composites | electrocatalysis | Prussian blue analogs

ABSTRACT

Nanoheterostructures that integrate Prussian blue (PB) or Prussian blue analogs (PBAs) coordination polymers combined with other inorganic substances integrated into a unified nanosystem represent an extremely demanding yet rapidly developing category of distinct hybrid multifunctional nanostructures. In these structures, chemical and physical properties can function either independently or synergistically to produce unique effects. The conventional PB, distinguished by its flawless structure and highly integrated lattice, demonstrates exceptional structural stability while harboring a diverse range of vacancy networks. And so forth, providing the basis for all kinds of physicochemical reactions. In this review, we comprehensively summarize the key advancements in this category of nanomaterials, focusing on their compositions, structures, and various applications. The characteristics of different structures and their applications in battery electrocatalysis are introduced, and the role and contribution of nanomaterials are highlighted.

1 | Introduction

In recent years, the escalating energy shortage and worsening environmental degradation have compelled the global scientific community to emphasize the advancement of efficient and sustainable functional materials. Within this context, Prussian blue (PB) and its derivatives, known as PB analogs (PBAs), have emerged as focal points of interest. These coordination compounds display distinctive 3D open-framework architectures and have adjustable physical and chemical characteristics [1–5] and multidimensional functionalities [6–10], rendering them highly promising for diverse applications. This review underscores their importance in contemporary research. Concurrently, advancements in nanomaterials science [11] have provided novel strategies for optimizing the performance and expanding the applications of these traditional materials. The integration of PB/PBAs with nanotechnology not only deepens fundamental research but also demonstrates immense potential in energy [12], environmental, and biomedical fields.

PB, first synthesized in the early 18th century, is chemically represented by the formula Fe_4 $[Fe(CN)_6]_3 \cdot xH_2O$. This compound features a cubic lattice structure composed of cyanide-bridged Fe^{2+} and Fe^{3+} ions. This rigid framework endows it with exceptional ion conductivity, redox activity, and structural stability. By substituting metal centers [13, 14] (e.g., Co, Ni [15], Mn) or modulating coordination environments, the electronic structure, pore size, and surface properties of PBAs can be precisely tailored to meet diverse application requirements. For instance, in sodium [16]/potassium-ion batteries [17–23], the open channels of PBAs enable rapid insertion/extraction of alkali metal ions, delivering excellent performance at high rates and prolonged cycling stability [24–27]. In the field of catalysis, the synergistic interactions between metal centers are pivotal in significantly enhancing the OER activity and the efficiency of photocatalytic processes [28–32].

The incorporation of nanotechnology further unlocks the potential of Prussian Blue-based materials. Through size control, morphology engineering, or composite design (e.g., nanoparticles,

nanowires, porous frameworks, or hybrid structures with carbon-based materials), their specific surface area, electron transport pathways, and interfacial reaction kinetics are markedly improved. For example, nanoscale PBAs expose more active sites, boosting adsorption capacity for heavy metal ions, while PB/graphene composites form conductive networks to enhance electrochemical performance [33, 34]. Additionally, PB-based nanomaterials are emerging in biomedicine, leveraging their porous structures for drug loading/controlled release and photothermal conversion properties for innovative tumor therapy strategies. The engineered PB nanohybrid multicellular spheroids (PBNPs@MCSs), endowed with enhanced antioxidant capabilities, effectively mitigated cell apoptosis in peroxidative environments. Furthermore, these nanohybrids exhibited superior performance in modulating the microenvironment and promoting bone repair in both in vitro conditions experimental models and in living organisms living systems [35]. Moreover, drug repurposing entails discovering novel clinical applications for drugs that have already received approval for clinical use. This strategy markedly diminishes the cost and time associated with clinical evaluation, leveraging the extensively documented molecular structures, pharmacokinetics, and pharmacodynamics of these drugs. Within this framework, clinically approved PB has attracted substantial attention owing to its unique optical, magnetic, and enzymatic characteristics [36]. Ga-based nanoparticles (NPs) containing varying amounts of Ga are synthesized in a single step by using PB, which possesses numerous Fe sites, as a substrate for Ga substitution. This strategy is specifically designed to overcome the limitations of both materials and develop an efficient nanomedicine [37]. Moreover, scientists have successfully fabricated a hierarchically porous MOF heterostructure with remarkable characteristics regionally arranging micro-, meso-, and macropores in a structured manner through epitaxially cultivating a microporous ZIF-8 shell on a hollow PB core [38].

Nevertheless, integration of PB and its analogs (Figure 1) with nanomaterials still faces considerable challenges. Despite substantial progress in developing a wide variety of PBAs, the one-pot synthesis of PBAs with highly complex compositions and architectures continues to be a formidable obstacle [39]. The application of advanced oxidation processes involving peroxymonosulfate (PMS) for the removal of quaternary ammonium compounds encounters several challenges. Notably, these processes are associated with substantial metal dissolution and high oxidant consumption, which collectively hinder their practical implementation [40]. Pyrolytic PBAs often experience severe agglomeration issues, which significantly restrict their performance in microwave absorption applications [41]. Moreover, the NaMHCF synthesized via the traditional coprecipitation method exhibits a high content of crystalline water and a significant number of defects [42]. Furthermore, the progress in defect engineering has enabled the realization of various technologies.

Nevertheless, the selective creation of defect sites within existing material systems continues to pose a substantial challenge [43]. Key challenges encompass the precise control of structural defects during nanoscale fabrication, the enhancement of long-term cycling stability, and the establishment of scalable, environmentally friendly synthesis approaches. Moreover, gaining deeper insights into structure-property correlations necessitates the application of cutting-edge in situ characterization tools and sophisticated theoretical simulations. Looking ahead, interdisciplinary cooperation and creative material design have the potential to drive PB-based nanomaterials toward significant advancements in intelligent responsive systems, high-efficiency energy storage solutions, and sustainable environmental remediation technologies. This review offers an extensive summary of the structural features of PB and PBAs, approaches to nanoscale modifications, and their uses in energy, catalysis, and biomedicine. Additionally, it offers an in-depth analysis of existing challenges and suggests potential avenues for future research, with the goal of offering theoretical guidance and practical ideas for the advancement of new functional nanomaterials.

2 | Structural Characteristics of PB and its Analogs

2.1 | Single Crystal PBAs

The actual crystal structures of both PBAs and PB have long represented a challenging and significant issue in solid-state chemistry. This is because the seemingly straightforward powder diffraction patterns mask an extraordinary atomic complexity level. The common ancestral structure originates from a cubic lattice and aligns with the optimized arrangement $M[M'(CN)_6]$. In the structure under discussion, M and M′ atoms (usually transition-metal cations) reside in alternating vertices of the lattice and are coordinated in an octahedral geometry by linking with cyanide ions (CN^-) located along the boundaries of the lattice. This arrangement bears a striking resemblance toward the double perovskite structure. Indeed, the concepts of covalency and octahedral coordination, which stabilize oxide ceramics in perovskites, also support this structure in metal-cyanide complexes in a similar manner, thus considering the variety in chemical composition observed in PBAs. To ensure charging neutrality. PB is inherently a mixed-valence cyanide compound of iron in its ferrous (2+) and ferric (3+) oxidation states, indicating that its composition does not strictly conform to the oxidation-state-sumrule. To compensate for this, vacancies play a critical role: the compound's structure can be calculated by utilizing the formula $FeIII[FeII(CN)_6]_{3/4}1/4{\cdot}xH_2O$ (Figure 2a,b), where the notation denotes a $[FeII(CN)_6]^{4-}$ vacancy. These vacancies are typically occupied through the interaction with water molecules, which fill the remaining coordination sites of the neighboring M cations. Scientists employ the word "vacancy" to characterize the possible occupancy of the M′ position by water molecules. Every empty position generates a micropore having an effective diameter of roughly 8.5 Å. Thus, when two neighboring vacancies exist, they coalesce to create a larger micropore. A stochastic arrangement of vacancies suggesting a large quantity or bulk microporosity once the fraction of vacancies surpasses the percolation threshold in the face-centered cubic (fcc) structure M′ sublattice (approximately 0.20). However, PB does not exhibit microporosity. X-ray diffraction of single crystals studies has demonstrated that empty spaces are likely to remain separated from each other through the use of a particular structured sequence. The maximum vacancy fraction that permits complete isolation of vacancies is one-fourth. Due to geometric constraints, these vacancies—irrespective of their distribution—necessarily form connected neighboring pairs.

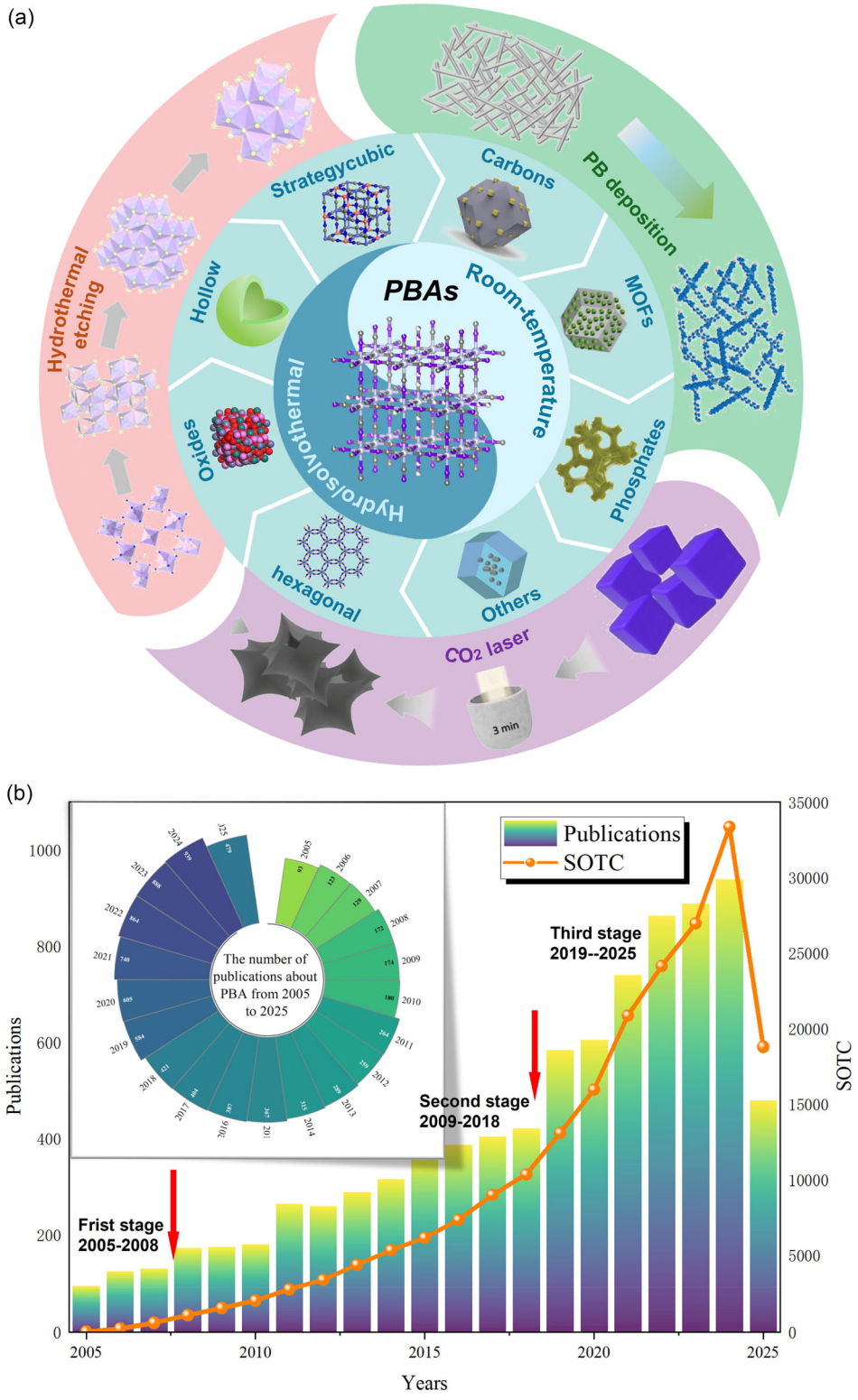

FIGURE 1 | (a) Crystal arrangement during the phase transformation in PBA hydrothermal etching. Schematic illustration of AgNWs@PB composites and detailed explanation of the direct formation mechanism of the CoFe2O4@NC hollow structure from CoFe-PBA nanocubes via CO2 laser exposure. Furthermore, various PBAs with distinct structures and compositions have been identified. (b) The number of publications and SOTC about PBA from 2005 to 2025.

The formation of an extended micropore network, along with its characteristics, depends on the correlations of vacancies across longer distances. The overall microporous architecture of PBAs remains significantly underexplored, despite the critical role that mass transport plays in determining many key properties of this material family. Research has revealed several insights: isotherm measurements for adsorption indicate diverse pore features throughout different PBAs; solid-state cadmium

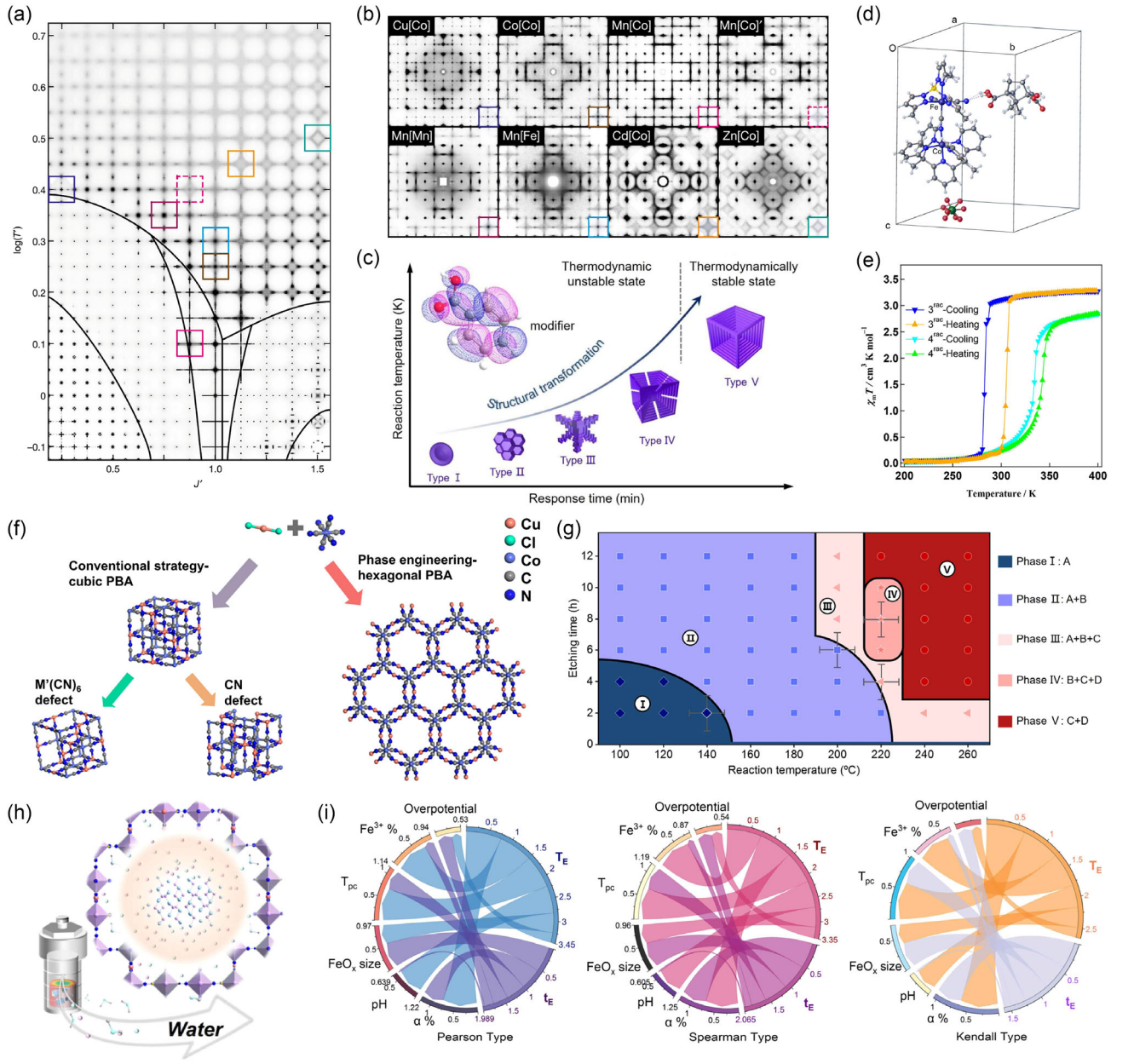

FIGURE 2 | (a) A Monte–Carlo diffuses scattering map with the experimentally plane-averaged scattering overlaid (indicated by squares). (b) Diffuse scattering from single crystals of PBAs. Reprinted with permission [44]. Copyright 2020, Springer Nature. (c) Demonstration of the self-assembly procedure for PB crystals under different hydrothermal reaction temperatures and time periods. Reprinted with permission [45]. Copyright 2024, Wiley-VCH. (d) The crystal structure of 4^{rac} has been extracted, revealing the structural disorder of the HBD unit and the ClO^{4-} anion. (e) $\chi_m T$ values of 3^{rac} and 4^{rac}. Reprinted with permission [46]. Copyright 2024, American Chemical Society. (f) The schematic representations for the synthesis of conventional cubic PBAs with defect regulation and atypical hexagonal PBAs through phase manipulation. Reprinted with permission [47]. Copyright 2025, Springer Nature. (g) Hydrothermal phase diagram of PBA. (h) Schematic diagram of the PBA reaction in a hydrothermal high-pressure reactor. (i) The impact of hydrothermal etching reaction temperature and duration on other parameters estimated through three statistical models. Reprinted with permission [48]. Copyright 2024, American Chemical Society.

NMR studies have demonstrated nonrandom defect arrangements within $Cd[Fe_xCo_{1-x}]$; faint fundamental superlattice reflections are occasionally identified in powder X-ray diffraction (PXRD) profiles, typically understood as proof of partial or complete vacancy of Prussian-blue-like ordering; HRTEM has identified vacancy chains in certain copper-based PBAs, whereas the lack of them is noted in samples containing zinc; and within the sole monocrystalline diffraction analysis conducted on a PBA, structured diffuse scattering was detected and analyzed using Warren–Cowley correlation parameters. Collectively, these findings suggest that vacancy arrangements are not stochastic and highlight significant diversity in the pore structures among various PBAs. In this research, the investigator explored vacancy correlations in various perovskite-related materials by growing high-quality single crystals, explaining these profiles using a 3D-dPDF analysis combined with Monte–Carlo methods [44].

2.2 | Spiral-Concave PB

In addition, exploring the development and change mechanisms of spiral-concave crystals is essential to promote the development of innovative material design and deepening our understanding (Figure 2c). Significantly, the arrangement of the coordination sphere in SC-HCF can be accurately tuned by incorporating various metals. Researchers clarified the transformation mechanism from SC-HCF to Co-HCF, a process that is enhanced by oriented adsorption and ion exchange. Experimental findings, supported by density functional theory calculations, demonstrate that Co-HCF has an ideal energy band structure. This architecture allows for the adjustment of the electronic environment in the local area, thus improving the efficiency of the OER. This study not only explains the development process and organization control of highly stepped HCF but also offers a novel strategy for designing nanocrystals with complex spiral-concave architectures [45]. In addition, iron-based PBAs constitute a potential category of cathode materials for sodium-ion batteries are characterized by their low cost and ease of preparation. The quality of these materials, as well as their electrochemical performance, is substantially determined by the precipitation process. In this research, the authors introduce a controllable precipitation technique for producing high-performance PB materials specifically designed for sodium-ion storage applications. Through a detailed examination related to the formation of nuclei and growth highly crystalline processes PB microcubes, it was determined that these materials possess a rhombohedral structure. This structural characteristic provides advantageous attributes, including an excellent initial charge–discharge efficiency, outstanding rate performance, and exceptional cycling durability. The phase evolution of the synthesized material is explored using synchrotron-based in-place powder X-ray diffraction, demonstrating highly reversible architectural changes. Additionally, the PB material fabricated through a scalable approach shows reliable cycling stability in a pouch full cell configuration for more than 1000 cycles. This study is regarded by scientists as a significant step forward in achieving practical application of PB materials in SIBs [49]. The scientist created innovative, switchable molecular structures that are defined by sudden and total phase transitions (as illustrated in Figure 2d,e). These transformations are facilitated by hydrogen bonding with a chiral carboxylic acid [46]. Researchers introduce a straightforward yet adaptable method for synthesizing unconventional hexagonal open structures of PBAs (as shown in Figure 2f) [47]. Researchers utilized PBA to construct a machine-learning model (Figure 2g–i) and assess its hydrothermal phase diagram [48]. Maintaining the structural integrity of electrode materials while ensuring high reversibility is crucial to improve the long-term stability of battery systems. Nevertheless, many electrodes materials experience deterioration over charge–discharge cycles as a result of the unavoidable rise in entropy. The doping approach in bulk PBA leads to substantially enhanced electron transport and ion diffusion characteristics. This improvement considerably boosts the material's cyclability, allowing it to maintain stable performance for over 4000 cycles within a diluted electrolyte setting. In contrast, the FeCo-PBA nanocubes present a relatively rough surface texture. Additionally, the FeNi-PBA nanocubes display smoother edges at their eight corners. Researchers analyze the predominant forms of structural complexity in PBAs and explore strategies for managing these complexities through meticulous compositional design. Although the well-established parent face-centered cubic (fcc) structure, often associated with PBAs, is widely observed, various distortions can compromise its cubic symmetry, either locally or globally. Researchers will focus on the most influential distortions. In the subsequent discussion, the researcher will examine the interaction among various factors and the experimental response across different degrees of freedom. Where relevant, these findings will be connected to the specific case of potassium manganese hexacyanoferrate (K_xMn_y). Transition metal hexacyanoferrates, such as PB and PBAs, constitute a wide-ranging class defined by an open-framework architecture that displays a perovskite-like, face-centered cubic arrangement. The standard crystal structures of PBAs ($A_xMA[MB(CN)_6]$) are also depicted. A perfectly structured PB with a highly integrated lattice demonstrates remarkable structural stability. Nevertheless, structural flaws that are inevitably introduced during the synthesis process might cause structural deterioration while cycling, which in turn triggers a swift decline in capacity and hinders practical usage. On the other hand, not every defect is harmful. Additionally, the current difficulties and possible future trends are explored in detail, highlighting the essential significance of defect engineering in enhancing PBAs for SIB-related applications [50].

2.3 | High Entropy PBAs

In contrast to other structured cathode materials, the 3D open framework characteristic of PBAs enables large Na^+ ions to be readily accommodated and removed [51]. This distinctive attribute is ascribed to the structural resilience of PBAs, which enables their high effectiveness as cathodes across both nonaqueous and aqueous SIB systems [52]. Notwithstanding their benefits, PBAs face pressing issues such as limited cycling stability, often due to irreversible phase changes, that require resolution. Here, the high entropy strategy, which elevates material complexity by employing multiple constituent metals, has proven to be an effective avenue for tackling these challenges.

The application of high-entropy strategies in both aqueous and nonaqueous sodium-ion battery systems effectively strengthens the structural integrity of the lattice, accommodating sodium ion (de)intercalation with reduced mechanical strain. This suppression of detrimental phase transitions, coupled with the promotion of a highly reversible storage mechanism, endows the optimized PBAs with exceptional long-term cycling resilience. An additional advantage of HE-PBA electrodes is the exhibition of higher Na^+ diffusion coefficients throughout the (de)intercalation processes compared with standard PBAs. This is complemented by a significant tailoring of the electronic structure through multi-element incorporation, which induces a narrowing of the bandgap and an elevation of electronic density, resulting in a marked enhancement of conductivity. Collectively, these findings underscore the considerable potential of high-entropy strategies in optimizing the reaction kinetics of PBA-based SIBs [53].

3 | Synthesis of PB/PBAs with Different Structures

3.1 | Square Nanostructure

For the synthesis of FeNi-PBA, 3 mmol of $NiCl_2{\cdot}6H_2O$ was utilized, omitting $CoCl_2{\cdot}6H_2O$. In contrast, the preparation of

FeCo-PBA involved using 3 mmol of $CoCl_2{\cdot}6H_2O$, excluding $NiCl_2{\cdot}6H_2O$, and following a similar process to that applied for FeCoNi-PBA. The NiFe-PBA was synthesized through an adjusted co-precipitation technique. Specifically, a solution was made by dissolving 0.1426 g of nickel chloride hexahydrate ($NiCl_2{\cdot}6H_2O$) along with 0.2647 g of trisodium citrate dihydrate ($Na_3C_6H_5O_7{\cdot}2H_2O$) in 20 mL of deionized water. Subsequently, this solution was mixed with another solution. In the latter solution, 0.1317 g of potassium ferricyanide ($K_3[Fe(CN)_6]$) was dissolved in 20 mL of deionized water. The resulting mixture was continuously magnetically stirred for 3 min. After that, it was maintained at room temperature and left to age for 10 h. After that, the precipitates were collected through centrifugation. Subsequently, they were thoroughly rinsed multiple times with a water/ethanol solution. Finally, they were dried at 60°C for a long time. For the synthesis of PBA@POM composites, researchers employed a single-step hydrothermal approach to fabricate PBA, followed by incorporating POM using it as a template, thereby producing composites with porous features. The imaging analysis shows that PBA has a uniformly smooth tetrahedral structure on its surface, consistent with the previously published findings in the literature.

3.2 | Polygon Structure

Furthermore, researchers investigate the principal types of structural complexity in PBAs, their influence on material functionality, and the strategies for managing them through meticulous compositional selection. Our paper ends with a detailed examination of the strategic use of interactions among different distortion mechanisms to improve the performance of this system and other associated systems. This, in turn, could facilitate the development of next-generation PBA materials [54]. Aqueous energy storage technologies offer significant benefits for large-scale power stations, characterized by their affordability, safe functionality, and eco-friendliness. Nevertheless, the intricate energy storage processes in water-based environments impose strict demands on suitable material hosts. Coordination materials composed of metal-organic structures, have attracted significant research attention due to their open-framework structures that facilitate the reversible insertion and removal of diverse guest cations. This manuscript explores essential chemistry and electrochemical properties of PB and PBAs. Subsequently, it shifts emphasis to examining targeted design approaches aimed at tackling specific issues. The recent progress of PB/PBAs in different kinds of aqueous batteries and supercapacitors is thoroughly analyzed. This analysis is achieved by establishing correlations between their electrochemical characteristics and their structural and compositional traits. Ultimately, this paper sums up the current challenges and key insights related to the future development of PB/PBAs for practical uses in aqueous energy storage [55].

3.3 | Hollow Structure

Particles with hollow structures, featuring substantial internal cavities and slender outer walls, represent a significant category of materials. These materials possess extensive possible applications across multiple domains, such as energy storage, chemical catalysis, photonics, and biomedical delivery systems. The properties of these particles are significantly determined by the composition and complex nanostructures of their shell regions. Extensive research has been dedicated to modulating these factors to enhance performance. Recently, hollow particles with nanoporous shells have garnered increasing attention because their high pore volume and extensive surface area not only improve storage capacity but also promote the efficient diffusion of guest molecules into the interior cavity. For instance, metal oxide hollow particles exhibit an exceptional lithium storage capacity and outstanding cycle stability, which not only enhance their performance in lithium-ion batteries but also improve gas sensing capabilities and catalytic efficiency in other applications [56]. Furthermore, a simple yet adaptable approach was presented for the in-situ formation of hierarchical PBAs on diverse metal substrates. This was achieved through a combination of an interfacial redox reaction and an in-situ precipitation process. A range of PBAs with tunable chemical properties were successfully synthesized, thereby broadening the potential applications of PBAs. A detailed exploration of the underlying mechanism indicated that the potential difference promotes the gradual release of metal ions, which subsequently undergo coordination and in situ precipitation to form the desired PBAs. Therefore, with the assistance of acid, the kinetic growth process can be precisely regulated, leading to remarkable morphological flexibility. Furthermore, in the development of nanomaterials, both kinetic and thermodynamic factors play crucial roles in shaping the structures and phases of nanocrystals. As a result, scientists have devoted considerable effort to exploring diverse synthesis methods to precisely engineer desired nanocrystals and elucidate the underlying principles that dictate the formation of particular structures. Through modification of the overall reaction duration, MnCo Prussian blue analog (MnCoPBA) crystals, with assistance from sodium dodecyl sulfate, experience four unique morphological changes across various stages. Additionally, it is evident that epitaxial growth on the surface of MnCoPBA nanocrystals preferentially occurs along the (100) plane. This review provides a detailed examination of the thermodynamic and kinetic principles governing the morphological transformation process. By adjusting the overall reaction time, MnCoPBA crystals, with the help of sodium dodecyl sulfate, undergo four distinct morphological transitions at different stages. Furthermore, it is clear that epitaxial growth on the MnCoPBA nanocrystal surface predominantly proceeds along the (100) crystal plane. This study offers an in-depth analysis of the thermodynamic and kinetic mechanisms that regulate the morphological evolution process [57] Moreover, hollow materials obtained from MOFs exhibit exceptional physical and chemical characteristics, as well as broad application prospects, due to their adjustable architecture, makeup, pore structure, and particular surface area.

Furthermore, hollow materials derived from MOFs exhibit outstanding physical and chemical characteristics. By conducting an in-depth analysis and discussion of 14 reaction processes, a thorough mechanism for converting MOFs into hollow-structured materials is clearly presented. Subsequently, the review highlights the applications of these hollow structures serving as electrode materials in lithium-ion batteries and hybrid supercapacitors, and electrocatalytic reactions. Finally, the review delves more deeply and clearly into the future outlook on emerging challenges and advancements in the controllable synthesis and

electrochemical applications of the subject [58]. Furthermore, because of their unique structural features, hollow structures exhibit intriguing physical and chemical properties and have found broad applications, particularly within the domain of electrochemical energy storage and transformation. Past few years, PB and PBA have garnered growing interest due to their affordable costs, simple synthesis methods, inherent open structures, and adjustable compositions. This review article comprehensively analyzes and assesses recent progress in the field of development and utilization of hollow structures derived from PB and PBA for the storage and conversion of electrochemical energy applications. A number of typical cases are presented regarding the fabrication of hollow structures from PB and PBA-derived materials, with a focus on their structural features. Moreover, this review provides a summary of the latest progress in this area, along with a detailed evaluation of the existing limitations and key challenges. Ultimately, it suggests possible approaches to overcome these issues and explores prospective avenues for future research [59]. Moreover, PB-type nanoparticles represent an exceptional category of molecule-based nanomaterials. These nanoparticles possess the capability for surface alteration alongside distinct benefits derived from their porous, molecule-driven structures. They also exhibit intriguing chemical and physical characteristics, such as redox capabilities, magnetic properties, photothermal effects, and host–guest interactions. Researchers have concentrated on the latest developments, while also contrasting these with contemporary approaches utilized in MOFs. This offers valuable insights into the potential directions for future research in this area [60]. CoFe-PBA serves as a starting material for the preparation of NGC and PDA-20. These materials are subsequently used to encapsulate $CoSe_2$/$FeSe_2$ nanoparticles in a stepwise manner, resulting in a dual-layer coated structure (as illustrated in Figure 3a). The resulting composite is viewed as a promising anode material for high-performance SIBs [61]. Furthermore, a straightforward self-templating strategy is presented for the synthesis of hollow nanocube composites composed of PBA (Figure 3b) and metal-organic frameworks (PBA/MOF HNCs) [62]. The development of highly porous 3D framework PBA (CoFe-PBA) via structural self-transformation has been investigated. This process is guided by a combination of template-assisted epitaxial growth (as shown in Figure 3c,d), constrained assembly, and oriented assembly [63].

3.4 | Others

Researchers outline a single-step fabrication technique for generating Fe–Co PBAs, which display both an uneven composition distribution and a core–shell structure featuring open cages. The preparation process of these Fe–Co PBAs is as follows: Divalent cobalt ions were mixed with potassium ferricyanide in an acidic solution containing polyvinylpyrrolidone (PVP). At ambient conditions, $Co_3[FeIII(CN)_6]_2$ nanocubes assembled quickly. Following this, the identical reaction solution was exposed to hydrothermal conditions at 80°C for different time intervals, resulting in the final products (labeled as PBA-1 to PBA-5, respectively). The application of PVP as a reductant facilitated partial conversion of $[Fe(CN)_6]^{3-}$ into FeII species. Building upon their innovative efforts, nickel-cobalt PBAs (Ni-Co PBAs) in the shape of nanocones were effectively produced using a simple ammonia-etching technique. In the synthesis process, the precipitation duration for Ni–Co PBA nanocubes was reduced. As the process progresses proceeds, etching extends along the diagonals of the cubes, ultimately resulting in the formation of nanocones as the twelve edges are gradually eliminated. Nevertheless, these materials generally encounter issues like insufficient electronic conductivity and a lack of structural stability. This hierarchically nested structure facilitates superior lattice expansion accommodation, shortens the sodium ion diffusion pathway, enhances electronic transport properties, and optimizes redox activities, thus attaining an outstanding rate performance, substantial particular capability, and prolonged cycling durability. As expected, the fabricated FeHCFe nanoframes/CNTs electrode demonstrates exceptional performance in handling high rates. This research introduces a novel approach to designing sophisticated electrode materials specifically suited for ultrahigh-rate SIBs [64].

4 | Prussian Blue and its Analogs Composite Nanomaterials

4.1 | MOF/PBA

Moreover, PBAs are considered potential candidates for sodium storage due to the distinctive benefits of their metal-organic framework structure. Nevertheless, the actual implementation of these materials has been obstructed by the challenges of limited specific capacity and insufficient reversibility, which stem from phase transformations during charge/discharge cycles. This research presents a novel method for dramatically improving the electrochemical characteristics of PBAs through the incorporation of high entropy into their crystalline lattice. In order to accomplish this, five different metal elements are embedded within the structure, each bonded to the same nitrogen site. This design increases the system's configurational entropy to exceed 1.5R. The primary elements driving these improvements include high configurational entropy and the related effects, along with the existence of multiple active redox sites. It has been reported that gases are released from PBAs. Furthermore, the generation of dimeric cyanogen, resulting from the oxidation of cyanide ligands, has been observed. Through the enhancement of the electrochemical stability window, a Coulombic efficiency close to 100% can be maintained even after over 3000 cycles [65]. PB nanoparticles and their related compounds constitute a class of MOFs [66, 67] comprising alternating ferric and ferrous iron ions bridged by cyanide ligands. These nanoparticles display exceptional biocompatibility and biosafety. Moreover, they possess other notable features. In these reactions, the iron atoms function as active metal centers. The varied oxidation states of these nanoparticles are fundamental to their diverse catalytic capabilities, which include functions similar to peroxidase, catalase, and superoxide dismutase. Based on their catalytic activity, these nanomaterials may either produce or eliminate ROS [68]. Furthermore, the capability to achieve multiple readouts via multimodal detection improves the adaptability, reliability, and accuracy of lateral flow immunoassays. Integrating two distinct MOFs [69, 70] into a novel composite material offers significant potential, as demonstrated in Figure 4a,b, for advancing multimodal LFIA technology [71]. For the first time, it is shown that an amphiphilic polymer-coated $CsPbX_3$ exhibits oxidase-like and ascorbate oxidase-like activities

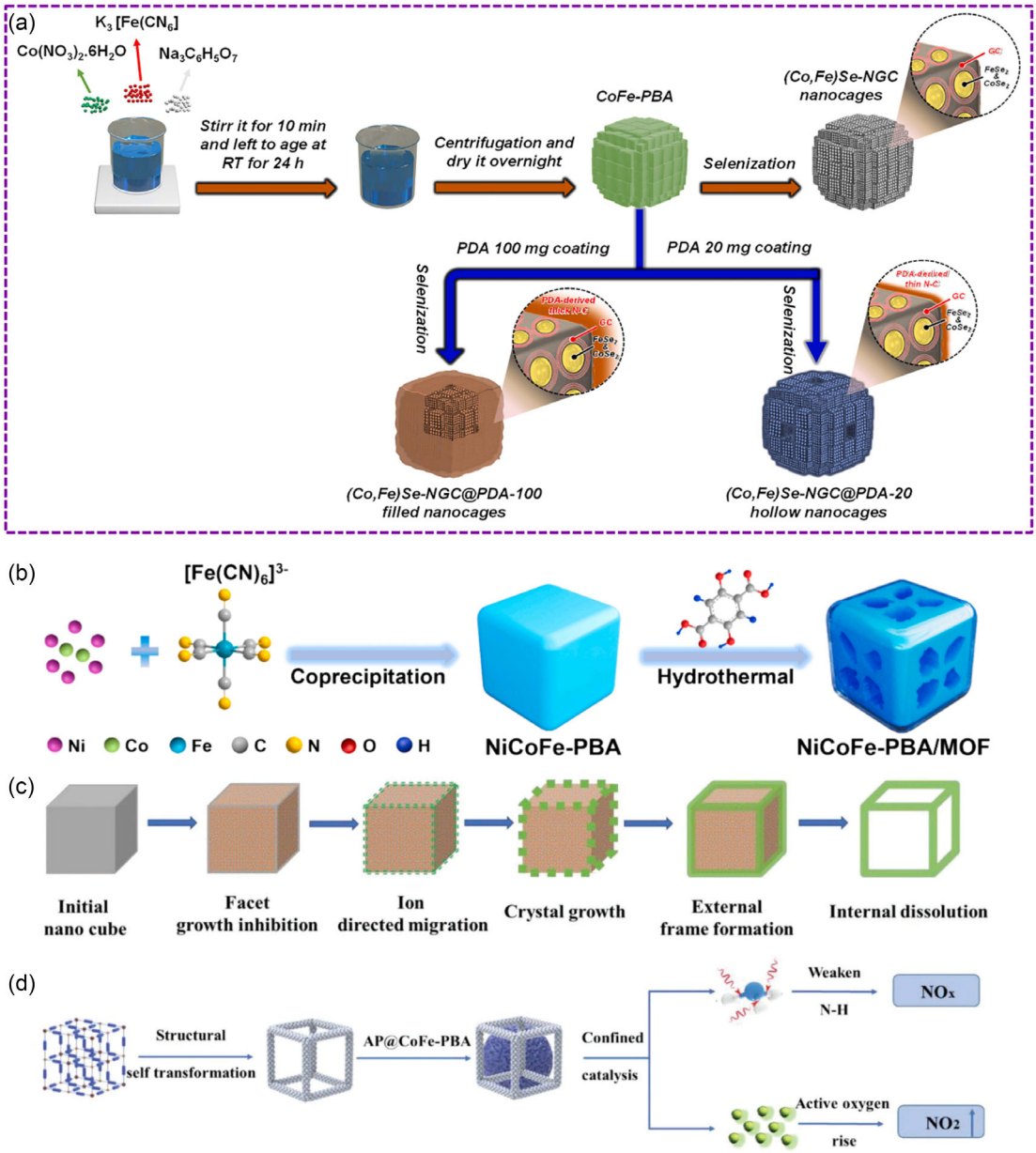

FIGURE 3 | (a) Schematic representation of the fabrication process for (Co, Fe)Se-NGC nanocages, (Co, Fe)Se-NGC@PDA-20 hollow nanocages, and (Co, Fe)Se-NGC@PDA-100 filled nanocages using a co-precipitation method followed by selenization. Reprinted with permission [61]. Copyright 2024, Elsevier. (b) The proposed method for schematic synthesis involves NiCoFe-PBA/MOF HNCs. Reprinted with permission [62]. Copyright 2024, Elsevier. (c) Schematic diagram of structural self-transformation of CoFe-PBA. (d) Diagram illustrating the thermal breakdown of AP when catalyzed by CoFe-PBA. Reprinted with permission [63]. Copyright 2023, Wiley-VCH GmbH.

(Figure 4c–e), and the mechanism of its catalysis is investigated in greater depth [72]. The researcher presents an innovative approach for treating wastewater contaminated with ferrocyanide, as illustrated in Figure 4f [73].

4.2 | MXene/PBA

Despite their advantages as LiB anodes—low Li^+ diffusion barriers and high conductivity—MXenes suffer from structural aggregation and stacking, which hinders ionic/electronic shuttle and causes capacity fade. To address this, the use of interlayer spacers in MXene hybrids has emerged as a key strategy. Introducing PBAs as a spacer preserves MXene's conductivity, curbs PBA structural degradation, and incorporates the large surface area and porosity of PBAs. Intelligent regulation of MXene sheet size enables the fabrication of Co-PBA@MXene hybrids with both sandwich and core–shell morphologies. Moreover, adjusting the Co-PBA/MXene mass ratio allows for precise control over the MXene shell thickness in the resulting Co@M(x:y) hybrids. Among these, the Co@M(5:2) anode exhibits excellent specific capacity (603 mAh g^{-1} at 0.2 A g^{-1} after 100 cycles) and sustained cycling stability, resulting from the conductive protection of the MXene shell and the multi-redox activity and porosity of the Co-PBA core [74]. Moreover, fabricating high-performance, flame-retardant MXene-based polymers with superior mechanical

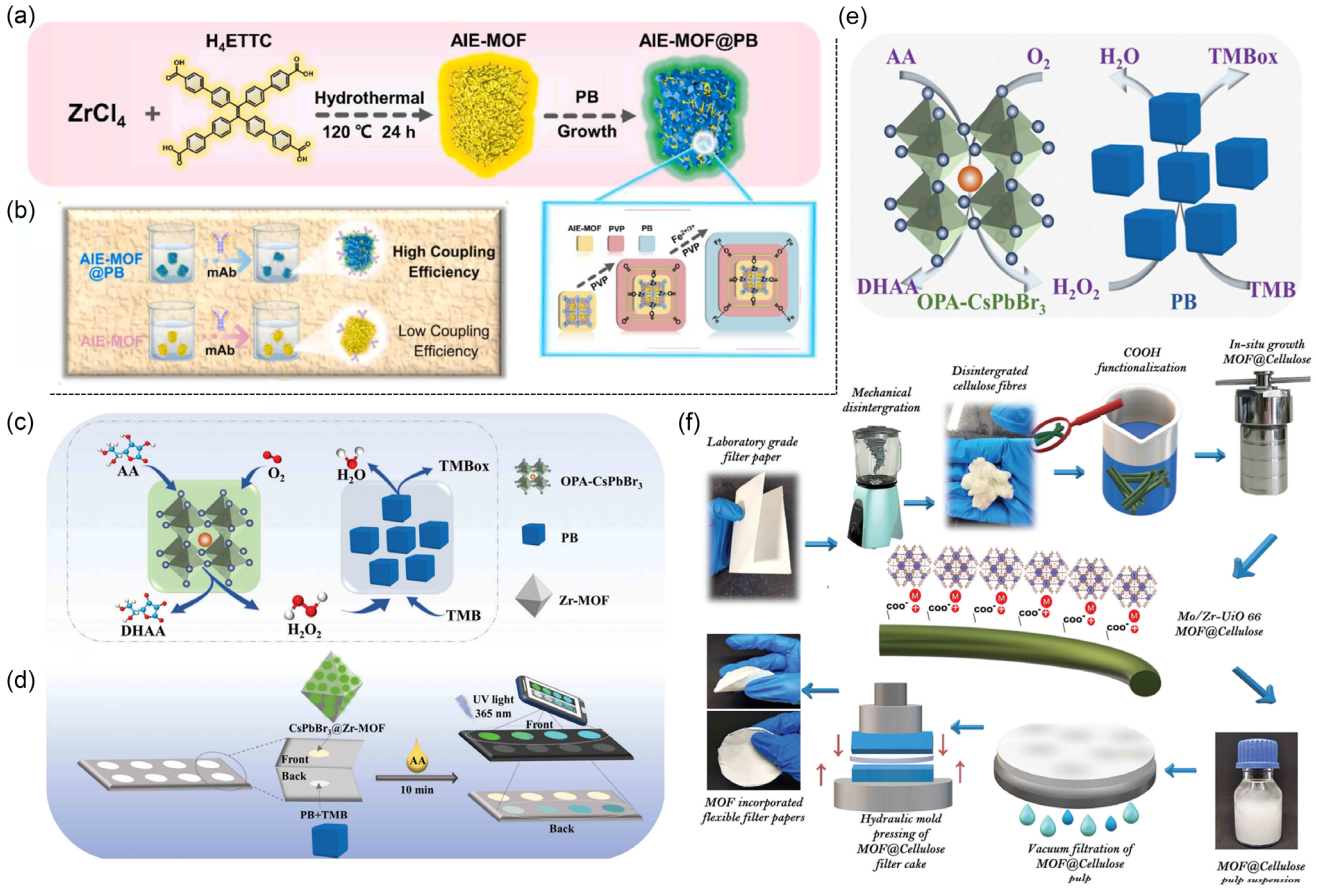

FIGURE 4 | (a) Illustrative diagram of the construction process for the AIE-MOF@PB hybrid structure. (b) Diagrammatic representation of the procedure for conjugating mAbs with AIE-MOF and AIE-MOF@PB. Reprinted with permission [71]. Copyright 2024, Elsevier. (c) The possible reaction pathways for biomimetic cascade catalysis using OPA-$CsPbBr_3$ nanocrystals and PB are explored. (d) A paper-based device was developed to implement biomimetic cascade nanozyme reactions for the dual-mode ratiometric detection of ascorbic acid using both fluorescence and colorimetric methods. (e) The enzyme-free cascade system constructed from OPA-$CsPbBr_3$ nanocrystals and PB has a reaction mechanism that can be described as follows. Reprinted with permission [72]. Copyright 2023, The Authors. (f) Illustrative diagram showing the preparation of Mo/Zr-UiO-66 MOF-integrated cellulose filter papers. Reprinted with permission [73]. Copyright 2023, Wiley-VCH GmbH.

properties is a major challenge. This study demonstrates a surface modification of MXene nanosheets using PBAs through electrostatic self-assembly, yielding hierarchical MXene@PBA nanohybrids. When integrated into an epoxy matrix, the resulting EP-MXene@PBA nanocomposites benefit from the excellent dispersion of MXene@PBA. Impressively, at ultra-low additions, these nanohybrids confer outstanding flame retardancy and smoke suppression. For instance, with only 1.0 wt% MXene@PBA, the EP-1.0%MXene@PBA composite attains a UL-94 V-0 rating and shows remarkable reductions in pHRR (36.70%), TSP (34.28%), and pCO (43.48%) compared with pristine epoxy. Additionally, the nanohybrids improve the material's flexural and impact strengths. This work provides a viable approach for developing multifunctional MXene-derived polymer nanocomposites with broad industrial potential [75].

Recently, PBAs have been recognized as potential electrode materials to improve the efficiency of capacitive deionization (CDI). Nevertheless, a balance between capacity for desalination and its stability remains elusive in monometallic bimetallic PBAs, posing challenges to achieving both high desalination efficiency and outstanding recyclability at the same time. The Ni^{3+}/Ni^{2+} pair showed electrochemical inactivity within the CuFe@NiFe PBA compound [76]. Although significant advancements have been made in the development of monofunctional electrocatalysts for HER or OER, the design of bifunctional electrocatalysts for efficient overall water splitting remains challenging. This study details the development of MoC_2-doped NiFe alloy NPs encapsulated in few-layer N-doped graphene, which is named NG-NiFe@MoC_2. This compound is produced through a single-step calcination method using hybrid precursors. Significantly, an alkaline electrolyte employing NG-NiFe@MoC_2 nanohybrids as bifunctional electrocatalysts accomplished overall water splitting, exhibiting a current density that surpassed that of the high-performance Pt/C//RuO_2 system [77]. Furthermore, a ciprofloxacin (CIP) electrochemical sensor was developed by integrating cobalt-iron PBA with carbon nitride (Co-Fe-PBA@CN). The Co-Fe-PBA on CN was prepared through a straightforward ultrasonication-assisted hydrothermal approach, resulting in a composite with cubic structures anchored on CN layers. The resulting Co-Fe-PBA@CN material was analyzed the physical characterization was conducted using X-ray diffraction (XRD) and scanning electron microscopy (SEM). Subsequently, the electrochemical performance of this composite was evaluated for the detection of the antibiotic ciprofloxacin (CIP). The electrochemical properties were examined through methods. The

Co-Fe-PBA@CN-modified electrode demonstrates an extensive linear range, a minimal detection limit, and exceptional sensitivity for CIP. Furthermore, the altered electrode demonstrates remarkable selectivity, reproducibility, and repeatability in the detection of CIP. The fabricated sensor was verified by analyzing real samples, such as biological specimens including urine and blood serum, along with widely marketed ciprofloxacin tablets. These findings indicate that the sensor has significant practical applicability and dependability [78]. This research presents a novel approach for designing and synthesizing MXene/MOF composites [79] and intricate hollow architectures featuring adjustable architectures and compositions, which facilitates their utilization across a broad spectrum of applications [80].

4.3 | Carbon Material/PBA

To prepare Co-Fe PBA nanocubes anchored on carbon nanotubes (CoFe PBA/CNT). In the past few years, PBAs have drawn considerable interest due to their potential as precursors or templates for creating porous carbon-based materials used in microwave absorption (MA). This fascination arises due to their open-framework architectures, adjustable compositions, and comparatively moderate synthesis requirements. Trimetallic FeCoNi-PBA nanocubes are utilized as precursors. Following this, a distinctive core–shell composite is effectively produced through a pyrolysis method. Furthermore, the synthesis approach based on multimetallic PBAs offers fresh insights into the advancement of carbon-based absorbers that are lightweight, high-performing, cost-efficient, and simple to produce [81]. Moreover, as wireless communication technology continues to evolve rapidly, human living environments are becoming increasingly exposed to a multitude of EWs. As a result, materials that absorb EW are crucial for promoting environmentally friendly living environments. Composites with carbon matrices originating from MOFs constitute a promising class of EW absorption materials with substantial potential for practical applications. However, designing efficient absorbers that exhibit low loading ratios and broad absorption bandwidths remains a significant challenge. The researcher successfully fabricated 1D, uneven, and permeable nitrogen-doped graphene fibers (N-GFs) by assembling 2D graphene sheets. These graphene sheets were surface-engineered with an iron-based PBA derivative. The rough and porous structure of the fibers introduced air spaces that effectively enhanced the impedance matching characteristics of the absorber. Meanwhile, the PBA nanoparticles significantly improved the electromagnetic properties of the N-GFs, leading to superior electromagnetic wave absorption performance. The distinctive microstructure of the Fe-based PBA/N-GFs, combined with their excellent electromagnetic wave absorption capabilities, provides critical insights for the future advanced design and development graphene-based absorbing materials [82]. Moreover, porous MnSe/$FeSe_2$ (Mn-Fe-Se) structures integrated with intertwined carbon nanotubes (CNTs) have been effectively fabricated through a straightforward chemical precipitation method followed by a single-step carbonization-selenization process process of the Mn-Fe PBA precursor. The analysis demonstrates that the synthesized Mn-FeSe/CNTs possess a network architecture with excellent conductivity, wherein Mn-Fe-Se spheres are uniformly embedded within an interconnected web of CNTs. Each Mn-Fe-Se sphere consists of numerous nanoparticles, forming abundant void spaces, and each nanoparticle is homogeneously encapsulated by a thin layer of amorphous carbon doped with nitrogen. Nevertheless, the larger sizes of sodium and potassium ions compared with lithium ions pose a considerable challenge in identifying anode materials with suitable structures for adding and removing these ions. The characterization outcomes show that the prepared Mn-FeSe/CNTs possess a highly conductive network structure. This architecture consists of Mn-Fe-Se spheres either attached to or embedded within an interconnected network of CNTs. Each Mn-Fe-Se sphere is composed of numerous nanoparticles, with abundant void spaces existing between them. Moreover, each nanoparticle is uniformly encapsulated by a thin layer of nitrogen-doped amorphous carbon [83]. In this research, the author leveraged the electrochemical transparency of graphene demonstrates that the direct intercalation of alkali-metal cations does not occur. Even though these cations cannot penetrate the graphene layer and integrate with PB, monolayer graphene-coated PB thin films still displayed electrochemical redox behavior in the existence of alkali metal ions (such as K^+ or Na^+). The protection of graphene not only maintained the electrochemical activity of PB is also significantly improved its stability. To validate this idea, scientists showed that a transparent graphene electrode encapsulating PB could serve as a superior hydrogen peroxide converter. This further highlights the possibility of developing an electrochemical sensor that can carry out long-term measurements with high dependability [84]. PBAs are regarded as highly potential next-generation CDI electrodes require advanced faradic electrode materials, owing to their outstanding theoretical capacity per unit weight, safe nontoxic characteristics, and straightforward synthesis method. Nevertheless, the performance of desalination for PBAs is constrained by their inherently slow reaction rates and inadequate activation of active sites [85]. To tackle the slow kinetics of the ORR and OER, designing effective bifunctional electrocatalysts continues to be a major challenge. Although FeCo alloys are typically recognized as active materials, their catalytic stability is often compromised due to their susceptibility to corrosion. In this research, scientists developed a core–shell structure featuring an FeCo alloy enclosed in nitrogen-doped porous carbon nanosheets (FeCo/NUCSs) using a self-growth approach. The FeCo/NUCSs feature a large specific surface area of $140\ m^2\ g^{-1}$, achieving an outstanding half-wave potential ($E_1/_2 = 0.89$ V) and demonstrating significant resilience against methanol interference in the ORR process. A carbon shell derived from Prussian blue analogs effectively protects the dual active sites (Fe-N_x/Co-N_x) on the FeCo core, significantly enhancing the stability of ORR activity. FeCo/NUCSs demonstrates exceptional OER performance, with an overpotential of 300 mV, surpassing that of RuO_2. This can be credited to the development of highly reactive FeOOH/CoOOH intermediates on the FeCo alloy surface, as confirmed by in situ X-ray diffraction studies. The assembled ZAB demonstrates a favorable open-circuit voltage of 1.51 V, a specific capacity of up to 791.86 mA h g^{-1}, and remarkable durability (lasting for 102 h). This novel catalyst, based on a bimetallic alloy, offers a potential solution for creating durable oxygen electrocatalysts tailored for ZAB applications [86].

4.4 | Others

Moreover, a research study highlights the development of novel magneto-plasmonic core@satellite PBA Au–Ag nanoheterostructures. While the size, shape, and structural integrity of the PBA nanoparticles remain unchanged during the creation of these core@satellite heterostructures, a significant modification in magnetic properties is observed due to the presence of the ultrasmall gold–silver nanosatellites. Notably, these capabilities are dramatically boosted under light exposure, which can be ascribed to a plasmon-enhanced catalytic mechanism. These innovative PBA core@Au–Ag satellite structures exemplify a rare case where the interaction between the two component materials not only modifies their magnetic properties but also elevates their catalytic performance [87].

5 | Prussian Blue and its Analogs Derived Nanomaterials

5.1 | Oxide-Related Nanomaterials

The magnetic copper–iron oxide (CuFeO) was prepared through a straightforward thermal treatment of Cu-Fe PBAs. Electron spin resonance (ESR) combined with DMPO analysis, along with radical scavenging experiments, verified the participation of hydroxyl radicals (·OH) and superoxide radicals ($\cdot O_2^-$) in the degradation mechanism. Among these, the hydroxyl radicals (·OH) were primarily responsible for the decomposition of SMZ. Using liquid chromatography-mass spectrometry (LC-MS) analysis, the intermediates resulting from SMZ degradation were detected, and a likely degradation mechanism was suggested. Furthermore, CuFeO demonstrated excellent stability and reusability, maintaining its performance even after five consecutive cycles of testing. In addition to the relatively low metal leaching and excellent magnetic characteristics of CuFeO, the developed catalyst demonstrates significant potential in the treatment of organic wastewater [88]. Slower OER kinetics represent a critical limiting factor in various renewable energy transformation and storage systems. Although multimetal oxides have been investigated as promising electrocatalysts for OER, the optimal elemental composition of these materials remains elusive. Using density functional theory (DFT) computations, scientists have forecasted that Co oxyhydroxides, when doped with Fe and V, exhibit substantially improved catalytic activity. A scientist prepared a range of amorphous ternary compounds cobalt-iron-vanadium metal oxides using PBAs as innovative metal precursors. These substances display a meticulously regulated metal molar ratio (represented as $Co_aFe_xV_xO_x$, where $a + b + c$ equals 10), featuring evenly distributed components and consistent structures. A comprehensive analysis was conducted to elucidate the relationships between elemental compositions and OER activity in $Co_aFe_xV_xO_x$ compounds. This led to the creation of an extensive catalytic performance map for ternary Co-Fe-V metal oxides in OER, providing a crucial reference for the advancement of high-efficiency electrocatalysts. Particularly noteworthy is the compound $Co_3Fe_4V_3O_x$, which has an elemental ratio of Co:Fe:V equal to 3:4:3 and demonstrates exceptional performance. X-ray photoelectron spectroscopy (XPS) analysis reveals substantial electronic coupling occurring between the metal cations within $Co_aFe_bV_cO_x$. The incorporation of V and Fe alters the electronic structure of Co, leading to nearly optimal adsorption energies for OER intermediates and significantly enhancing its catalytic performance. Furthermore, PBAs that possess compositionally adjustable and structurally consistent characteristics function as flexible and effective metal precursors for the creation of a broad variety of multi-metal oxides. This makes them exceptionally appropriate for diverse renewable energy applications [89]. Achieving efficient water splitting necessitates electrocatalysts that exhibit high activity, cost-effectiveness, and durability. In this research, the author details the creation of Penroseite (Ni, Co)Se_2 nanocages anchored on 3D graphene aerogel by employing PBA as precursors and evaluates their performance in overall water splitting electrolysis. The synergistic interaction between the outstanding catalytic performance of (Ni, Co)Se_2 and the exceptional electrical conductivity of graphene significantly enhances the electrochemical properties of the composite material in alkaline conditions. Notably, the (Ni, Co)Se_2-GA hybrid catalyst achieves a current density of 10 mA cm^{-2} at an exceptionally low cell voltage of 1.60 V. This underscores its potential as a practical alternative to noble metal-based catalysts for water splitting applications [90]. For large-scale electrocatalytic water splitting to generate hydrogen, it is of great significance to develop catalysts for the OER that are both efficient and cost-effective. Generally, PBAs synthesized via the traditional coprecipitation approach exhibit fewer active sites and inferior electrical conductivity. As a result, because of their relatively low OER activity, these materials are often employed as precursors for the synthesis of PBA derivatives, including metal oxides, metal alloys, metal phosphides, and others. The controlled synthesis of NiFe PBA along with Fe_2O_3 byproducts on a nickel foam substrate was realized via a straightforward one-step hydrothermal approach. This was accomplished by regulating the quantities of urea and potassium ferricyanide. After being subjected to additional chemical etching and electrochemical activation, the NiFe PBA was completely converted into an amorphous and highly superhydrophilic NiFe PBA (denoted as a-NiHCF). This a-NiHCF demonstrated excellent OER performance under high current densities. The excellent performance can be ascribed to the following reasons: (1) The in situ growth on a metal foam substrate not only enhances the structural integrity but also facilitates more effective charge transfer and the release of oxygen bubbles. (2) Chemical etching makes additional surface-active sites visible, thereby increasing the available reactive areas. (3) Electrochemical activation results in an amorphous surface layer. This layer demonstrates an enlarged Brunauer–Emmett-Teller (BET) surface area, a greater number of high-valent oxidation states, and improved intrinsic OER activity. (4) The surface structure with superhydrophilic properties enhances the effective adsorption of water molecules. Together, these features position a-NiHCF as an exceptionally potential material for use in electrocatalytic water splitting applications [91].

5.2 | Sulfide-Related Nanomaterials

Solar-aided electrocatalytic water oxidation is highly promising for contemporary energy transformation and retention technologies. This study outlines the development and construction of a novel type of PBAs/transition metal dichalcogenides (TMDs) hybrids. These materials effectively merge the inherent electrocatalytic properties of TMDs for the OER with the light-responsive characteristics of both PBAs and TMDs, achieving a synergistic effect. In particular, the porous architecture, tailored surface

imperfections, and numerous oxygen vacancies significantly boost their electrocatalytic performance for the OER. These enhancements are attributed to an increased surface area that facilitates electrolyte infiltration, improved structural integrity, and refined routes for electron and mass transport. Moreover, this method is capable of efficiently enhancing photo-induced oxidation reactions, characterized by a remarkably high current density and negligible overpotential. Research into the fundamental mechanism indicates that the enhancement in OER performance is primarily attributed to the collaborative interaction between photo-driven and electro-driven water oxidation processes. Specifically, when photogenerated electrons move from PBA to TMDs, this process not only increases the buildup of photogenerated holes in PBA but also promotes the oxidation of H_2O. Moreover, it reduces the activation energy required for OER in TMDs. This study emphasizes the photo-enhanced electrocatalytic water oxidation characteristics of PBA/TMD hybrids and proposes a possible method for designing and improving highly efficient electrocatalysts for light-induced water splitting [92].

5.3 | Phosphating-Related Materials

Furthermore, when compared with monometallic phosphides, bimetallic phosphides exhibit a higher capacity to improve the catalytic performance for the HER. Thus, the intelligent design and easy synthesis of bimetallic phosphides, with accurately controlled structures and compositions, hold considerable scientific and technological importance. Fe–Co PBA nanocones (NCs) have been effectively synthesized through an intercalation reaction approach, by employing layered α-$Co(OH)_2$ NCs as self-sacrificing templates. Following the calcination and phosphorization procedures, the Fe–Co PBA NCs can be transformed into Fe-doped Co_xP NCs while maintaining minimal structural shrinkage. Electrochemical studies show that adding Fe can significantly improve the electrocatalytic activity of Co_xP. This straightforward and efficient approach is expected to facilitate the advancement of other cobalt-based functional bimetallic compounds. Furthermore, this method could facilitate the development of synthesizing various PBA materials, featuring unique structures and novel morphologies. These materials are anticipated to function as a flexible foundation across a broad spectrum of applications, with particular emphasis on energy storage and conversion [93]. Exploring non-precious metal electrocatalysts as substitutes for noble metal-based catalysts in full water electrocatalysis remains a significant challenge when aiming for lower costs. In this study, porous ternary nickel-iron-phosphide (Ni–Fe–P) nanocubes were effectively developed by means of a one-step phosphidation process of a Ni–Fe precursor. When prepared under the ideal phosphating conditions, the Ni–Fe–P nanocubes exhibit a coarse and porous surface morphology. This characteristic facilitates improved mass transfer and promotes oxygen diffusion throughout the electrocatalytic reaction. Consequently, the Ni–Fe–P material synthesized at 350°C, although exhibiting lower crystallinity, offers a greater abundance of unsaturated atoms as active sites, which in turn enhances the adsorption and activation of reactants. Additionally, the incorporation of nickel optimizes the electronic configuration, thereby reducing the charge–transfer resistance. This facilitates accelerated electron transfer and enhances the intrinsic electrocatalytic performance. Moreover, the Ni–Fe–P nanocubes exhibit exceptional stability during continuous water splitting in a two-electrode alkaline electrolyzer. This study presents an easy yet effective approach to creating bifunctional electrocatalysts and further broadens the potential applications of MOFs in overall water splitting reactions [94]. Moreover, the deliberate fabrication regarding metal-based nanoclusters used in heterogeneous catalytic reactions involves attracted significant interest. However, achieving their fabrication while simultaneously preventing aggregation and maintaining surface activity remains a significant challenge. A recent investigation suggested the use of NiCoFe polyoxometalates (POMs) in nanocage form as a framework for the on-site distribution and stabilization of multimetallic pMP-NPs. This study presents a comprehensive approach for the in situ stabilization of pMP-NPs on PBA nanocages and highlights a novel method to increase the Gibbs free energy of the OER can be regulated by modulating the electron transfer from metallic phosphides to the PBA structure [95]. Below that, hexacyanometallates, such as PB and PBAs, represent a class of coordination compounds distinguished by their organized, porous, and open-framework structures. These substances are created through the self-assembly process involving metal ions and cyanide ligands. The evenly distributed elements within PBAs render them excellent precursors for producing hollow and highly porous nanostructures, which can include a variety of compositions. Researchers explore sophisticated methods for obtaining materials from PBAs, with an emphasis on the complex connection between synthesis processes and the resulting morphological and compositional features. Additionally, this study provides deeper insights into the catalytic and electrochemical properties that arise through various derivatization approaches. It addresses the challenges in tailoring the properties of these derivatives and presents perspectives on synthetic strategies designed for specific applications. Moreover, it provides a forward-looking analysis of underexplored areas within the field of PBA derivatives [31]. The researcher proposes a systematic approach involving electron manipulation and surface reconstruction of bimetallic phosphides (as illustrated in Figure 5a–e) to simultaneously modulate both the HER and OER activities [96]. The researcher shows that utilizing PBA as precursors, Fe-doped Ni_5P_4 nanosheet arrays on nickel foam (Fe–Ni_5P_4/NF) can be successfully fabricated and can be successfully synthesized via a simple hydrothermal process followed by phosphidation (Figure 5f–j) [97]. Furthermore, a series of ultrathin N-doped carbon-coated Fe-CoP (Fe-CoP@NC) materials are synthesized via the phosphating process of Fe–Co–Co PBA (Figure 5k,l) under different conditions, with the aim of achieving broad-spectrum photocatalytic hydrogen production [98]. Moreover, a general synthesis approach is presented for binary transition metal phosphides (TMPs) with hollow sandwich heterostructures, characterized by vertically interconnected nanosheets on all interior and exterior surfaces of the polyhedral $FeCoP_x$/C structure. This approach is demonstrated through the incorporation among different transition metals, such as Co, Fe, Cd, Mn, Cu, Cr, and Ni [99].

6 | Electrochemical Energy Storage Applications of PB and its Analogs

6.1 | Supercapacitor

In recent years, significant research and exploration have been conducted on PBA materials within the areas of energy storage

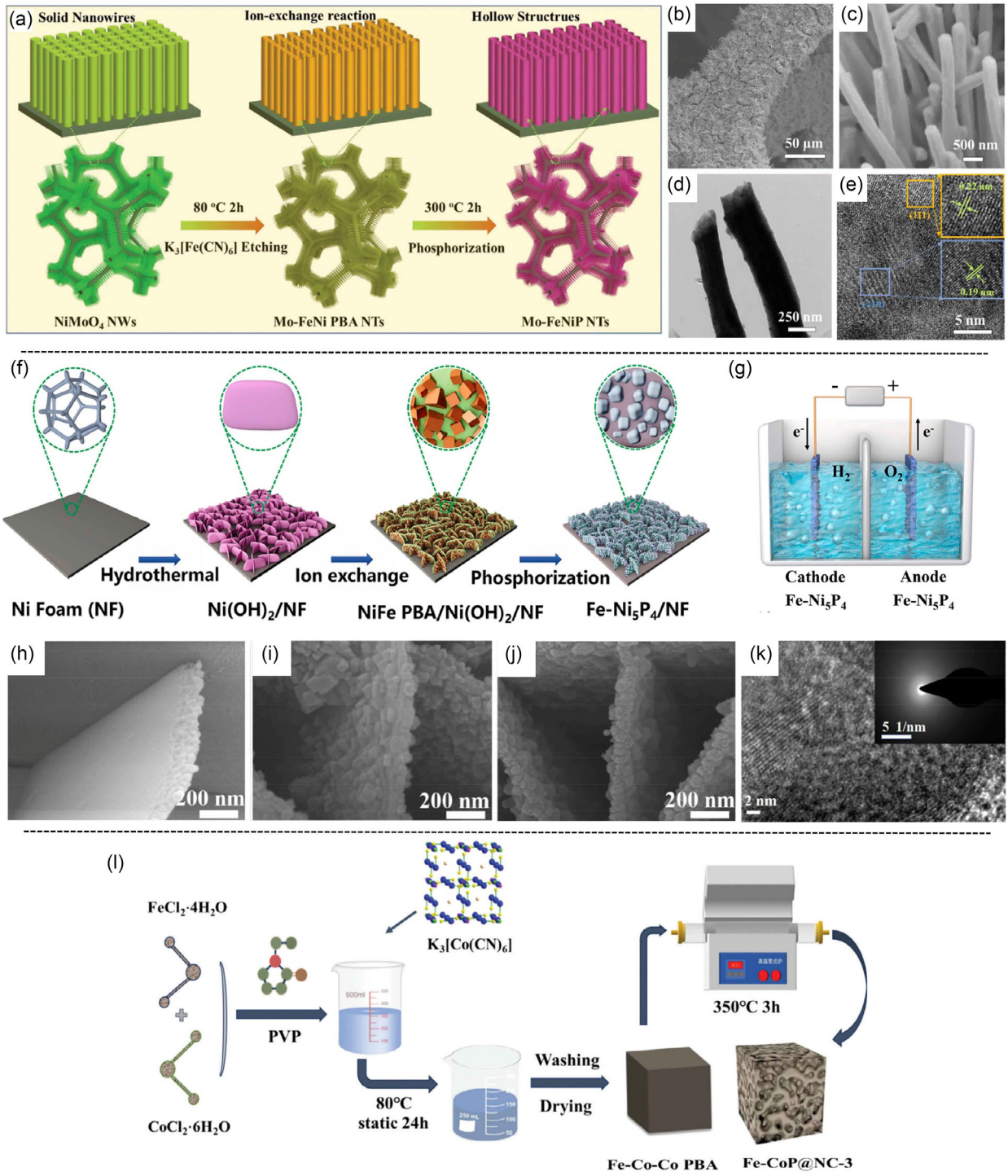

FIGURE 5 | (a) Schematic illustration of the synthesis process for Mo-FeNiP nanotubes on nickel foam. (b,c) Scanning electron microscopy (SEM) images displaying the morphology of Mo-FeNiP nanotubes. (d) TEM image and (e) HRTEM image of MoFeNiP NTs. Reprinted with permission [96]. Copyright 2024, The Authors. (f) Diagram illustrating the construction process of Fe–Ni_5P_4/NF. (g) Schematic illustration of an electrolyzer utilizing Fe–Ni_5P_4/NF for water splitting. SEM images of (h) $Ni(OH)_2$/NF, (i) NiFe PBA/$Ni(OH)_2$/NF, and (j) Fe–Ni_5P_4/NF. Reprinted with permission [97]. Copyright 2024, Hydrogen Energy Publications LLC. (k) HRTEM images of Fe-CoP@NC-3. (l) Schematic illustration of the preparation procedure for Fe-CoP@NC samples. Reprinted with permission [98]. Copyright 2024 Wiley-VCH GmbH.

and transformation. This study explores the connection between the structure and characteristics of PBA materials, which serve as host matrices for a range of charge-carrier ions such as sodium (Na^+), potassium (K^+), zinc (Zn^{2+}), magnesium (Mg^{2+}), calcium (Ca^{2+}), and aluminum (Al^{3+}). Furthermore, it highlights the strategies for optimizing PBA electrodes to achieve enhanced performance [100]. This research offers a detailed examination of PBA materials and is expected to act as a significant resource for upcoming studies and developments in PBA electrode technology [51]. Moreover, porous materials can be fabricated by

making use of MOFs with various topological structures as templates. This groundbreaking study offers a technique for controlling the structural change of uniformly sized Ce-Fe PBA and simultaneously develops a porous substance ideally suited for next-generation supercapacitors [101]. Supercapacitors are regarded as highly promising devices for energy storage and conversion. This is mainly due to their remarkable advantages, including excellent power density, long operational lifespan, fast charge/discharge capabilities, and cost efficiency. Nevertheless, the restricted low energy density hinders their wider application. Developing supercapacitors that possess an ultra-high energy density similar to batteries continues to be a significant challenge. In this research, a mesoporous hollow PBA nano-box/g-C_3N_4 composite was successfully prepared. The material demonstrates outstanding electrochemical properties, featuring a significant specific capacity of 201.6 mAh g^{-1} and excellent cycling stability (retaining 90.1% of its initial capacity after 5,000 cycles). Notably, this result exceeds the performance of most other electrode materials based on PB/PBA. Additionally, the supercapacitor exhibits exceptional cycling stability and can effortlessly power an LED indicator while maintaining efficient operation for over 3 min. The mesoporous hollow PBA nano-box/g-C_3N_4 hybrid exhibits considerable practical potential for application as a cathode material in high-performance supercapacitors [102]. Furthermore, the advancement, design, and improvement of crystalline porous materials (CPMs), such as MOFs and covalent-organic frameworks (COFs), have attracted considerable attention due to their well-defined crystalline structures and precisely tunable pore networks. Recently, significant efforts have been devoted to employing CPMs as templates for synthesizing electrochemically functional materials. These materials feature a high density of inherently electrochemically active sites, which are currently under investigation for their roles in various electrochemical processes. The focus is on understanding the electrochemically active regions and their surrounding microenvironments within CPMs, including metal ions, organic ligands, crystal arrangements, pore structures, and morphologies. Recent progress in areas such as metal-ion batteries, metal-air batteries, water electrolysis, and other related electrochemical devices has been highlighted. In summary, this review offers a deeper understanding of the advancements in electroactive CPMs by focusing on the thoughtful design and adjustment of active elements, including redox-active metal clusters and organic ligands. It also examines the spatial features around these active centers and their crucial role in electrochemical energy storage and conversion technologies [103]. Furthermore, supercapacitors (SCs), which are renowned for their capacity to provide high power output, have drawn growing interest as effective and eco-friendly energy storage alternatives. PB and PBAs are part of a category of coordination polymers, characterized by adjustable chemical compositions and an open-framework structure. PB is capable of serving as an electrode material in its native form. Due to its simple synthesis process, nontoxic property, and cost-efficiency, it has been employed to fabricate a wide range of metallic nanostructures for electrochemical applications. Researchers offer a brief summary of the charge storage mechanisms in supercapacitors (SCs) and then explore the synthesis methods for PB/PBAs and their related compounds. Following this, an extensive analysis of recent investigations into the utilization regarding PB/PBAs and their derivatives utilized as electrode materials in SCs is offered, emphasizing methodologies aimed at enhancing their electrochemical properties. Finally, key challenges are identified, and possible avenues for future exploration are suggested [104]. Considerable focus has been placed on PB and PBA, two of the most heavily researched MOFs, especially within the context of energy storage. These materials have drawn considerable attention because of their promising prospects in this area. This fascination arises due to their exceptional characteristics, including a 3D porous structure, extensive surface area, adjustable pore size distribution, and economically viable synthesis techniques. Nevertheless, their relatively low conductivity can lead to insulating behavior when used as supercapacitor electrodes, thus restricting their broader applicability, especially in high-performance electronic devices. As far as we are aware, this review seeks to offer an extensive overview of the studies focused on employing PB and PBA for the creation of supercapacitor electrodes. It explores their fabrication techniques along with their combination with other substances like graphene, carbon nanotubes (CNTs), and conductive polymers. It also highlights diverse approaches to address their drawbacks, including limited cycle life, low retention capacity, and inadequate energy/power density, thus encouraging more in-depth exploration and advancement in their utilization as supercapacitor materials [105].

6.2 | Battery

The realm of electrochemical energy storage is witnessing a paradigm shift beyond conventional lithium-ion chemistry, driven by the pursuit of sustainability, affordability, and resource availability. Sodium-ion (SIBs), potassium-ion (PIBs), and zinc-ion batteries (ZIBs) represent the vanguard of this shift, sharing the fundamental "rocking-chair" or intercalation mechanism (with the exception of ZIBs' distinct conversion chemistry in some configurations) that underpins LIBs' success, yet they diverge significantly in their operational principles and material requirements. The choice of charge carrier—Li^+, Na^+, K^+, or Zn^{2+}—imparts unique characteristics to each system, influencing key performance metrics including energy density, power capability, cycle life, and safety. SIBs capitalize on the abundance of sodium, offering a low-cost alternative; PIBs exploit the high conductivity of K^+ ions for potential high-power applications; while ZIBs benefit from the divalent nature of Zn^{2+}, aqueous electrolyte compatibility, and enhanced safety. The following systematically compares and contrasts these four ion battery technologies, elucidating their electrode materials, electrolyte formulations, interface engineering, and device architectures, with the goal of identifying existing challenges and highlighting promising avenues for future research to advance the field of next-generation energy storage.

6.2.1 | Lithium-Ion Battery

Manganese-based PBAs (Mn-PBAs), characterized by their 3D metal-organic scaffold and numerous redox-active centers, have garnered significant attention for use in ZIBs (Figure 6). However, the Jahn–Teller effect and disproportionation reactions associated with Mn^{3+} often lead to inferior electrochemical performance and compromised structural stability. To mitigate these issues, researchers developed a HE-PBA by incorporating five transition metals—manganese, cobalt, nickel, iron, and copper—were incorporated into lattice positions coordinated by nitrogen. This strategy not only enhances configurational entropy but also stabilizes the crystal structure through the

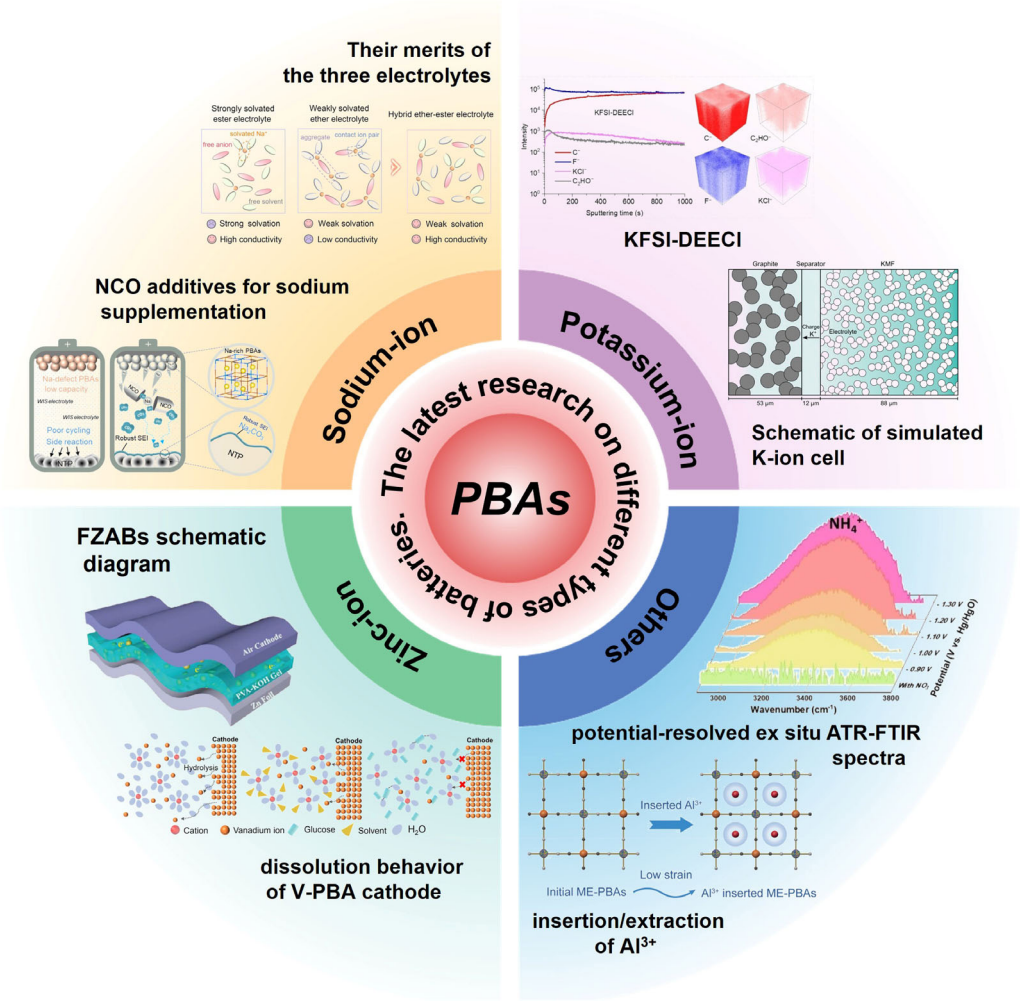

FIGURE 6 | The latest research of PBAs in sodium ion, potassium ion, zinc ion battery, and other batteries.

synergistic interactions of multiple transition metals. Consequently, the HE-PBA exhibits superior Zn^{2+} storage capacity, achieving a remarkable 80 mAh g^{-1}. Moreover, within the HE-PBA cathode, a transformation phase from monoclinic to rhombohedral is detected. This results in a stable configuration where MN_6 (M = Mn, Co, Fe, Ni, Cu) is connected to ZnN_4 through FeC_6 via cyanide bridges. Moreover, the benefits of entropy-driven stability are confirmed through a comparison of the calculated reduction energy and density of states for HE-PBA and $KMn[Fe(CN)_6]$ (KMnHCF). This research not only demonstrates an exceptionally efficient HE-PBA cathode for ZIBs but also proposes a new approach rooted in high-entropy concepts for developing advanced materials [106]. Moreover, LIBs have been instrumental in enabling the wireless advancement of portable digital devices. However, to meet the demands of more sophisticated applications, such as extensive energy storage systems and next-generation portable devices, it is essential to improve the energy density, power density, and cycle life of LIBs [107]. This can be achieved by enhancing the electrochemical characteristics of the three primary elements: the cathode, anode, and electrolyte. Beyond LIBs, LMBs have drawn significant attention owing to their extremely high energy density, primarily attributed to the lithium–metal anode. Nevertheless, the present efficiency of LMBs is limited by major obstacles, such as the formation of dendrites and insufficient contact at the electrode–electrolyte interface. Scientists highlight the essential role of coordination chemistry in improving both LIBs [108] and LMBs. This is especially significant for the development of next-generation electrode and electrolyte materials, as these depend on coordination compounds featuring well-defined molecular architectures. The examination initiates with an overview of the progression in coordination chemistry, extending from individual coordination compounds to coordination polymers and metal-organic frameworks. Subsequently, the authors explore the design principles of coordination compounds specifically developed for lithium storage and lithium-ion transport. A comprehensive analysis is provided on various strategies to enhance the electrochemical properties, operational voltage, capacity, cycling stability, and rate capability of electrodes based on coordination compounds. Additionally, the review provides an in-depth exploration of reticular chemistry, which allows metal-organic frameworks to achieve ideal structures and pore dimensions for effective lithium-ion conduction when used as electrolytes. Finally, the present challenges and potential avenues for future research in coordination chemistry for LIBs and LMBs are emphasized [109]. PBAs are regarded as promising candidates for anode materials in Li^+ storage because of their adaptable compositions, customizable structures, and tunable porous frameworks. Nonetheless, these materials face challenges such as substantial capacity loss and inadequate cycling stability, primarily caused by volume variations during the

lithiation/delithiation cycles and their inherently high electrical resistance. To overcome these limitations, researchers have developed a general method for generating small PBA nanoparticles anchored regarding 2D MXene or reduced graphene oxide substrates. This method encompasses an in situ conversion process originating from ultrathin LDH nanosheets. Two-dimensional conductive nanosheets enable fast electron transfer, which helps maintain the efficient use of PBA even at high rates. Concurrently, PBA nanoparticles effectively suppress the reaggregation of 2D materials while enhancing swift ion diffusion. When used as an anode in LIBs, the optimized $Ni_{0.8}Mn_{0.2}$-PBA/MX delivers a capacity of 442 mAh g^{-1} at a current density of 0.1 A g^{-1} and shows enhanced cycling stability in comparison to bare PBA bulk crystals. Researchers believe that this research introduces a novel method for creating PBA-based electrode materials specifically tailored for application in energy storage systems [110]. Moreover, the lithium metal anode, considered a potential candidate for next-generation lithium battery technology, faces considerable obstacles, including dramatic volume fluctuations and uneven lithium plating/stripping processes. To address these issues, researchers have developed a lightweight lithiophilic PBA with a honeycomb-like structure on copper foam via a self-assembly approach. This unique honeycomb architecture provides expanded surface areas and multiple deposition sites, enabling uniform distribution of the Li^+ flux during plating. Consequently, the carefully designed PBA-modified Cu foam current collector achieves stable long-term performance (up to 1800 h) for reversible lithium plating/stripping, accompanied by a significantly enhanced Coulombic efficiency (reaching 98.3% after 350 cycles). The direct self-assembly synthesis method applied to metal foam offers innovative strategies for designing lightweight 3D current collectors specifically tailored for lithium metal anodes [111].

The shuttle effect and poor conductivity lead to capacity fading, which poses a significant challenge for the commercialization of LSBs. To tackle this issue, researchers have developed a sulfur electrode material by employing a polypyrrole composite encapsulated with a nickel-manganese Prussian blue analog (3-MnNi-PBA@S@PPy). This composite exhibits strong chemical adsorption for polysulfides (LiPSs) along with remarkable catalytic activity, successfully restricting LiPSs and promoting their transformation. Within the 3-MnNi-PBA@S@PPy structure, the outer layer of 3-MnNi-PBA naturally reacts with polysulfides to create thiosulfate salt intermediates, which enhances polysulfide conversion and substantially boosts the overall electrochemical performance. By taking advantage of the previously discussed benefits, 3-MnNi-PBA@S@PPy composites were employed as cathode materials in LSBs. At a current density of 0.1 C, the composites demonstrated an outstanding initial capacity of 1285 mAh/g and maintained excellent cycling stability. Moreover, upon testing at an elevated current density of 0.5 C for 500 cycles, the decline in capacity was as low as 0.07% per cycle. The MnNi-PBA material exhibits a unique heterogeneous interface catalytic mechanism that effectively reduces the shuttle effect in LSBs, thus underscoring its significant potential for real-world applications [112]. Furthermore, the logical design, simple fabrication, and practical implementation of electrodes made from double-shelled hollow structures with accurate morphologies and diverse components continue to pose substantial challenges. In this study, the research team effectively synthesized double-shelled Ni-Fe-P/N-doped carbon nanoboxes (referred to subsequently as Ni-Fe-P/NC). These materials were then employed as electrode components for potassium-ion batteries and lithium-sulfur batteries. These unique structures not only effectively reduce volume changes and avoid the aggregation of Ni-Fe-P/NC during the cycling process but also provide extensive surface areas to enhance electrolyte infiltration. Moreover, the incorporation of nitrogen-doped carbon (NC) can significantly enhance the electrical conductivity of the electrode. Consequently, when Ni-Fe-P/NC nanoboxes are employed as anode materials in potassium-ion batteries (KIBs), they exhibit exceptional cycling stability. Simultaneously, Ni-Fe-P/NC can function as an effective sulfur host material in LSBs due to its unique hollow structure. It is capable of supporting high sulfur content while also successfully restraining polysulfides through strong chemical bonds [113]. So far, the incorporation of high-entropy materials into PBAs has not been widely explored within the domain of LSB materials. In this study, the researchers successfully created a wide range of PBAs, spanning from binary to high-entropy compositions, using a simple co-precipitation method. The organization of components within these PBAs was investigated through XAFS spectroscopy, and elemental mapping confirmed the uniform incorporation of all metallic elements. Crucially, electrochemical assessments revealed that high-entropy PBAs function efficiently as polysulfide stabilizers to reduce the shuttle effect and also serve as catalysts to facilitate polysulfide transformation, thus enhancing overall performance substantially. Moreover, various nanocubic metal oxides, extending from binary to six-component systems, were prepared by utilizing PBAs as sacrificial precursors. The researchers have faith that the extensive array of novel materials generated through their coprecipitation and pyrolysis strategy will inspire further progress in PBA system research and sulfur host material development [114]. Furthermore, the advancement of Li-S batteries faces substantial obstacles, such as the polysulfide shuttle effect and insufficient electronic conductivity. To tackle these issues simultaneously, a novel strategy has been proposed, integrating the benefits of PBAs and the conductive properties of polypyrrole (ppy) for the creation of an FeCoNi PBA-S-ppy composite. The available metal centers in PBAs act as Lewis acid sites and exhibit a strong attraction to negatively charged polysulfide anions. Additionally, the porous structure with open channels enables efficient sulfur incorporation while effectively suppressing the migration of LiPS. The process and dynamics of the polysulfide redox reaction are elucidated through in situ X-ray diffraction analysis. Comprehensive assessments, including adsorption capability tests, electrochemical performance evaluations, and density functional theory computations verify that FeCoNi PBA demonstrates superior lithium polysulfide (LiPS) absorption and cycling stability compared to FeNi and FeCo PBAs. This enhancement can be credited to the multi-metal synergistic effect in FeCoNi PBA, which functions as an effective chemical anchor for trapping LiPS molecules. The researchers conclude that PBAs can effectively ensure the stability and efficiency of Li-S batteries [115]. Moreover, soluble lithium polysulfides (LiPSs) in Li-S batteries exhibit a significant "shuttle effect," leading to sluggish sulfur redox reaction kinetics and rapid capacity degradation. This presents a significant hurdle for the widespread commercial adoption of Li-S batteries. To address this challenge, cascade catalysis is implemented by using a self-regenerating catalyst featuring multiple active sites. During this entire process, the In/O and In/Zn active sites undergo dynamic reactivation through a switching catalytic mechanism. This facilitates the self-restoration of the active sites, thereby improving their long-term catalytic stability. This

research shows that cascade catalysis can be realized by employing self-regenerating catalysts with multiple active sites for LiPSs. This offers fresh perspectives on the development of multifunctional catalysts for effectively managing the redox reactions of LiPSs [116]. Owing to their reasonable cost and remarkable theoretical energy density, LiSBs [117] are considered highly promising candidates for next-generation energy storage systems. However, despite notable progress in recent years, the ongoing issue of polysulfide (PS) migration during battery function continues to hinder the commercial viability of LiSBs. This problem is particularly exacerbated under practical conditions, making it a significant challenge to overcome. This study proposes a permselective ionic barrier strategically positioned between the electrodes, which effectively suppresses polysulfide migration while enabling unhindered lithium-ion transport, thereby significantly enhancing the electrochemical performance of LiSBs. The barrier is facilely fabricated on the separator via robust ionic interactions and intermolecular bonding with functionalized polymers, leading to improved battery efficiency and safety. Furthermore, the research comprehensively examines the performance of LiSBs under real-world operating conditions to enhance the system's overall equilibrium for attaining high energy densities. Such findings offer essential perspectives for the advancement of specialized separators designed for commercially feasible lithium-sulfur batteries [118].

6.2.2 | Sodium-Ion Battery

Materials with 3D framework structures, such as PB and PBA, have been shown to be crucial in the development of SIBs. Researchers have developed a simple self-template approach for creating hollow-structured PBA, specifically CoFePBA. This design not only successfully adapts to volume fluctuations during the processes of ion insertion and extraction but also substantially reduces the ion diffusion distance, thus improving electrochemical performance. Additionally, in situ X-ray diffraction analysis confirms that CoFe-PBA@PDA maintains its reversible structure without forming any new phases during electrochemical cycling. This research offers a novel design method or technique to improve the structural integrity and electrochemical characteristics of PBA cathodes for SIBs [119, 120]. Furthermore, PBAs are promising candidates as cathode materials for SIBs; however, many PBAs face a trade-off between high capacity and structural stability. This study proposes a new type of disodium ethylenediaminetetraacetate hydrothermal method assisted by (Na_2EDTA) for synthesizing monoclinic nickel-rich PBA cathodes doped with iron (H-PBA) for efficient sodium ion storage. The engineered H-PBA cathode combines the minimal strain advantage of a nickel-based PBA structure with the enhanced capacity enabled by nitrogen-supported Fe^{3+}/Fe^{2+} redox centers. It exhibits remarkable ability of sodium storage in terms of capacity and rate capability and cycling stability. Moreover, ex situ studies indicate that during the charging and discharging cycles, solid solution reactions take place between 2.0 and 3.0 V, while phase transition reactions occur within the range of 3.0–4.0 V. This allows the H-PBA framework to hold roughly 1.5 Na^+ ions for storage.

At the same time, the H-PBA//$NaTi_2(PO_4)_3$@C full cell exhibits outstanding electrochemical characteristics. Looking ahead, this study is anticipated to support the practical application of SIBs in extensive grid energy storage systems [121]. Moreover, it has been suggested that a concentration-gradient structure can serve as a highly efficient approach to reduce mechanical deterioration and improve the electrochemical cycling durability of sodium-ion battery cathodes. By employing a simple co-precipitation method, $Na_xNi_yMn_{1-y}Fe(CN)_6{\cdot}nH_2O$ particles with a gradient nickel distribution—from low concentrations in the core to high levels at the surface—were successfully synthesized. When employed as active materials in cathodes, these particles demonstrated superior electrochemical performance in comparison to homogeneous $Na_xMnFe(CN)_6{\cdot}nH_2O$. They obtained a high reversible specific capacity of 110 mAh g^{-1} at 0.2C, along with demonstrating outstanding cycling stability (retaining 93% of their capacity after 1000 cycles at 5C). Electron microscopy analysis showed that the enhanced electrochemical properties of the gradient structure were attributed to its strong microstructure. This feature successfully mitigated the stresses and cumulative damage induced by sodium intercalation/deintercalation processes, thereby avoiding the fractures typically encountered in homogeneous materials. These results provide essential perspectives for the intelligent development of advanced electrode materials in sodium-ion batteries [122]. As presented in Table 1, among the advanced cathode materials for SIBs.

Moreover, NIBs and KIBs are considered to be extremely promising alternatives for future electric energy storage systems, owing to their reduced costs and similar energy/power densities compared to Li^+ batteries. In the quest for effective electrode materials for NIBs and KIBs, PBAs have demonstrated remarkable potential. This is attributed to their sturdy, open-framework architectures and extensive interstitial spaces, which enable the reversible intercalation of larger alkali metal ions while maintaining structural integrity. This review explores the techniques and accomplishments in enhancing the characteristics of HCF materials, such as composition refinement, crystal water management, increased crystallinity, shape regulation, and boosted electronic conductivity. The objective is to deepen the comprehension of these materials and offer fresh perspectives for the further development of PBAs designed for advanced rechargeable battery applications [123]. Moreover, SIBs have drawn significant focus in the area of energy storage systems because of the abundant availability of their constituent materials and their cost-effectiveness. In order to attain the best balance between efficiency and expense, both the positive and negative electrode materials require additional refinement. Electrolytes play a crucial role in SIBs and are required to possess wide electrochemical stability windows, outstanding thermal stability, and effective ion transport characteristics. To address the practical requirements of SIBs, sophisticated electrolyte systems have been designed, utilizing diverse materials and compositions. These include organic-based electrolytes, ionic liquids, water-in-salt electrolytes, solid-state electrolytes, and hybrid systems. Although well-developed organic electrolytes are predominant in today's manufacturing processes, aqueous and solid electrolytes offer significant potential for future use, as will be elaborated in the following sections. Recent advancements have centered on modifying electrolytes to improve their compatibility with electrodes at the interface, thereby enhancing battery longevity and safety. This article offers an in-depth examination of sophisticated characterization methods used to analyze the characteristics of electrolytes and electrode interfaces. Additionally, it clarifies the reaction mechanisms and deterioration processes associated with

TABLE 1 | The electrochemical characteristics of the most advanced cathode materials for sodium-ion batteries, as reported in the past 2 years (TMO is the abbreviation of "transition metal oxide", PA is the abbreviation of "polyanion").

Electrode material	Capacity, (mAh g^{-1}@mA g^{-1})	Cycle life, (cycles, retention %@ mAg^{-1})	Rate performance, (mAh g^{-1}@mA g^{-1})
(Ni, Mn)-TMO	103@22	3000, 68@480	67@1600
Mn-LO	241@22	100, 98@50	110.2@2000
(Ni, Co, Mn, Mg)-LO	154@16	200, 81@320	98@800
(Ni, Ru)-LO	130@7	1000, 81@130	57@1300
$Na_4MnCr(PO_4)_3$/C-PA	114@11	600, 87@550	27@1650
$Na_3Ti_{0.5}V_{0.5}(PO3)_3N$-PA	91@8	3000, 86@1600	60@1600
Na $_3V_{1.5}Cr_{0.5}(PO_4)_3$-PA	163@15	2650, 72@750	128@1500
$Na_2Fe(C_2O_4)$SO4-PA	170@45	500, 85@44	54@440
Ni-based PBAs	83@8.5	3500, 93@850	75@1700
Fe-based PBAs	116@10	500, 71@100	70@200
Fe- based PBAs	145@15	3500, 59@750	94@1500
Mn-based PBAs	137@25	2700, 72@500	105@500

SIBs. Moving forward, the practical feasibility of SIBs is expected when paired with high-efficiency electrolytes that effectively complement electrodes. To promote the development of next-generation SIBs, targeted suggestions are presented [124].

Possessing numerous advantages, PBAs have emerged as exceptional cathode substances utilized for SIBs. Nevertheless, the practical implementation of these materials remains constrained by issues like inadequate stability, prominent $[Fe(CN)_6]$ defects, and residual moisture within the structure, mainly resulting from fast crystal formation. To overcome these limitations, a "water-in-salt" nanoreactor strategy has been developed, enabling the synthesis of PBAs with improved crystallinity, fewer defects, and significantly reduced water content. The enhanced PBAs exhibit outstanding specific capacity and rate performance when used in SIBs. Furthermore, evaluations of air-stability, adaptability to all climates, and full-cell characteristics suggest that our PBA achieves significantly improved electrochemical performance and a greater volumetric energy density than those synthesized using traditional water-based co-precipitation techniques. Furthermore, the excellent reversibility of sodium-ion storage in these materials has been thoroughly examined and confirmed using a variety of in situ characterization methods. This research not only offers essential perspectives for the intelligent design of PBAs but also opens new avenues for their expanded use in large-scale energy storage solutions [125].

In addition, a SSS electrolyte exhibiting an ionic conductivity of 2.6×10^{-3} S cm^{-1} has been effectively created. This innovation is specifically designed to mitigate the challenges associated with interfacial side reactions commonly observed in conventional liquid carbonate electrolytes used in PB-based sodium-ion batteries, as well as to suppress sodium dendrite growth. The solidification process is initiated via the polymerization of fluoroethylene carbonate (FEC), which is triggered by the addition of 5 wt% $AlCl_3$ Lewis acid into the original liquid electrolyte. The SSS electrolyte plays a crucial role in substantially improving the inherent reversibility of the rhombohedral PBA (r-PBA) cathode material. This enhancement results in an exceptional cycling lifespan, achieving 3000 cycles at a current rate of 1C and 4000 cycles at 2C. Additionally, it exhibits the material exhibits high-rate capacities of 121 mAh g^{-1} at 1C and 88 mAh g^{-1} at 10C, demonstrating its excellent performance under different current rates. The significant improvements in both cycling stability and rate capability are mainly attributed to the strengthened interface between the r-PBA and the electrolyte. This is achieved through the development of a protective poly(vinylene carbonate) layer on the surface of the r-PBA. This study underscores the pivotal role of interface stability in preserving the rhombohedral structure of PBAs, providing valuable insights for advancing this field [126].

Moreover, PBAs, including copper hexacyanoferrate (CuHCF), have been extensively studied as conventional intercalation sodium-ion battery cathode materials. However, the electrochemical performance of these PBAs is often limited by insufficient activation and rapid capacity fading. To address the challenges of low electrochemical activity and structural instability in CuHCF cathodes, various approaches have been devised to improve both specific capacity and cycling performance. Through a pyrophosphate-assisted co-precipitation technique, CuHCF nanosheets exhibiting high crystallinity with minimized water content (referred to as CuHCF-P) were effectively produced. The substance exhibits an extraordinarily reversible 1.5-Na insertion/extraction capability, achieving a specific capacity of ≈120 mAh g^{-1} at a 0.1C rate. This corresponds to the highest value reported to date for CuHCF cathodes. A joint approach using first-principles calculations and XPS analysis indicates that both Cu and Fe function as redox-active sites in the CuHCF-P cathode, greatly improving its exceptional ability to store Na^+ [127]. Reducing the water content within the CuHCF framework increases the occupancy of Fe/Cu 3d orbitals, thereby activating both transition metals. Moreover, fully assembled cells featuring the synthesized CuHCF-P cathode and a commercially sourced hard carbon anode demonstrate outstanding performance, maintaining a reversible capacity of 109 mAh g^{-1} at 0.1C over 200 cycles [128]. As a potential cathode material for sodium-ion

batteries, the crystallinity of PB/PBA plays a key role in affecting the electrochemical reaction kinetics and the longevity of the material. If it is lower than optimal, this can significantly affect performance and stability over time. However, achieving controllable adjustment of PB/PBA crystallinity remains a significant challenge. In this research, scientists introduce a harmonized approach to synthesize low-defect PB (LD-PB) materials, showcasing excellent capabilities for sodium energy storage. Sodium carboxymethylcellulose serves as a gentle chelating agent to efficiently control the precipitation of LD-PB, resulting in a structure that has few vacancies and contains negligible crystal water molecules. The highly crystalline open structure facilitates extraordinarily fast and completely reversible sodium insertion and removal. Remarkably, even at an ultra-high rate of 100 C, a specific capacity of 101 mAh g^{-1} is attained, along with an outstanding capacity retention of 97.4% after 3000 cycles. This research provides essential understandings of the balanced coordination approach to enhance PB/PBA cathode materials, which in turn advances ultrafast and long-lasting alkalimetal energy storage [129].

Furthermore, the simultaneous adjustment of both chemical composition and morphological structure results in the creation of a hollow monoclinic high-entropy MHCF (Figure 7a), termed HMHE-HCF [130] assembled by nanocubes for the first time to realize the objective. In addition, seven Cobalt-Mbased (M = V, Mn, Fe, Co, Ni, Cu, Zn) PBAs (CoM-PBAs) are designed as anodes for SIBs via a universal low-energy co-precipitation approach (Figure 7b) with the strategic inclusion of 3d transition metals [131]. Researchers proposed for the first time that $[Fe(CN)_6]$ vacancies play a crucial role in achieving high specific capacity. These vacancies are likely to introduce additional net electrons while reducing barriers to ionic transport, thereby improving the electronic (as depicted in Figure 7c,d) and ionic conductivity of PBAs, which in turn enhances their rate performance [132]. A balance between optimizing the anion-reinforced solvation structure and achieving high ionic conductivity is achieved via the entropy-assisted hybrid ester-ether electrolyte, as depicted in Figure 7e,f [133]. In addition, we introduce $Na_2C_4O_4$ additives as sodium sources to compensate for sodium deficiencies in PBAs. Meanwhile, the CO_2 released from the thermal decomposition of $Na_2C_4O_4$ is utilized to form a stable SEI layer enriched with Na_2CO_3 components (as depicted in Figure 7g) [134]. Furthermore, we present an alkaline aqueous sodium-ion battery featuring a manganese-based PBA cathode (Figure 7h), which demonstrates a remarkable long cycle life of 13,000 cycles at 10 C, while providing a high energy density of 88.9 Wh kg^{-1} at 0.5 C [135]. Furthermore, this research takes the lead in applying an innovative equilibrium chelation technique for the synthesis of PBAs, achieving high crystallinity at 94.7%. This is achieved by finely tuning the chelating strength of potent chelating agents via the "acid effect," thereby attaining optimal chelating capability and effectively addressing the limitation of insufficient cyclic stability in PBA cathodes [136]. Despite extensive experimental efforts to remove interstitial water in order to enhance capacity, a thorough comprehension of the low capacity of low-spin Fe, which is critical for Na^+ storage, remains insufficient [137]. In addition, a balancing strategy is implemented to sustain the equilibrium between interstitial water replenishment and water-induced degradation. To illustrate this concept, xCS (x, ratio; CS, co-solvent, such as polyethylene glycol or trimethyl phosphate) balanced electrolytes are utilized to mitigate the issue of rapid performance decline [138]. Furthermore, a one-pot synthesis approach has been established for the creation of MnFe PBA open frameworks. These architectures are subsequently employed as cathode materials in sodium-ion batteries [139].

Moreover, sodium nickel ferrocyanide ($Na_{1.34}Ni[Fe(CN)_6]_{0.92}$, NNHCF) is regarded as a potential cathode material for SIBs because of its distinctive structural characteristics and excellent sodium storage capability [140]. In addition, a series of isostructural PBAs samples have been successfully synthesized, and the isostructural transformation of PBAs from cubic to monoclinic upon condition adjustment has been clearly observed [141]. Furthermore, a set of highly crystalline iron-based PBA cubes, where HCF stands for hexacyanoferrate, is fabricated through a single-step pyrophosphate-assisted co-precipitation method [142]. Furthermore, a disordered and sodium-deficient NASICON structure, $Na_{4-x}Mn(FeVCrTi)_{0.25}(PO_4)_3$ (hereafter referred to as $Na_{4-x}Mn(HE)$), is developed and constructed to efficiently reduce the Jahn–Teller effect, thereby realizing a high-performance and extremely stable cathode material for sodium-ion batteries [143]. Furthermore, this study seeks to tackle this challenge by incorporating highly stable AMnHCF (with A representing K, Rb, or Cs) via a simple approach for combination with NaMnHCF [144].

6.2.3 | Potassium-Ion Battery

Ether-based electrolytes are essential for achieving superior low-temperature performance and high ionic conductivity in potassium ion batteries. However, conventional dilute ether-based electrolytes often encounter challenges such as the co-intercalation of ions and solvents into graphite, poor cycling stability, and difficulty in supporting high-voltage cathodes above 4.0 V. To address these issues, an electron-withdrawing group (chloro-substitution) was introduced (as illustrated in Figure 8a–c). This modification effectively modulates the SEI and enhances the oxidative stability of ether-based electrolytes. Specifically, the chloro-functionalized ether-based electrolyte at a low concentration (≈0.91 M) not only facilitates the formation of a uniform dual halide-based SEI but also substantially reduces aluminum corrosion under high-voltage conditions. By utilizing the functionalized electrolyte, the Kj jgraphite cell exhibits remarkable stability for up to 700 cycles. The Kj jPB cell (4.3 V) exhibits a durability of up to 500 cycles [145]. Furthermore, PIBs, which do not depend on strategically critical and often costly elements such as lithium, nickel, cobalt, or copper, are considered potential electrochemical energy storage alternatives that are both low-cost and environmentally sustainable that could serve as complements to current LIBs. Nevertheless, the electrochemical performance of PIBs remains less than ideal, particularly when produced under real-world battery manufacturing conditions. The main challenge arises from the absence of electrolytes that can adequately support both the low-voltage anode and the high-voltage cathode, which is essential for achieving acceptable Coulombic efficiency (CE) and maintaining long-term cycling stability (as shown in Figure 8d,e). Researchers introduce an innovative electrolyte. This electrolyte exhibits remarkable compatibility with the high-voltage $K_2Mn[Fe(CN)_6]$ (KMF) cathode operating at 4.4 V (vs. K^+/K). As a result, the KMF ‖ graphite full cell, with no prior electrode treatment, achieves an average discharge

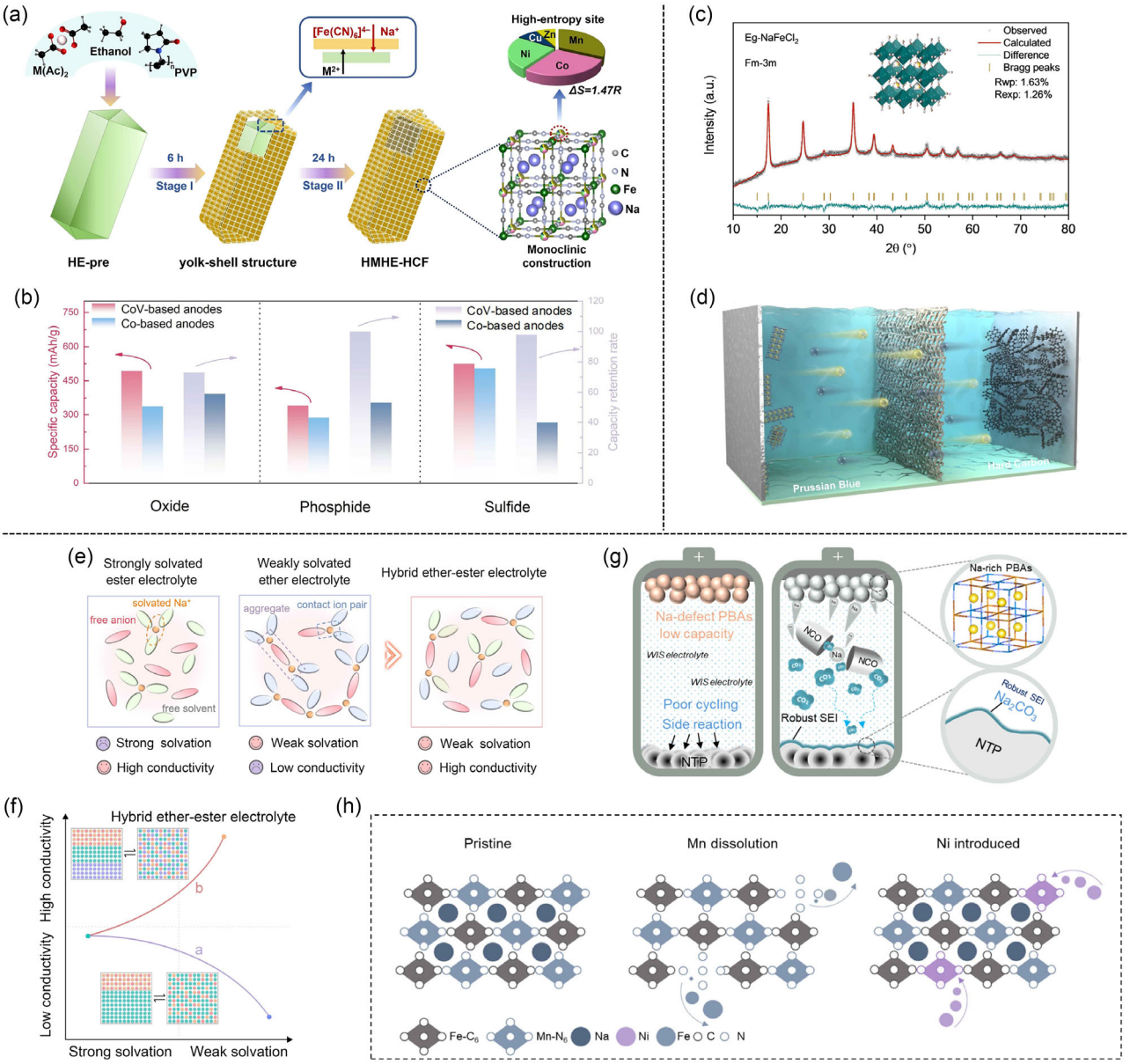

FIGURE 7 | (a) Diagrammatic representation of the fabrication procedure and crystalline structure of HMHE-HCF. Reprinted with permission [130]. Copyright 2024, Wiley-VCH GmbH. (b) The comparisons of the SIBs performance between Co-based and CoVbased anodes (oxide, phosphide, sulfide). Reprinted with permission [131]. Copyright 2025, Wiley-VCH GmbH. (c) XRD pattern of Eg-$NaFeCl_2$. (d) Schematic diagram of the full batteries. Reprinted with permission [132]. Copyright 2024, Wiley-VCH GmbH. (e) Schematics of solvation structure and their merits of the three electrolytes. (f) Schematic illustration of weakly solvated electrolyte (path f) and hybrid ester-ether electrolyte (path e). Reprinted with permission [133]. Copyright 2024, Wiley-VCH GmbH. (g) Schematic illustration of NCO additives for sodium supplementation with simultaneous construction of SEI interface in PBA-based full ANIBs. Reprinted with permission [134]. Copyright 2025, American Chemical Society. (h) Suggested Ni/C coating design to tackle the structural instability resulting from Mn dissolution in NMF cathodes. Reprinted with permission [135]. Copyright 2024, Springer Nature.

voltage of 3.61 V and a specific energy of 316.5 Wh kg^{-1} (calculated based on KMF + graphite). This performance is comparable to that of $LiFePO_4$ || graphite lithium-ion batteries. Moreover, after 2000 cycles, it preserves 71.01% of its original capacity [146]. Furthermore, KIBs are gaining more interest as a potential substitute for LIBs, primarily because they lessen the dependence on critical minerals. KIBs demonstrate enhanced fast-charging abilities in comparison to LIBs, as evidenced by the markedly quicker transport kinetics of K-ion electrolytes reported in recent research. Nevertheless, due to the lack of a commercially practical K-ion electrolyte, it is crucial to develop a full-cell rate model for KIBs that aligns with current commercial cell architectures. This model would enable an accurate evaluation of the fast-charging capabilities of KIBs. In this research, the solid-state diffusivities and exchange current densities of the graphite anode and the potassium manganese hexacyanoferrate $K_2Mn[Fe(CN)_6]$ (KMF) cathode were successfully assessed (Figure 8f–h). This was achieved by combining advanced analytical methods with refined material design strategies. Ultimately, researchers present a Doyle–Fuller–Newman model adapted for a KIB full cell, integrating practical geometry and loadings, to identify the key material properties that limit their rate performance [147].

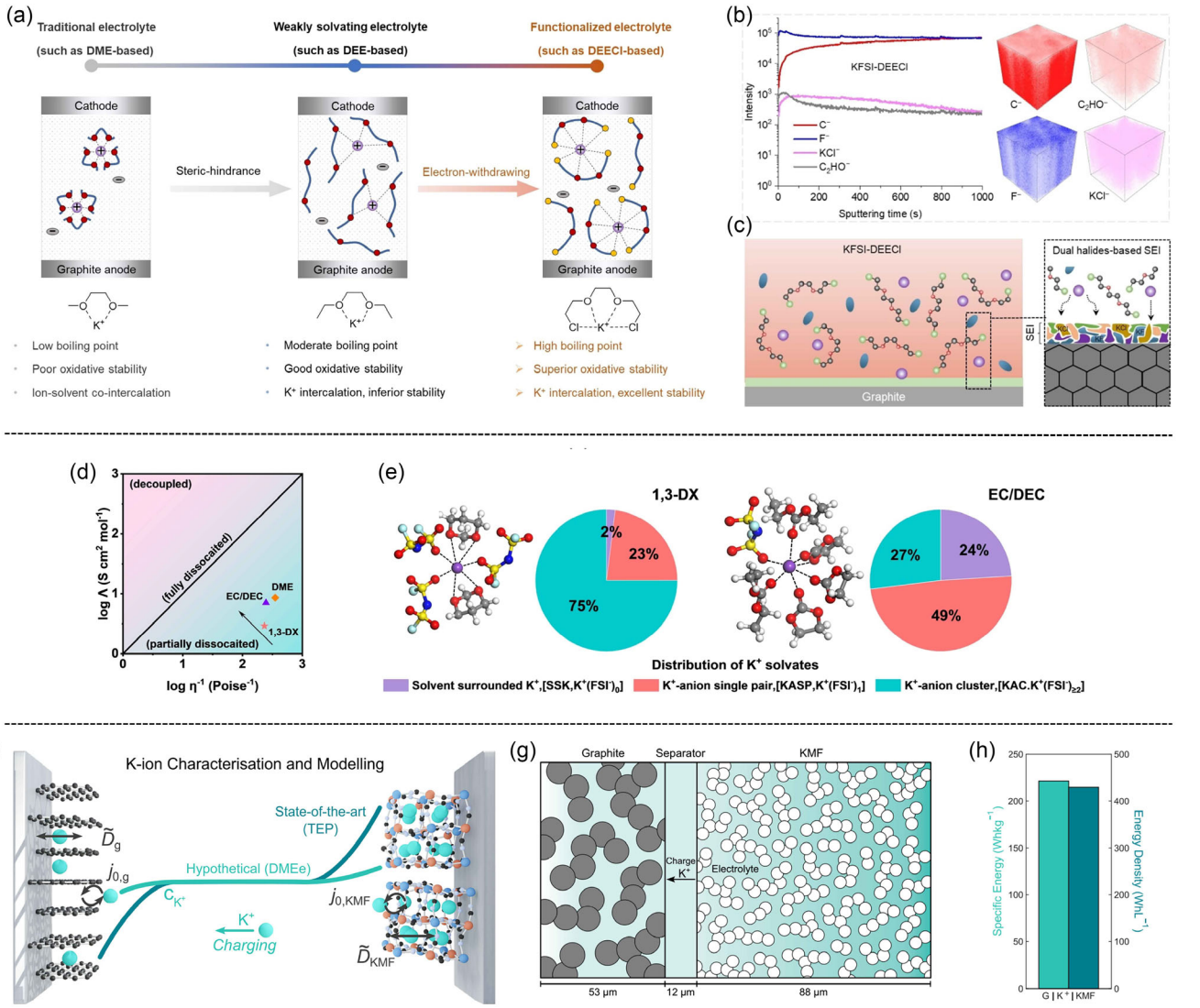

FIGURE 8 | (a) Design concept of the functionalized ether-based electrolyte. ToF-SIMS characterizations under (b) KFSI-DEECl. (c) The illustrate of dual halides-based SEI formation on graphite electrode when using KFSIDEECl electrolyte. Reprinted with permission [145]. Copyright 2024, Wiley-VCH GmbH. The Walden plot (d). (e) The most probable solvation structures of the primary K^+ solvation sheath from the cMD simulations and the distribution of different K^+ solvates, i.e., SSK, KASP, and KAC. Reprinted with permission [146]. Copyright 2024, Wiley-VCH GmbH. (f) K-ion characterization and modeling. (g) Diagram of the simulated K-ion cell. (h) Energy density and specific capacity of the K-ion chemistry at the stack level, as evaluated using the previously developed stack-level model. Reprinted with permission [147]. Copyright 2024, Springer Nature.

6.2.4 | Zinc-Ion Battery

Advancing flexible ZABs relies heavily on the creation of an integrated air cathode that exhibits improved ORR performance. This is essential as ZABs play a key role in providing power for wearable electronic devices. In this research, we introduce a self-assembly MOF-derived approach to create an atomic Fe/Fe_3C@N-doped C catalyst attached to CC, which is designed for application as an air cathode in flexible ZABs (Figure 9a–c). The precursor of PB, which forms spontaneously on the carbon cloth surface via electrostatic interactions, ensures the uniform distribution and high loading density of the catalyst on the carbon cloth substrate, thereby playing a key role in the overall performance enhancement. The hollow cubic architecture, along with an N-doped carbon layer and a well-integrated electrode design, improves the exposure of active sites and facilitates efficient electron transfer and mass transport. DFT analyses indicate that the electronic coupling between Fe-N_4 and Fe_3C dual active sites can significantly influence the adsorption and desorption behavior of oxygen intermediates generated during the ORR process. As a result, the Fe/Fe_3C@N-doped C/CC material demonstrates a notable half-wave potential ($E_{1/2} = 0.903$ V) and outstanding long-term stability in alkaline environments. Owing to its exceptional ORR performance, ZABs and flexible ZABs that utilize the Fe/Fe_3C@N-doped C/CC air cathode exhibit remarkable overall electrochemical characteristics, including open-circuit voltage, peak power density, flexibility, and cycling stability [148]. Moreover, PBAs have been widely investigated as host materials for aqueous ZIBs. Nevertheless, they encounter substantial obstacles, such as limited capacity and inadequate cycling stability. These issues are mainly due to restricted electron transfer rates and the existence of interstitial water in the PBA structure. A silver hexacyanoferrate material, $K_{0.95}Ag_{3.05}Fe(CN)_6$ (referred to as AgHCF-3), which is free of

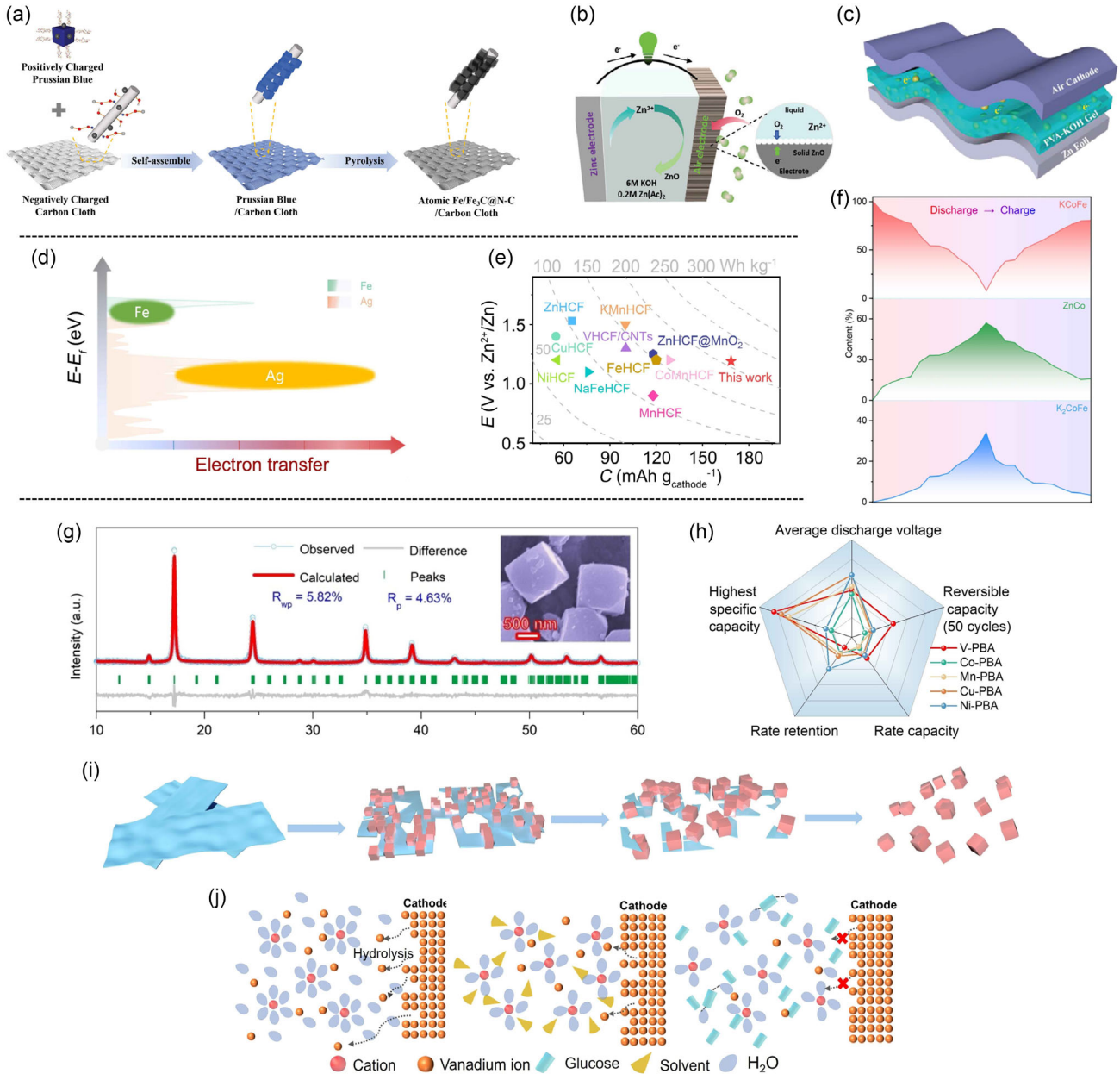

FIGURE 9 | (a) Diagrammatic representation of the catalyst synthesis process. (b) Customized mold schematic diagram. (c) FZABs schematic diagram. Reprinted with permission [148]. Copyright 2024, The Author(s). (d) redox potentials of the elements Ag and Fe in AgHCF-3. (e) ragone plot showing the energy density average voltage and capacity of our work with various PBA materials. Reprinted with permission [149]. Copyright 2024, Wiley-VCH GmbH. (f) Changes of phases content for KCoFe, ZnCo and K_2CoFe during charge–discharge process. (g) Rietveld refinement XRD pattern of KCoFe. The insert is the SEM image of KCoFe. Reprinted with permission [150]. Copyright 2024, Wiley-VCH GmbH. (h) Comparison of electrochemical performance between the V-PBA and other metal-based PBA cathodes for AZIBs. (i) Schematic diagram from V_6O_{13} nanobelts to V-PBA nanocubes. (j) Schematic illustration of dissolution behavior of V-PBA cathode. Reprinted with permission [151]. Copyright 2024, Wiley-VCH GmbH.

vacancies and water, was effectively synthesized through the precise adjustment of the K-to-Ag ratio within its crystalline structure (as shown in Figure 9d,e). The Zn//AgHCF-3 battery cell achieves an approximate energy density of 200 Wh kg^{-1}, exceeding that of previously reported PBA-based zinc-ion batteries. Notably, the formation of metallic Ag0 during the cycling process significantly enhances the rate performance of AgHCF-3. It maintains a capacity of 156.4 mAh g^{-1} at a current density of 200 mA g^{-1} after 100 cycles, with a capacity retention rate of 80.3%. This study pioneers novel pathways for the development of high-capacity PBA cathodes, enhancing their superior electrochemical characteristics [149]. Furthermore, PBAs demonstrate remarkable potential as electrode materials due to their versatile electrochemical activity and cost-effectiveness. Nickel-based bimetallic hydroxides are extensively employed as electrode materials for supercapacitors, benefiting from their high theoretical specific capacitance and economic viability [152]. Moreover, manganese-based Prussian blue analog (PW) is characterized by a high voltage platform, high specific capacity, and competitive cost-effectiveness [153].

However, these materials often suffer from severe structural degradation caused by Jahn–Teller distortion and the dissolution of

high-spin transition metal ions, resulting in unsatisfactory cycling stability. While material modification and electrolyte optimization have been extensively employed to address this issue, their efficacy has remained relatively limited. In this study, researchers propose a novel and highly efficient strategy to preserve structural integrity by co-doping Co^{2+} and Zn^{2+} ions into $KCo[Fe(CN)_6]$. This concurrent insertion (Figure 9f,g) enables a spontaneous and reversible phase transformation via the substitution of low-spin inner ions (Fe^{3+}). This mechanism effectively suppresses structural degradation caused by Jahn–Teller distortion and metal-ion dissolution, thus achieving superior Zn^{2+} storage performance and significantly enhancing the cycle life. This study constitutes a significant advancement in addressing the cycling stability of PBAs, thereby facilitating their practical application as electrode materials in aqueous batteries [150]. In addition, vanadium-based PBA nanocubes were successfully synthesized for the first time via a mild in situ transformation method at ambient temperature without requiring noble gas protection (as illustrated in Figure 9h–j). This highlights their exceptional ability to perform at various rates and their durability over extended cycling periods. This research not only provides an innovative strategy for synthesizing pure PBA nanostructures but also highlights a viable pathway to enhance the cycling durability of PBA-based AZIBs [154] under high current densities, thereby facilitating their potential industrial applications [151]. Furthermore, the substitution of aqueous electrolytes with a zinc hydrogel polymer electrolyte (ZHPE) is introduced [155].

6.3 | Others

Over the last 20 years, numerous aqueous rechargeable metal-ion batteries (ARMBs) have been created to enhance safety, environmental friendliness, and economic efficiency, making them suitable for applications in consumer electronics, electric vehicles, and large-scale energy storage systems. Nevertheless, the substantial disparity in energy density between aqueous rechargeable metal batteries (ARMBs) and traditional organic batteries impedes their real-world implementation, posing a major obstacle to substituting the prevalent organic lithium-ion batteries. Essentially, the significant disparity in energy density can be mainly ascribed to cell voltage, since the limited electrochemical stability range of aqueous electrolytes greatly constrains the selection of suitable electrode materials. This review provides an in-depth examination of different ARMBs [156], with an emphasis on their voltage properties and methods that can efficiently improve battery voltage. The study starts by examining the key limitation on the voltage of ARMBs, focusing on the electrochemical stability range of water-based electrolytes. This range determines the maximum voltage difference that can be maintained between the cathode and anode. The subsequent chapter explores a range of ARMB systems, examining their voltage features through midpoint and plateau voltages, and linking these aspects to the attributes of particular electrode materials. Subsequently, the review outlines several strategies that promote the development of high-voltage ARMBs, emphasizing recent breakthroughs. Finally, the conclusion highlights potential directions for further improvement and provides insights into the future outlook of this rapidly advancing field [157]. Moreover, PBAs are generally regarded as materials capable of reversibly incorporating divalent cations, such as calcium (Ca^{2+}) and magnesium (Mg^{2+}). However, the presumed reversible insertion of Mg^{2+} into nanoscale PBA materials has been shown to be a misconception. There is substantial evidence suggesting that this process is unfeasible, regardless of whether the material is rich or poor in cations, within nickel, iron, and copper hexacyanoferrates. By analyzing structural, electrochemical, IR spectroscopy, and quartz crystal microbalance data, we determine that the charge compensation in PBA redox reactions stems from protons instead of divalent ions within aqueous Mg^{2+} solutions. The reversible addition of protons involves intricate reorganizations of the lattice water molecules. At the same time, the existence of Mg^{2+} ions and anions from Mg salts helps to stabilize the processes of proton insertion and deinsertion. This stabilization is achieved by modulating the local pH and through the adsorption of anions onto the PBA surface. These results highlight the importance of developing proton-based batteries that function in eco-friendly aqueous solutions with minimal acidity [158]. Furthermore, PBAs exhibit significant potential as cathode materials for PIBs, attributed to their large interstitial spaces that can efficiently accommodate the relatively bulky K^+ ions. Manganese-based PBA (MnHCF) shows a high redox potential; however, it experiences substantial capacity fading over extended cycling. Conversely, iron-based PBA (FeHCF) demonstrates exceptional cycling stability but features a relatively lower redox potential. This divergence in electrochemical performance is primarily ascribed to differences in coordination states. By integrating these two coordination states into a single framework, an iron/manganese coexisting PBA (FeMnHCF) is synthesized. This substance not only attains a high average discharge voltage of 3.82 V versus K^+/K but also demonstrates excellent cycling stability, with a capacity of 90 mAh g^{-1} remaining after 600 cycles in a typical ester-based electrolyte. The results indicate that the coexisting coordinated structure not only increases the redox potential of N-coordinated Fe but also markedly improves the capacity at high voltages (over 3.5 V). Moreover, this structure successfully inhibits the dissolution of transition metal (TM) elements and preserves structural stability throughout the K^+ intercalation/deintercalation process, a critical factor in ensuring exceptional cycling performance. This research offers a potential approach for developing stable, high-voltage PBA cathode materials [159]. Furthermore, PBAs are considered potential candidates for aqueous [160] zinc-ion batteries due to their distinctive open-framework structures. Nevertheless, they encounter issues like restricted capacity and substantial capacity loss, primarily due to a lack of sufficient redox-active sites and instability in their architecture. This study introduces copper-substituted manganese Prussian blue analogs double-shelled nanoboxes (CuMn-PBA DSNBs). These structures are synthesized using tannic acid etching and cation exchange methods, exhibiting remarkable efficiency in zinc ion storage capacity. Their unique hollow architectures not only reveal a significant number of active sites but also mitigate volume fluctuations during cycling, which in turn boosts electrochemical performance. And that, a hierarchical porous carbon material (CNC800) was developed via high-temperature pyrolysis of ZIF-67@ZIF-8 core–shell structures [161]. Moreover, replacing a portion of Cu and creating Mn vacancies could significantly reduce the Jahn–Teller distortions within the Mn-N6 octahedra. This factor is essential in improving the durability of the material. Consequently, CuMn-PBA DSNBs demonstrate excellent reversible capacity, remarkable rate performance, and extraordinary

cycling stability for more than 2000 cycles. Furthermore, ex situ analyses indicate that the charge storage mechanism of CuMn-PBA DSNBs primarily consists of reversible redox reactions of transition metals, which are associated with the intercalation and deintercalation processes of Zn^{2+} ions [162, 163]. Less than that, PBAs are viewed as promising and reliable cathode materials for AZIBs. Nevertheless, they face issues like restricted capacity and inadequate cycling stability, primarily due to the lack of active sites and structural deterioration during ion insertion/extraction processes. To overcome these limitations, a template-directed ion exchange approach has been developed for synthesizing cobalt-incorporated, manganese-rich PBA hollow spheres as cathode materials for aqueous AZIBs [164]. By utilizing advantageous features like a hollow structure, multiple active sites, rapid Zn^{2+} diffusion kinetics, and partial integration of cobalt, the CoMn-PBA HSs electrode exhibits exceptional zinc ion storage performance. This is characterized by significant capacity, remarkable rate capability, and prolonged cycling stability [165]. Furthermore, the plentiful reserves and economic viability of potassium resources have positioned KIBs as a potential substitute for lithium-ion batteries. Nevertheless, the greater ionic size of potassium ions poses significant difficulties in developing appropriate electrode materials. PBAs with Ni substitution have been widely studied as cathode materials for KIBs. The synthesized compound $K_{1.90}Ni_{0.5}Fe_{0.5}[Fe(CN)_6]_{0.89}{\cdot}0{\cdot}42H_2O$ (KNFHCF-1/2) integrates several advantages: high capacity stemming from the electrochemical activity of Fe-ions, superior electrochemical performance attributed to a reduced band gap and activation energy for K-ion diffusion, and remarkable structural stability ensured by nonreactive Ni-ions. Thus, KNFHCF-1/2 demonstrates a large capacity of 81.6 mAh g^{-1} at a current density of 10 mA g^{-1}, an exceptional rate capability. The addition and removal of K^+ occur through an effective solid solution reaction mechanism, facilitating a 1.5-electron transfer via low- and high-spin Fe^{2+}/Fe^{3+} redox pairs. Additionally, a full K-ion battery using a graphite counter electrode demonstrates an impressive energy density reaches 282.7 Wh kg^{-1}. This research could stimulate further exploration of PBA materials for electrode applications and drive progress in potassium-ion battery technology [166]. Furthermore, a novel hybrid battery technology featuring an Mg anode and an Fe-based PBA cathode (as shown in Figure 10a) is introduced. This cathode is doped with functional transition metal ions and contains N═O bonds, which enhance its electrochemical performance [167]. Furthermore, researchers suggest an entropy-driven approach to realize ultralong lifespan aqueous AIBs (as illustrated in Figure 10b) through the use of ME-PBAs as the host material [168]. Furthermore, in contrast to the current predominant focus on cations, we emphasize the underexplored competition between anions and cations (C^-, K^+, Zn^{2+}) (Figure 10c,d), which is triggered by high-voltage scanning [169].

Moreover, scientists employed OR during the electrochemical cycling of a copper hexacyanoferrate electrode in proton batteries (Figure 10e,f). In this process, the dissolved Cu and Fe ions experience a crystallization process, resulting in the creation of a stable interfacial layer composed of interconnected cubic structures on the electrode surface [170]. In addition, a zinc-nitrate ($Zn\text{-}NO_3^-$) battery system was developed to simultaneously achieve ammonia (NH_3) synthesis via the electrocatalytic nitrate reduction reaction (NO_3RR) (as illustrated in Figure 10g,h) while also producing electricity [171].

7 | Electrocatalytic Applications of Prussian Blue and its Analogs

7.1 | OER

Co-PBA was successfully synthesized via low-temperature air plasma assistance, and it was found that Co-PBA exhibited remarkable catalytic performance for the OER. The TiO_2/PBA composites demonstrated superior photoelectrochemical performance compared with TiO_2 alone, as PBA acted as a highly effective co-catalyst which facilitated the transfer, separation, and transport of photogenerated electron–hole pairs while simultaneously enhancing visible light absorption. Taking into account various factors such as the highest photocurrent density at 1.7 VRHE, the most significant reduction in overpotential, the most negative flat-band potential, the smallest bandgap, excellent stability, relatively low charge transfer resistance, rapid photocurrent response, and prolonged electron lifetime, it can be concluded that TiO_2/PBA (5:1) possesses the strongest photoelectrocatalytic activity for water splitting [172]. If the number of inert sites is high, they significantly affect the electrocatalytic activity and practical application of PBA. One of the key challenges is to activate the inactive sites in PBA to achieve efficient OER. Fe sites modified by incorporating Mo and S into inert PBA were successfully designed and synthesized via a hydrothermal method, aiming to enhance structural stability and boost OER performance. The PBA-SMo/NF exhibits enhanced activity with a reduced overpotential and shows remarkable durability at high current densities. Theoretical studies on H_2O adsorption energy and Bader charges suggest that the Mo sites in PBA-SMo promote improved H_2O adsorption dynamics. More importantly, examining the Gibbs free energy plot and density of states indicates that PBA-SMo has lower energy hurdles for the OER along with improved conductive properties. This study offers valuable perspectives for the development and improvement of PBA materials across various applications [173]. Furthermore, to efficiently convert renewable energy through water splitting, it is essential to design high-performance electrocatalysts for the OER. The PBA@POM material was synthesized using a PBA as the starting framework. A simple hydrothermal approach was utilized to synthesize PBA@POM. This process included etching cubic PBA frameworks using a strong Brønsted acid, $H_3PMo_{12}O_40$ (HPMo). The resulting hollow cube configuration not only increases the accessibility of active sites but also promotes electron transfer, leading to enhanced electrocatalytic efficiency for the OER. Unlike the initial PBA that merely anchors on POM, the optimized PBA@POM hybrids display markedly enhanced OER catalytic efficiency. The facilely synthesized PBA@POM, with its outstanding electrochemical activity and stability, holds great potential for practical application in the OER process [174]. Moreover, scientists have successfully incorporated Co–O–Fe catalytic active motifs into cobalt-iron Prussian blue analogs (CoFe–PBA) (Figure 11a–c) through the application of oxygen plasma treatment. This approach not only effectively activates lattice oxygen, thereby improving its reactivity, but also ensures the preservation of superior structural stability [175]. In addition, the researcher demonstrates that K^+ ions in the interstitial regions of CoFe PBA can be effectively replaced by NH_4^+ ions via treatment with a hot aqueous urea solution. This substitution process plays a critical role in influencing the structural transformation of PBAs during subsequent heat treatment (Figure 11d,e)

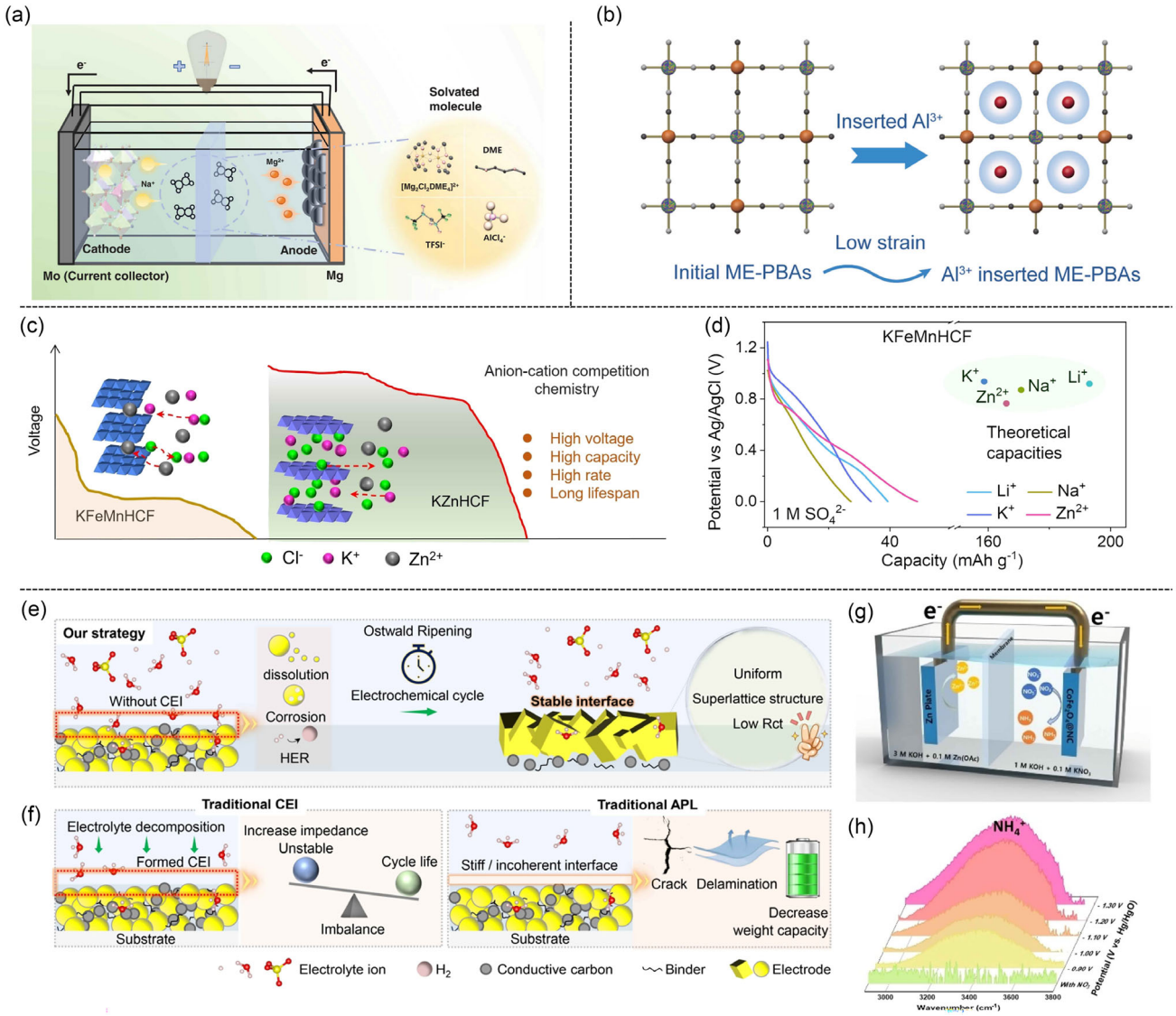

FIGURE 10 | (a) The conceptual illustration of Mg-Na hybrid batteries utilizing ZMNO-PBA cathode and high-voltage dual-salts electrolyte. Reprinted with permission [167]. Copyright 2024, The Author(s). (b) Illustration of the Al^{3+} insertion/extraction mechanism within the ME-PBA and Mn-PBA frameworks during the electrochemical reaction. Reprinted with permission [168]. Copyright 2024, Wiley-VCH GmbH. (c) Demonstration of the anion-cation competitive chemistry, which results in an elevated discharge voltage plateau, enhanced capacity, improved rate capability, and superior cycling stability. (d) Electrochemical characteristics of the KFeMnHCF electrode in a three-electrode configuration. Reprinted with permission [169]. Copyright 2024, Wiley-VCH GmbH. Structural characterization of CuHCF. (e) Schematic of OR process. (f) Schematic of traditional CEI and APL. Reprinted with permission [170]. Copyright 2024, Wiley-VCH GmbH. (g) Graphical representation of the fabricated Zn-NO_3^- battery using a $CoFe_2O_4$@NC cathode. (h) Potential-resolved ex situ ATR-FTIR spectra. Reprinted with permission [171]. Copyright 2024, Wiley-VCH GmbH.

and consequently affects the OER performance of the resulting derivatives [176]. Furthermore, the researchers propose a ligand-mediated MOF-on-MOF strategy for constructing diverse trimetallic MnFeCo-based PBA nanostructures, as illustrated in Figure 11f,g [177].

7.2 | HER

The researchers introduce a method involving ammonia-assisted in situ cation exchange for synthesizing dodecagonal N-doped carbon-based nanosheets containing Pd, Co, and Ni (Pd-e-NiCo-PBA-C) and systematically evaluate their catalytic performance. The Pd-e-NiCo-PBA-C demonstrates remarkably low overpotentials and Tafel slopes for both the HER and OER in both acidic and alkaline environments. Specifically, it attains overpotentials of only 47 mV (pH = 0, HER), 147 mV (pH = 14, HER), and 309 mV (pH = 14, OER). These values surpass the performance of commercially available IrO_2-based and Pt-based catalysts. Moreover, after 5000 cycles, the linear sweep voltammetry curve demonstrates a minimal deviation, underscoring its remarkable stability. To assess its overall water-splitting efficiency, Pd-e-NiCo-PBA-C is utilized as the material for both the cathode and anode. A notable current density of 33 mA cm^{-2} is attained at a cell voltage of 1.6 V, with the catalytic activity preserving 97.3% of its original value after over 50 h of

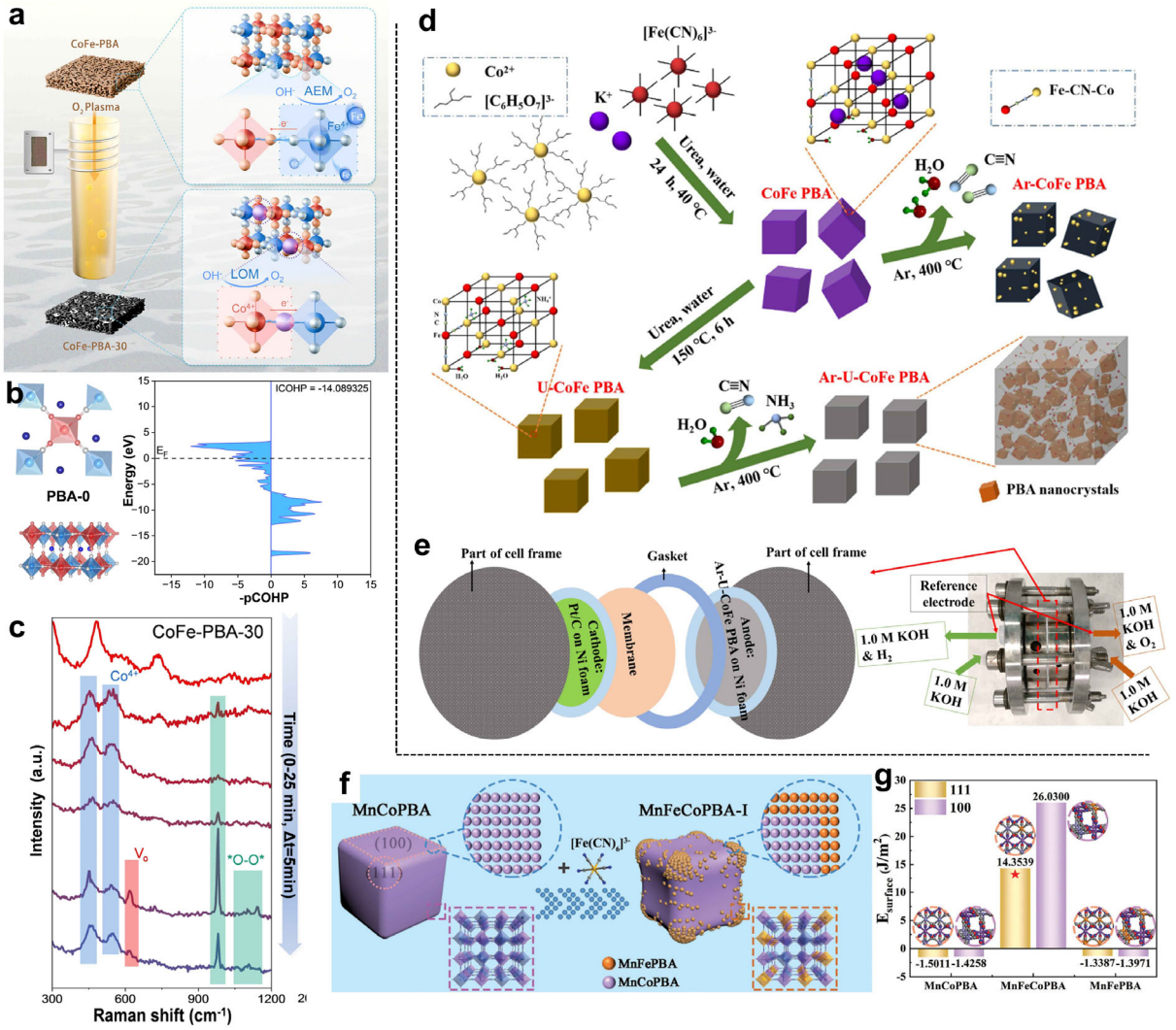

FIGURE 11 | (a) Schematic representation of the local structural changes and the suggested OER mechanism for PBA-30 during the reaction. (b) Snapshot of Co-NC-Fe configuration and crystal orbital Hamilton population (COHP) analysis in PBA-0. (c) Operando Raman spectra of PBA-30 in 1.0 M KOH. Reprinted with permission [175]. Copyright 2024, Wiley-VCH GmbH. (d) Synthesis process. Diagrammatic representation of the synthesis method for CoFe PBA, U-CoFe PBA, Ar-CoFe PBA, and Ar-U-CoFe PBA. (e) Illustration and digital image of the alkaline electrolyzer utilized for the two-electrode testing. Reprinted with permission [176]. Copyright 2022, Science Press and Dalian Institute of Chemical Physics. (f) Formation of schematic trimetallic PBA heterostructures. (g) Surface energies associated with the (111)/(100) faces of MnCoPBA, MnFePBA, and MnFeCoPBA. Reprinted with permission [177]. Copyright 2024, The Authors.

continuous operation. To achieve a more comprehensive understanding of the outstanding OER and HER performance, theoretical investigations are carried out. The improved performance can be ascribed to the unique attractions between Pd and Ni atoms and gas molecules. Moreover, replacing inert atoms can not only decrease binding energy but also greatly improve electrocatalytic activity [178]. To date, PBA materials have been widely studied as potential electrocatalysts for the HER. However, their practical application remains limited by challenges such as low electrical conductivity and obscured active sites, which result in significantly higher overpotentials compared to thermodynamic requirements. Recently, researchers have developed an innovative strategy by introducing unconventional dual vacancies—comprising cyano-group anion and cobalt cation—in CoFe-PBA by means of a fast TA etching procedure. Extensive experimental and theoretical studies suggest that introducing these bivacancies not only increases the exposure of available active sites but also improves the distribution of electron density in CoFe-PBA, thus significantly lowering the reaction energy barrier. Consequently, the tannic acid-etched CoFe-PBA nanocubes attached to nickel foam (NF), referred to as CoFe-PBA@TA/NF, demonstrate exceptional catalytic performance for the HER. Specifically, these materials demonstrate a remarkably low overpotential of 86 mV at a current density of 10 mA cm^{-2}. This value shows a substantial decrease when compared to the bare PBA supported on NF, which is measured at 158 mV. Additionally, their performance aligns closely in comparison to commercial Pt/C catalysts [179]. Moreover, developing a stable heterojunction structure and investigating the interfacial charge transfer process at the atomic scale are crucial approaches to reduce photocorrosion and inhibit electron–hole recombination in CdS-based photocatalytic hydrogen generation.

A temperature-guided self-assembly technique has been devised to create PBA/CdS nanocomposites exhibiting a unique beaded morphology. Uniquely engineered architecture featured uniformly exposed CdS nanoparticles, which effectively captured visible light while suppressing photocorrosion. Simultaneously, the PBA with an extensive cavity facilitated mass transfer pathways and established active centers for photocatalytic reactions. This research offers deep insights into the strategic design of heterostructured materials for improved photohydrogen evolution (PHE) applications [180]. The development of efficient electrocatalysts for hydrogen production is crucial for the practical deployment of water-splitting technologies. Transition metal sulfides, which exhibit multiple electrochemical advantages, are regarded as promising candidates for promoting the HER in acidic media. In this study, Ru-doped cobalt sulfide nanosheets (denoted as Co_9S_8/Ru@t, where $t = 24$, 48, and 72 h) were synthesized. The reaction duration is crucial to increase the density of electroactive sites and optimizing the hydrogen adsorption–desorption processes, thereby significantly enhancing the HER performance of Co_9S_8/Ru@48h. The electrochemical results demonstrate that the optimized Co_9S_8/Ru@48h catalyst achieves a current density of 10 mA cm^{-2} at a minimal overpotential of only 94 mV, accompanied by a reduced Tafel slope of 84 mV dec^{-1}, indicative of its rapid reaction kinetics. Furthermore, the synthesized Co_9S_8/Ru@48h catalyst exhibits excellent stability, maintaining consistent performance during continuous electrolysis for up to 20 h. These findings, combined with its advanced synthesis method and superior electrochemical properties, establish Co_9S_8/Ru@48h as a potential substitute for noble-metal-based electrocatalysts for HER applications [181].

7.3 | ORR

Owing to the complexity of the ORR, developing catalysts with multiple catalytic centers is considered a promising strategy for enhancing ORR performance. Herein, we successfully fabricated a multi-center electrocatalyst consisting of Fe_3C/Mn_3O_4 encapsulated within N-doped graphitic layers (FeMn PDA-900) using iron manganese polyoxometalates and dopamine as precursors. Furthermore, the catalyst developed through this synthesis method demonstrates exceptional The ORR activity for both acidic and neutral electrolyte environments. This underscores its promising applicability in proton exchange membrane fuel cells as well as microbial electrolysis cells. It has been demonstrated that the exceptional results can be attributed to primarily attributed to the proton-coupled electron transfer (PCET) mechanism. This is enabled by multiple catalytic centers derived from Fe-N_x, Fe_3C, and Mn_3O_4, which provide abundant active sites simultaneously. Moreover, the N-doped graphitic layers serve as a conductive route that enables effective electron transfer across the interfaces of Fe_3C/Mn_3O_4 nanoparticles. Such a design enables the concurrent and rapid transfer of protons and electrons, thereby reducing the energy barrier and enhancing ORR process. FeMn PDA-900 emerges as an exceptionally promising substitute for precious metal-based ORR electrocatalysts across the entire pH spectrum [182]. Less than that, electrochemical approaches hold great promise as technological routes for future clean energy storage and conversion. A significant number of these techniques emphasize reactions associated with oxygen. The primary obstacles in these processes include poor kinetics and sluggish reaction rates. This research presents a simple method for creating highly effective catalysts for both OER and ORR. The catalysts are synthesized by incorporating metal ions into PBAs, resulting in the creation of materials known as M-PBAs. Among the catalysts studied, CoNi-PBA-2 exhibits the most superior OER performance, featuring an onset potential of 280 mV and a Tafel slope of 63 mV dec^{-1}. Meanwhile, Zn-PBA catalysts demonstrate exceptional selectivity for the two-electron ORR, with an H_2O_2 yield reaching up to 88% at 0 V relative to the RHE. Furthermore, DFT calculations confirm the outstanding selectivity of Zn-PBA for H_2O_2 production during the ORR [183].

7.4 | Carbon Dioxide Conversion

The increase in atmospheric carbon dioxide (CO_2) levels has contributed to the global warming and its association with extreme weather phenomena. Utilizing solar energy to photocatalytically transform CO_2 into valuable chemicals represents a promising strategy to address this challenge. MOFs, which belong to a category of organic–inorganic hybrid materials, exhibit substantial potential for photocatalytic CO_2RR. Nevertheless, many MOFs employed in CO_2RR suffer from limited photocatalytic efficiency and selectivity due to the presence of only a single active metal site, and they also face challenges related to instability under reaction conditions. In this context, ten PBAs were directly utilized as heterogeneous catalysts for photocatalytic CO_2RR, achieving remarkable performance in producing carbon monoxide (CO). Using Ni−Co PBA catalysts, a mass evolution rate of 140 mmol g^{-1} h^{-1} was attained, along with an apparent quantum efficiency (AQY) of roughly 0.7% and a selectivity for CO of almost 96.8%. Notably, CO_2RR activities of MIICo PBAs surpass those of MII−Fe PBAs. However, MII−Fe PBAs exhibit higher selectivity for CO compared to MIICo PBAs. This variation in activity can be ascribed to their differing electron transfer rates, which have been verified through electrochemical tests and spectroscopic investigations. Additionally, DFT calculations, combined with studies on the adsorption and desorption of H_2 in PBAs, provide insights into the mechanisms underlying the differences in selectivity [184]. Furthermore, the integration of chemical looping CO_2 capture combined with in-situ reverse water gas shift represents a promising approach for simultaneously achieving CO_2 capture and its conversion, thereby effectively addressing CO_2 emission challenges. Unlike most bifunctional materials that function within a sorbent-catalyst reaction framework, transforming the reaction structure into a sorbent-oxygen carrier configuration by incorporating a redox pair can enable an innovative CL-ICCC-RWGS strategy. A new combined method for CO_2 capture and transformation has been designed and confirmed through experimentation. This was achieved by synthesizing a range of PB-based Ca-Fe bifunctional materials with different iron content and then examining their cyclic capture-conversion reactivity. These dual-functional materials, containing both Ca and Fe elements, exhibit CO production during isothermal cycles. This occurs as a result of the re-oxidation of metallic iron with CO_2 in the capture half-cycle and the reverse water-gas shift reaction during the transformation half-cycle [185].

7.5 | Others

Cyanide-based coordination polymers, such as PBAs, are prominent materials in electrocatalysis. These compounds exhibit open-framework architectures, high particular surface regions, tunable metal active locations and consistent catalytic hubs, rendering them highly suitable for electrocatalytic water splitting. Furthermore, the distinct structural characteristics of PBAs allow their derived electrocatalysts to exhibit extensive surface areas and effectively distributed active sites. Additionally, PBAs can function as precursors for incorporating carbon and nitrogen. The addition of nitrogen can adjust the electronic properties regarding the active sites on the surface, thus boosting the inherent activity of the electrocatalysts. As a result, electrocatalysts derived from PBAs demonstrate exceptional efficiency in water splitting reactions. Moreover, the targeted method of removing ions from water through CDI plays a vital role in numerous environmental and industrial contexts, including water treatment, softening processes, and resource retrieval. Given their unique size and structural characteristics, PBAs have been considered as possible materials for electrodes in selective extraction of cations from water. To date, PBAs used in CDI systems have predominantly demonstrated selectivity toward monovalent ions. VHCF, A type of PBA is employed as an innovative electrode material in a hybrid CDI setup for the selective removal of divalent cations from water. The preference for divalent cations by these electrodes can be elucidated through DFT simulations. Moreover, applying a conductive polymer coating to the VHCF electrodes effectively mitigates water contamination caused by electrode degradation. This straightforward and adaptable coating technique can be easily applied to other PBA electrodes, thereby reducing water contamination during repeated operational cycles. This research not only introduces new possibilities for adjustable ion selectivity but also broadens the scope for electrodes that are suitable for use in selective CDI processes [186]. Moreover, a self-sustaining electrochromic device has been developed through a compact design by integrating a Zn/MnO_2 ionic battery (as shown in Figure 12a–c) into an electrochromic system based on PB [187].

In addition, researchers have identified that the predominant cause of PBAs dissolution is the elevated local pH of the electrolytes (Figure 12d,e), which results from proton co-insertion during the discharge process [188]. Furthermore, scientists have introduced a novel supramolecular assembly coating method to develop a sequence of binary electrocatalysts. This is achieved through the application of eight PBA profile coatings onto supramolecular supports (as shown in Figure 12f), serving as bimetallic precursors [189]. Moreover, scientists integrate ligand-coordinated ions into MPS_3-based (M = Mn, Cd) solid host crystals, thereby enlarging the interlayer spacing (Figure 12g,h) to facilitate ion migration while simultaneously shielding the charge-dense ions [190]. Furthermore, vanadium hexacyanoferrate PBA (VOHCF) is considered a potential cathode material for APBs because of its distinctive structural and electrochemical characteristics [191]. Furthermore, scientists have fabricated Ni-Fe Prussian blue analog nanocubes (NiFe-PBA-NC) using a straightforward precipitation technique. These nanocubes were subsequently transformed into NiFe-PBA-NG and porous mixed-metal oxides [192]. Moreover, FeCo alloy nanoparticles are fabricated on a carbon cloth substrate through a low-temperature heating approach, utilizing FeCo Prussian blue analog as the precursor material [193]. Furthermore, scientists have developed an easy approach for creating CoP nanoparticles with high dispersion, obtained from cobalt-based PBAs, which are centered on N-doped electrospun porous carbon material nanofibers (referred to as CoP@CNF) [194]. Furthermore, nitrogen-doped carbon (NC) encapsulated NiFe-NiFeP nanocubes, which are anchored on carbon nanotubes (CNT), denoted as NiFe-NiFeP@NC/CNT, are prepared by utilizing NiFe-PBA nanocubes and CNT composites as precursors. This is followed by polydopamine (PDA) coating, carbonization, and partial phosphorization steps [195]. Furthermore, nickel hexacyanoferrate (NiHCF) nanoparticles (NPs) and their derivatives can be prepared through a straightforward co-precipitation technique and subsequently thermally treated in nitrogen and air environments [196].

The notable advantage of DFT lies in its utilization of electron-density approximations for energy calculations, offering a favorable compromise between precision and computational feasibility that is ideal for simulations at Nanometer and ångström resolutions. In Nano Lett. 2025, 25, 957−965 [197], the in-situ synthesis of Prussian blue, mediated by carboxymethyl cellulose—a binder with appropriate binding energy per DFT calculations—successfully regulates the Fe^{3+}/water equilibrium and generates Fe^{III} vacancies in FeHCF, leading to the activation of low-spin Fe sites. Electrochemical tests reveal an initial capacity of 154.7 mAh g^{-1} (470.8 Wh kg^{-1}) at 1C and outstanding cyclability with 70.2% retention over 4000 cycles at 100 C. This methodology establishes a simpler alternative for fabricating cost-effective, high-rate, and highly durable sodium-ion cathode materials.

Its utility extends to both the *a priori* prediction of catalytic activity for unsynthesized candidates and the elucidation of performance origins. This capability for prediction is vital for linking experiment with theory, thus accelerating the development of superior catalytic materials [198]. The acceleration of innovative catalyst development is achieved through the application of DFT simulations, leading to enhanced time and cost efficiency. The predictive power and operational efficacy of these simulations are being steadily improved by the adoption of increasingly complex models and the integration of machine learning techniques. In scenarios where dynamic phenomena are critical, molecular dynamics (MD) offers the capability to model temporal atomic motions, yet its application is often constrained by a lack of electronic-level precision. The integration of DFT principles into ab initio molecular dynamics (AIMD) provides a pathway to greater accuracy in modeling dynamic processes, albeit at a substantially increased computational cost. While such multiscale techniques are indispensable for obtaining profound mechanistic insights, Density Functional Theory retains its preeminence as the foundational pillar in electrocatalysis research. This status is owed to its provision of an optimal equilibrium between efficiency and reliability for investigating a wide range of catalytic environments [199].

8 | Other Applications of Prussian Blue and its Analogues

8.1 | Sensor

The integration of two-dimensional (2D) MOFs with PBAs combines the advantageous characteristics of 2D materials, MOFs,

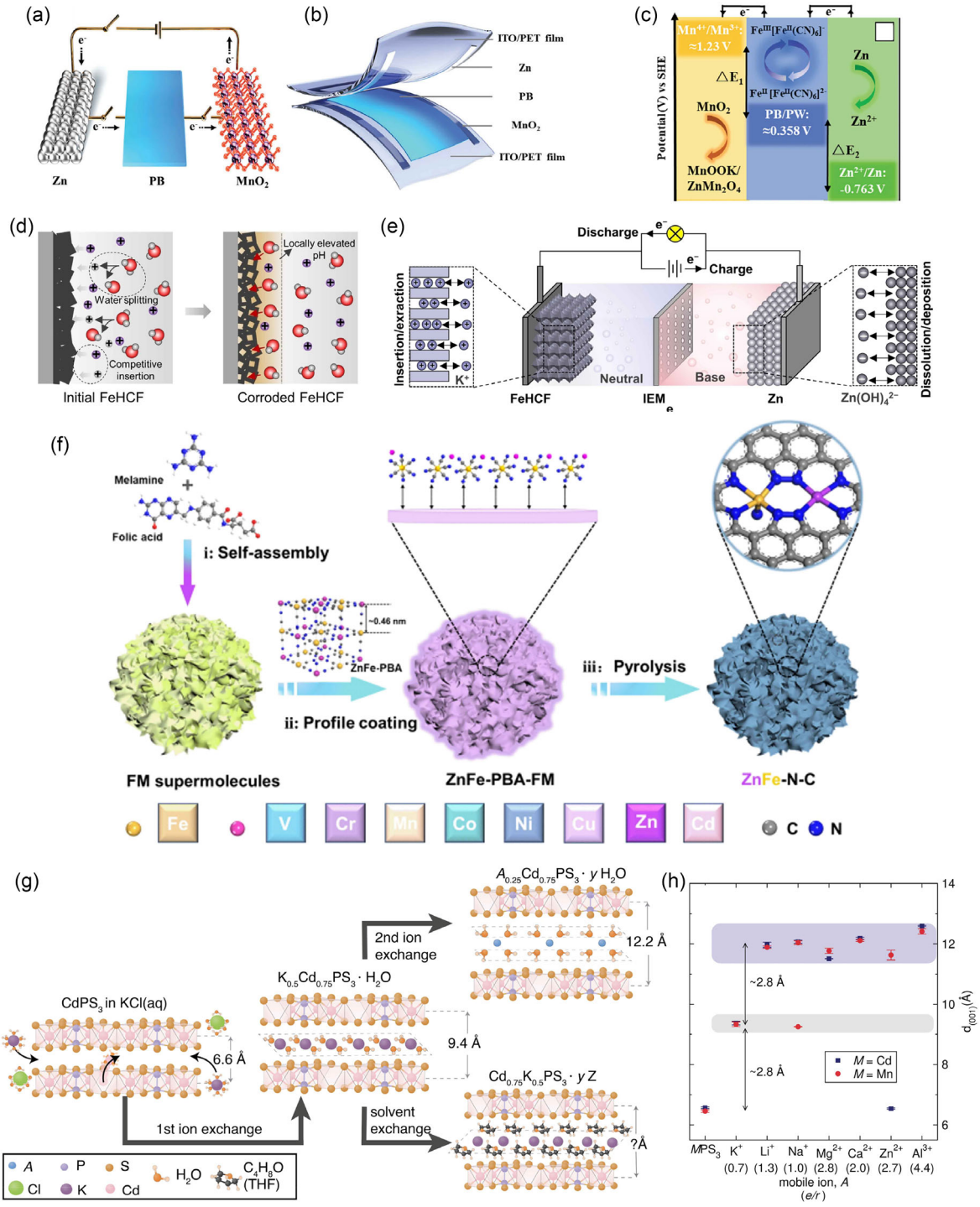

FIGURE 12 | (a) In the Zn||PB||MnO_2 electrochromic system, the Zn electrode can reduce the PB electrode to a transparent PW state when the two electrodes are connected. Additionally, the MnO_2 electrode can quickly oxidize the PW electrode, transforming it into the colored PB electrode. (b) Illustration of the flexible Zn||PB||MnO_2 electrochromic devices featuring a closed-system architecture. (c) Diagram showing the movement of electrons during the bleaching and coloring process, along with the standard electrode potentials of the Zn, Pb, and MnO_2 electrodes. Reprinted with permission [187]. Copyright 2024, The Author(s). (d) Scheme of the electrochemical dissolution of PBAs. (e) Prototype of the designed pH-decoupled cell. Reprinted with permission [188]. Copyright 2024, Wiley-VCH GmbH. (f) Schematic illustration for the synthesis of carbon-based electrocatalysts with dual metal sites. Reprinted with permission [189]. Copyright 2023, Wiley-VCH GmbH. (g) Diagram of the ion and ligand exchange utilized in this study. (h) d(001) spacing of $A_{2x/n}M_{1-x}PS_3{\cdot}yH_2O$. Reprinted with permission [190]. Copyright 2024, The Authors.

and PBAs. This approach successfully addresses the drawbacks of low electronic conduction and gradual diffusion kinetics commonly found in MOF-based electrochemical systems. Through the use of 2D leaf-like Co-ZIF and Fe-ZIF as sacrificial templates, the structures are converted in situ into PBA derivatives, resulting in the formation of robust PBA/ZIF nanocomposites anchored on NF. This innovative approach significantly reduces charge transfer resistance and enhances the efficiency of electron

and mass transport, leveraging the synergistic effect between electrochemically active PBA nanoparticles and the conductive NF substrate. The electrodes, artificially developed to serve as multifunctional sensors, exhibit exceptional selectivity and sensitivity for use in glucose and H_2O_2 biosensing applications. These sensors are characterized by an extensive linear detection range, an exceptionally low detection limit (LOD), and robust stability. Moreover, this the electrode has the ability to accurately monitoring glucose concentrations within human serum, thereby underscoring its potential for real-world uses. Furthermore, this substance functions as a highly effective multifunctional electrochemical sensor, exhibiting exceptional capabilities in detecting hydrogen peroxide. The sensor demonstrates a wide linear detection range, spanning from 0.2 to 6.0 mM. It shows a sensitivity of 196 μA mM^{-1} cm^{-2} and attains an exceptionally low detection limit of 1.08 nM (S/N = 3). The underlying mechanisms contributing to the improved sensing performance for both glucose and hydrogen peroxide are thoroughly explored and validated through extensive experimental data [200]. Furthermore, through the implementation of a dual-signal approach, an electrochemical sensor utilizing a MIP was constructed for the precise and sensitive identification of p-HAP. This sensor was developed by first modifying an electrode with NiFe PBA and then coating it with SnS_2. The dual signals were generated from the redox reactions of $[Fe(CN)_6]^{3-/4-}$ at 0.20 V and NiFe-PBA at 0.52 V. In the electropolymerization process used to create the MIP film, o-phenylenediamine functioned as the functional monomer, and p-HAP was utilized as the template molecule. Upon the attachment of p-HAP and the peak currents of the two aforementioned oxidation processes decreased simultaneously compared to those in the elution phase, enabling reliable dual-signal analysis. When operated under ideal experimental conditions, the sensor demonstrated a wide linear response range extending from 10^{-13} M to 10^{-7} M and attained an exceptionally low detection limit of 3.52×10^{-14} M (3σ). Furthermore, this approach was effectively utilized to measure p-HAP in human serum and environmental water samples, resulting in highly acceptable recovery rates [201]. Less than that, engineering crystal defect sites at the boundary of sensing materials plays a crucial role in improving electrochemical sensing performance.

However, the detailed mechanisms related to the movement of electrons across a surface and the precise atomic-level locations of active sites for analytes remain elusive. In this study, researchers constructed an electrochemical sensing interface with extremely high sensitivity. This sensitivity is fifteen times greater than that of the original Mn-Fe PBA. Moreover, computational results demonstrate a notable interaction between the Mn atom and Pb(II), indicating significant orbital overlap within the Mn–Pb bond. The Pb(II) ions that are adsorbed onto the surface undergo direct redox reactions with the sensing material, occurring independently of the adsorption–desorption kinetics [202]. Furthermore, both PB and PBAs constitute a highly promising class for sensing and biosensing applications, the selection and development of materials are crucial. Their distinctive open-framework architecture facilitates a robust correlation between their electrochemical properties and the intercalation of alkali metal ions. Moreover, these compounds display pronounced peroxidase-like activity, making them exceptionally effective as transducers in biosensors designed for hydrogen peroxide (H_2O_2) quantification. In this work, researchers comprehensively review the structural features, compositional diversity, and synthetic strategies associated with PBAs. Subsequently, they delve into recent advancements in the application of PBAs within electrochemical sensing technologies. This encompasses an in-depth and critical evaluation of their electrochemical behavior, electrocatalytic performance in H_2O_2 electrooxidation and electroreduction processes, as well as their utility in detecting toxic substances, hazardous materials, and pharmaceutical compounds [203]. In addition, a biomimetic receptor for glucose has been effectively developed, exhibiting high affinity and selectivity. This receptor was constructed in three effective stages using dynamic imine chemistry, subsequently undergoing an oxidation process to convert imines into amides. It consists of two parallel durene units that create a hydrophobic cavity capable of participating in [CH···π] interactions. Furthermore, the two pyridinium groups orient four amide bonds toward this cavity. These pyridinium components enhance solubility and provide polarized C—H bonds, which facilitate hydrogen bonding. Both experimental results and DFT computations show that these polarized C—H bonds significantly strengthen the binding of substrates. These findings emphasize the potential of dynamic covalent chemistry for creating molecular receptors and utilizing polarized C—H bonds to improve carbohydrate recognition in aqueous environments. This study establishes a robust groundwork for the advancement of materials and sensors that respond to glucose [204]. Moreover, scientists have created a SERS sensor using self-assembly and mask-supported methods for the accurate transfer of Au@PB@Ag nanoarrays (as shown in Figure 13a,b) onto filter paper [205]. In addition, researchers have developed a recyclable gallium (Ga)-based multilayer electrochemical glucose biosensor for extended noninvasive monitoring of glucose levels (Figure 13c–e) in the interstitial fluid [206]. Moreover, researchers developed a core–shell structured aerogel composed of highly conductive silver nanowires (AgNWs) and exceptionally active PB (Figure 13f,i). This aerogel, with the help of a microfluidic channel, is capable of continuously and precisely monitoring sweat uric acid (UA) [207].

8.2 | Photocatalysis

Engineering heterojunctions to create internal electric fields is a cornerstone strategy for mitigating charge carrier recombination in photocatalysis. Researchers report a rationally designed in-situ transformation strategy where a hybrid of Ni-Co PBA and CdS (CP) evolves into a NiS/CdS (CN) composite during the HER in a sulfur sacrificial reagent. This conversion replaces the original n–n interface between CdS and Ni-Co PBA with a p–n heterojunction between CdS and NiS, leading to superior photocatalytic activity. Crucially, spectroscopic evidence from surface photovoltage and transient absorption measurements indicates that the charge transfer pathway is concurrently reconfigured from a Type-I to a Type-II alignment. The efficacy of this approach is underscored by the CP-2 photocatalyst, which evolves 176.6 μmol of hydrogen—a 13.9-fold enhancement over pristine CdS [208]. Moreover, seeking to design an efficient advanced oxidation process for recalcitrant organic pollutants, we developed a tandem hybrid system that couples photocatalysis with peroxymonosulfate (PMS) activation, drawing inspiration from series hybrid electric vehicles. Herein, Bi_2MoO_6 functions as a photo-powered electron generator. The photogenerated electrons are directionally transferred via the

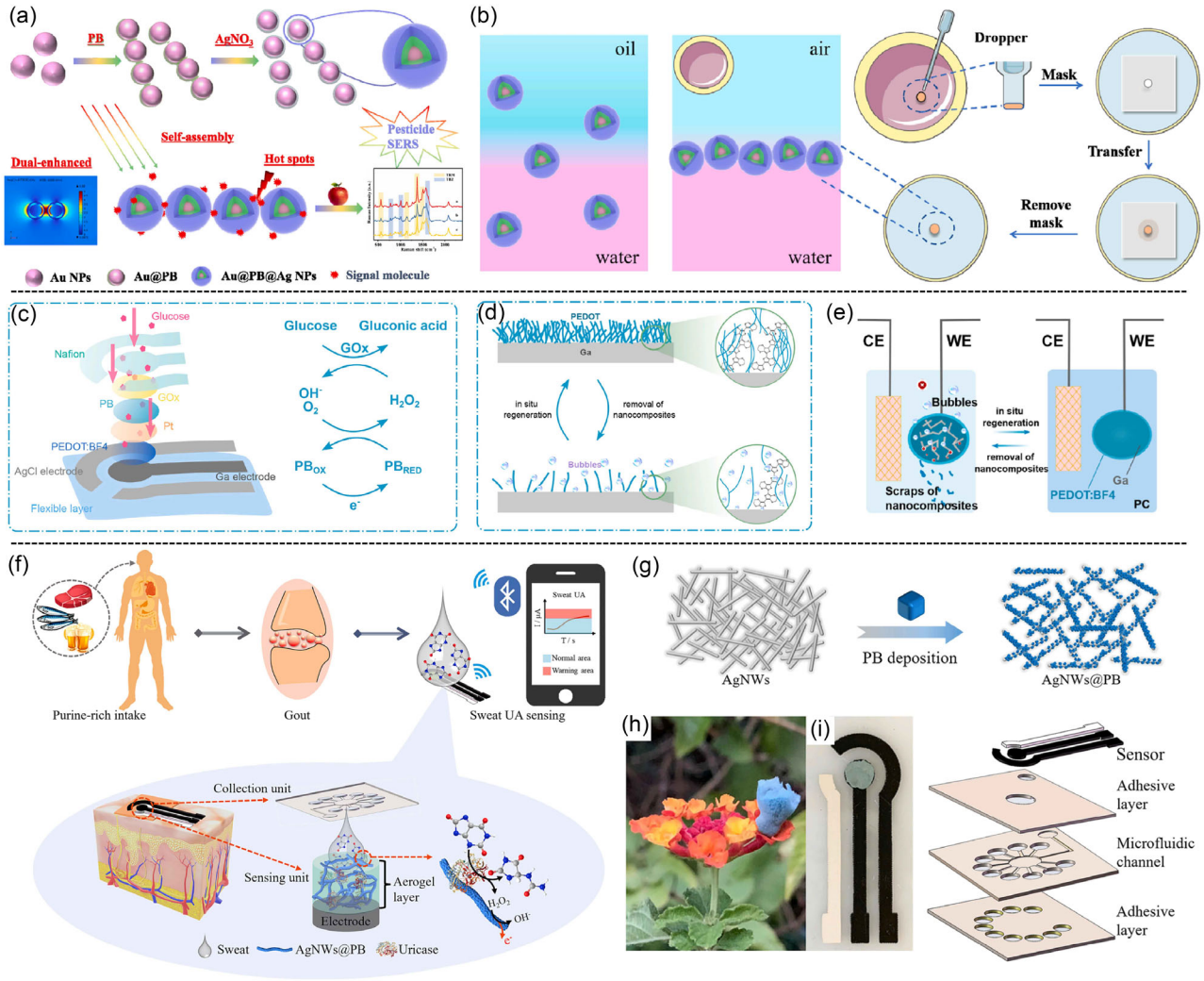

FIGURE 13 | (a) Schematic representation of the synthesis and sensing mechanism for self-assembled Au@PB@Ag nanoarrays. (b) Schematic illustration of liquid–liquid self-assembly, employing a plastic pipette to create uniform monolayers of Au@PB@Ag nanoarrays at specific locations and with precise patterns on filter paper via a masking technique. Reprinted with permission [205]. Copyright 2024, Elsevier B.V. (c) Diagram depicting the disassembled perspective of the Ga-based hybrid sensor and its biological sensing mechanism. (d) A Ga-based hybrid sensor with the ability for in situ regeneration and surface removal is introduced. (e) Illustrative depiction of a Ga-based hybrid sensor that enables the in-situ regeneration process and surface removal. Reprinted with permission [206]. Copyright 2024 Elsevier B.V. (f) Diagram of the wearable sweat sensor designed for UA detection. (g) Diagrammatic representation of the AgNWs@PB composite. Digital images of the AgNWs@PB aerogel positioned on a petal (h) and the AgNWs@PB aerogel-based sensor (i). Reprinted with permission [207]. Copyright 2024, Elsevier B.V.

molecular 'transmission shaft' polyaniline (PANI) to PBAs, empowering it to efficiently and persistently activate PMS. This unique electron delivery mechanism culminates in exceptional catalytic activity, boosting diclofenac (DC) degradation by 55% and elevating the rate constant (k) by a factor of 7 relative to standalone PMS. The system's engineering viability was also preliminarily explored under continuous-flow conditions [209].

Furthermore, PB is a member of the family of metal-organic coordination compounds that display fascinating electrochromic properties. Although its electronic structure has been extensively investigated, the underlying the electrochromic mechanism persists elusive because of limited insights into electronic transitions. To address this, scientists employ a combination of optical characterization techniques and DFT computations to investigate the electrochromism of PB and its derivatives. Through these methods, they accurately determine the optical bandgaps of PB-related derivatives and successfully fabricate a smart window with superior electrochromic performance and temperature regulation capabilities. DFT calculations further demonstrate that the coloring behavior of Prussian yellow (PY) is predominantly governed by two absorption peaks positioned at ≈2.4 and 3.0 eV, respectively. Conversely, the transformation from blue to transparency (referred to as Prussian white) occurs through the reduction of Fe(II) ions, resulting in an increased bandgap that enables visible light transmission. The strength of the band-edge transitions is significantly influenced by the contribution of C-p states, providing potential pathways for optical tuning via anionic doping. These results provide essential perspectives for comprehending and adjusting the optoelectronic characteristics of PB-associated materials for more advanced uses [210]. In addition, photoinduced charge–transfer processes play a pivotal role in both natural phenomena and

technological applications, enabling unique features like magnetic properties ordering in bimetallic coordination networks bridged by cyanide [211]. Although there has been substantial interest and notable progress in chemistry and materials science, providing an atomic-level explanation related to the primary photoinduced process—which connects transitions of intermetallic charge transfer to spin states—has remained a mystery for decades because of its exceptionally fast dynamics. This research enhances our understanding of how light can be harnessed to control charge–transfer-based functionalities [212]. Less than that, PBAs have attracted significant considering materials as a focus for removing radioactive cesium, because of its strong preference for absorbing Cs^+. Scientists have developed a range of PBAs by utilizing Ni^{2+}, Co^{2+}, and Fe^{2+} ions in the synthesis process resulting in the formation of NiFe-PBA, CoFe-PBA, and FeFe-PBA. To modify the particle size and surface area, varying concentrations of sodium citrate were introduced as a stabilizing agent during synthesis. These PBAs were subsequently combined using TiO_2, the effectiveness of Cs^+ adsorption was evaluated under two conditions: in the dark and under UV irradiation. The results indicated that greater surface areas and finer particle dimensions enhanced Cesium (Cs) adsorption performance, particularly for NiFe-PBA and NiFe-TiO_2 composites. Moreover, FeFe-TiO_2 demonstrated exceptional Cs^+ adsorption performance when exposed to UV light. The adsorption capacity of NiFe-PBA enhanced more than two times, increasing from roughly 0.8 mmol g^{-1} in darkness to 1.7 mmol g^{-1} under UV exposure. For NiFe-TiO_2 composite, adsorption capacity roughly triples, increasing from 0.45 mmol g^{-1} in the absence of light to 1.5 mmol g^{-1} when exposed to UV light exposure. Notably, an improved light-induced absorption effect is observed for NiFe PBAs when interacting with radioactive $^{137}Cs^+$. This improvement in Cs^+ adsorption by NiFe PBAs can be ascribed to a light-driven electron transfer reaction that takes place. This research constitutes the initial account of improved light-induced elimination of Cs^+ utilizing PBAs, offering a promising strategy for the effective elimination of radioactive Cs^+ from contaminated water [213]. The creation of sophisticated architectures for semiconductor photocatalysts is acknowledged as a potential approach to improve their effectiveness in transforming solar energy into chemical energy. Structures that are hollow and frame-like possess beneficial characteristics for photocatalytic reactions, including a larger surface area, more efficient charge–transfer routes, enhanced ability to capture light, and superior mass-transfer efficiency. A straightforward two-step sulfidation process has been devised for the synthesis of distinctive CdS particles featuring a frame-in-cage structure, which are used for photocatalytic hydrogen generation. Initially, Cd-PBA are transformed into Cd-PBA cube structures encapsulated within CdS cage particles. Subsequently, these are further converted into particles featuring a CdS frame enclosed within a cage structure. Thanks to the innovative frame-in-cage design, the resulting CdS photocatalyst exhibits exceptional performance under visible-light irradiation, with a hydrogen evolution rate reaching 13.6 mmol h^{-1} g^{-1}. This represents a substantial improvement compared to the activities of conventional CdS cubes and cages [214]. Less than that, if the availability of nanoparticles with programmable interactions and anisotropic bonding characteristics is limited, the capacity to assemble distinct colloidal aggregates (CCs). A technique has been devised by researchers to assemble anisotropic NCs into colloidal crystals, which display open and highly organized architectures. This advancement experimentally realizes the colloidal analogs of zeolitic clathrate structures. These oriented interactions stem from either the crystallographic or morphological anisotropy of the NCs and are realized through the combined effects of epitaxial growth, oriented attachment, and localized arrangement.

The interactions between particles can be ascribed to enthalpic and entropic factors, which simulate the hybridization of atomic orbitals in sp^3d^2 octahedral and sp^3d^3f cubic structures. Due to their highly organized hierarchical porous architectures, the resulting CCs demonstrate markedly improved catalytic efficiency in CO_2 photoreduction. This research provides essential understanding of the directional bonding mechanisms among NCs and pioneers a novel approach for developing distinctive CCs with innovative configurations and promising applications [215]. Furthermore, studies show that the glass transition in cobalt hexacyanoferrate crystals, which belongs to the PBAs, results in a rise in the number of open metals sites and modifies the electronic state. This occurs while preserving the coordination geometries (as shown in Figure 14a,b) and the short-range order within the structure [216]. In addition, to develop an effective advanced oxidation process that overcomes the intrinsic limitations in eliminating recalcitrant organic pollutants, scientists integrate phot catalysis with peroxymonosulfate (PMS) activation. By drawing inspiration from series hybrid electric vehicles, they construct a tandem hybrid catalytic system (as illustrated in Figure 14c–g) [209]. Furthermore, The author presents a novel semiconductor catalyst featuring a core−shell structure (as shown in Figure 14h), designed to significantly enhance the photocatalytic water oxidation performance [217].

8.3 | Biomedical Science

A major challenge associated with current therapeutic agents is their lack of selectivity in drug delivery, as they indiscriminately affect both healthy and cancerous cells. This paper conducts an in-depth analysis of various synthesis methods and surface engineering strategies for the development of PB NPs. Moreover, it elucidates the diverse targeting mechanisms employed to deliver therapeutic and imaging ligands specifically to the tumor site. The review also explores techniques to enhance the tumor-ablative efficacy of the nanoparticles, including several key combinatorial approaches. scholars have comprehensively reviewed the diverse in vitro and in vivo effects of PB nanoparticle (NP)-based therapies aimed at addressing both systemic and localized tumor-associated challenges. A promising emerging strategy—polymer-based nanoparticle immune drug delivery systems—has been investigated, offering a novel and potentially effective solution for overcoming cancer resistance and preventing tumor recurrence. Additionally, the current understanding of the toxicological profiles of PB NPs and their therapeutic applications has been critically analyzed. The authors propose that PB NP-based multimodal imaging-guided chemo-photothermal therapy presents innovative strategies to address existing challenges in cancer diagnosis and treatment [218]. Below that threshold, PB nanoparticles exhibit remarkable physicochemical characteristics. These include capabilities in imaging, effective photothermal conversion, catalytic activities, modifiable surfaces, substantial drug-loading potential, exceptional stability,

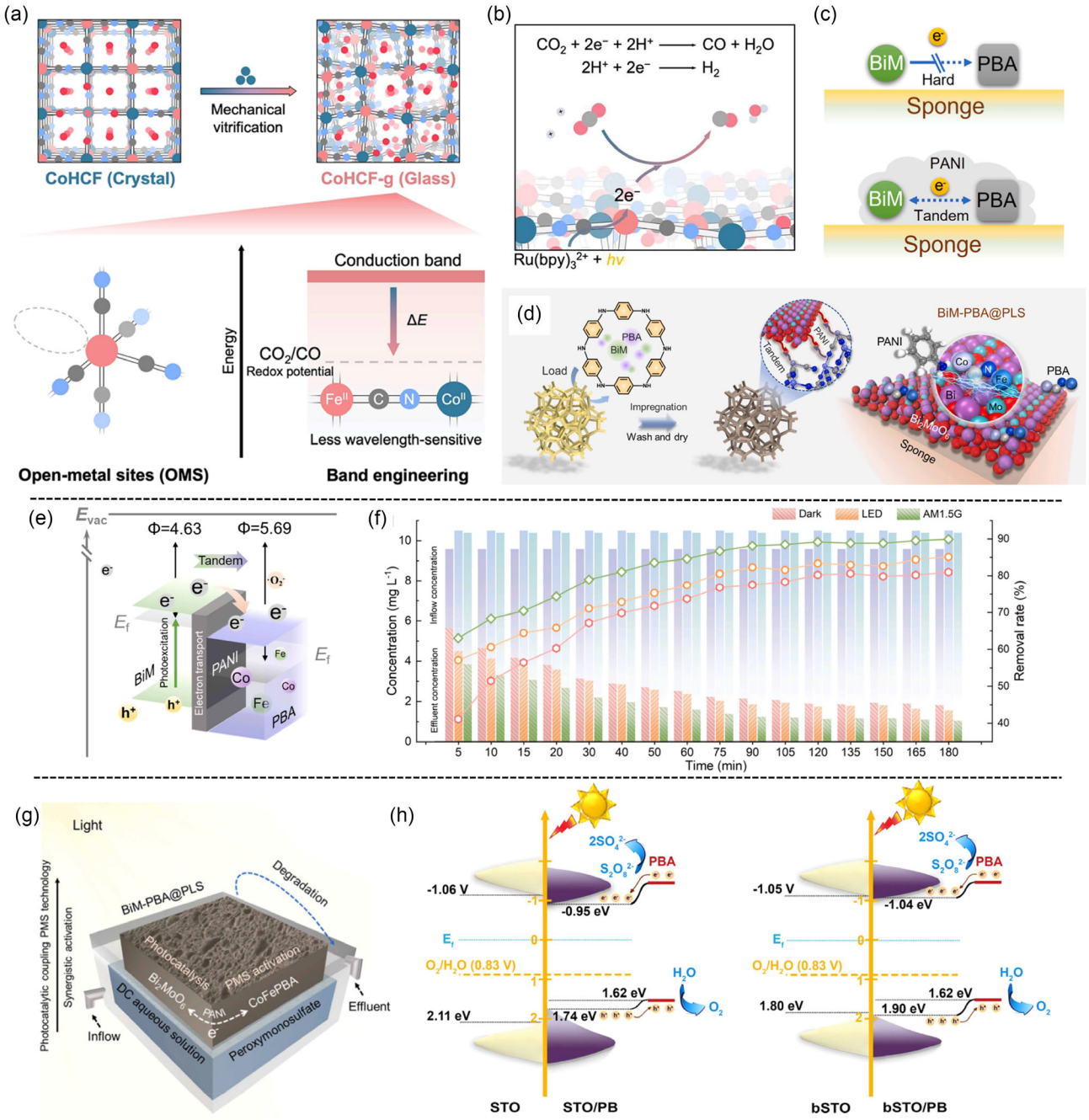

FIGURE 14 | (a) Schematic illustrations of the mechanically induced crystal–glass transformation of CoHCF and its effects on open-metal site (OMS) formation and band engineering suitable for CO_2 reduction. (b) Schematic diagram of photoinduced CO_2 reduction on the CoHCF-g surface. Reprinted with permission [216]. Copyright 2024, American Chemical Society. (c) Schematic representation of highly conductive PANI in combination with Bi_2MoO_6 and PBA. (d) Synthesis schematic illustration. (e) Diagrammatic illustration of the consecutive hybrid catalysis system employing BiM–PBA@PLS. (f) Performance of BiM–PBA@PLS in continuous flow reactions under varying illumination conditions. (g) Schematic diagram of the tandem hybrid catalysis system reactor. Reprinted with permission [209]. Copyright 2023, Elsevier B.V. (h) Energy band diagram representation for STO, STO/PB, bSTO, and bSTO/PB samples. Reprinted with permission [217]. Copyright 2023, The Authors.

biocompatibility, and biodegradability. As nanotechnology continues to evolve, a variety of PB-focused nanoplatforms have been created for use in biomedical fields. Finally, this review identifies current obstacles in existing studies on proposes potential directions for future research and applications of PB-based nanoplatforms, providing a framework to guide further advancements [219]. Furthermore, PB is a coordination network featuring the Fe^{2+}–CRN–Fe^{3+} mixed-valence state, representing a classical metal complex. This structure includes a C atom coordinated with Fe^{2+} (low spin) and an N atom bonded to Fe^{3+} (high spin). Both PB and PBAs exhibit outstanding biosafety, desirable magnetic features, exceptional photothermal capabilities, and the ability to simulate enzymatic activities. Such attributes stem from their stable structure, adjustable size, controllable shape, diverse modification approaches, and significant physicochemical characteristics. Consequently, they have drawn growing attention and

shown substantial potential in biomedical applications. This review systematically reviews and evaluates recent progress in the development on PB-based nanomaterials used in biomedical applications. This review systematically reviews the preparation methods for PB development, encompassing both conventional synthesis techniques and innovative approaches. Beyond summarizing the current state of preparation methodologies, particular emphasis is placed on specific PB-based nanomaterials that have demonstrated promising outcomes in targeted biomedical applications. Moreover, this review explores key factors and potential advancements necessary for translating PB materials into clinical use as multifunctional nanomaterials. Overall, this article provides a comprehensive guide for advancing the development and biomedical application of PB-based nanomaterials [220]. Below that, messenger RNA (mRNA) constitutes a revolutionary category of nucleic acid-based therapeutic agents for genome editing and addressing genetic disorders. However, achieving efficient and selective delivery of exogenous mRNA to specific cell types remains a critical challenge in expanding its biomedical applications and advancing targeted gene therapy. In this research, scientists effectively showcase the selective delivery of mRNA to specific cells and genome editing using CRISPR/Cas9 by altering the interaction between lipid nanoparticles (NPs) derived from PBA on the cell surface. A cationic lipid containing a PBA moiety, referred to as PBA-BADP, was developed to create nanoparticles with mRNA through electrostatic forces. Notably, these nanoparticles exhibit PBA groups exposed on their external surface, facilitating increased uptake by cancer cells that overexpress SA. This occurs due to specific interactions between PBA and SA at the interface. Research has shown that transfecting cells with PBA-BADP/mRNA nanoparticles leads to a 300-times greater expression of the luciferase reporter gene in cancer cells than in non-cancerous cells. Additionally, experimental results indicate that the delivery of tumor suppressor p53 mRNA via PBA-BADP specifically restrains the growth of cancer cells. Simultaneously, the administration of PBA-BADP/Cas9 mRNA nanoparticles successfully suppresses gene expression in HeLa cancer cells with significantly higher efficacy compared with normal cells. Scientists suggest that these results may enhance the application of PBA-SA interactions, leading to advancements in mRNA delivery mechanisms and genome editing techniques for sophisticated gene therapies [221]. Moreover, improving diabetic wound healing remains a significant global challenge. A recent study presented an innovative hydrogel that integrates glucose-responsive hyperglycemia management with robust antioxidant properties to enhance diabetic wound repair. Using a one-step synthesis method, gallic acid (GA), renowned for its potent antioxidant capabilities, was conjugated to chitosan (CS) chains. The revised CS-GA was integrated into a poly(ethylene glycol) diacrylate (PEG-DA) hydrogel framework, resulting in a new type of antioxidant hybrid hydrogel (PEG-DA/CS-GA). At the same time, polyethyleneimine (PEI) was modified with a distinct glucose-responsive PBA molecule for insulin encapsulation, creating PEI-PBA/insulin nanoparticles (NPs). The NPs can be incorporated into the PEG-DA/CS-GA hybrid hydrogel through dynamic borate bonds that are established between the phenylboronic acid groups on PEI-PBA and the polyphenol groups on CS-GA. The results indicated that the PEG-DA/PEI-PBA/insulin/CS-GA (PPIC) hydrogel system displayed excellent biocompatibility along with outstanding antioxidant properties, achieving a DPPH scavenging efficiency of over 95.0%. It successfully safeguarded cells against oxidative stress through the reduction of malondialdehyde (MDA) levels, the augmentation of superoxide dismutase (SOD) activity, and the preservation of balanced glutathione (GSH)/oxidized glutathione (GSSG) ratios. Additionally, The PPIC hydrogel demonstrated remarkable glucose-responsive insulin release properties and efficiently regulated blood glucose levels. Overall, these findings emphasize the promising capabilities of the PPIC hydrogel as a strong and efficient system for addressing diabetic wound treatment [222].

8.4 | Others

The CuFeO was synthesized via a straightforward thermal treatment of Cu–Fe PBAs. The resultant CuFeO exhibited remarkable catalytic performance across a broad pH range. Under near-neutral conditions (pH = 6.0), 95.42% of sulfamethoxazole was effectively removed within 30 min using the photo-Fenton process. ESR/DMPO and radical quenching experiments verified the involvement of both hydroxyl radicals (·OH) and superoxide radicals ($\cdot O_2^-$), with ·OH playing a more predominant role in SMZ degradation. Intermediates of SMZ degradation were recognized via liquid chromatography-mass spectrometry (LC-MS) analysis, and a reasonable degradation pathway was put forward. Moreover, CuFeO demonstrated exceptional stability and reusability, retaining its efficiency over five consecutive cycles. Given its minimal metal leaching, magnetic properties, and robust catalytic activity, the synthesized CuFeO shows great potential for practical applications in organic wastewater treatment. In addition, a novel layered double hydroxide based on PBA (PBA@ZnTi-LDH) was synthesized in situ and employed to remove radioactive Cs^+ ions from wastewater. The results demonstrated that this PBA@ZnTi-LDH, which employed LDH as both a structural framework and a source of transition metals, exhibited superior adsorption capacity and water stability compared to traditional PBAs, thereby showing significant potential for large-scale Cs^+ removal. To enhance its practical applicability, it was encapsulated within calcium alginate, forming PBA@ZnTi-LDH/CaALG. This composite material showed excellent performance in both post-separation and fixed-bed adsorption under different Cs^+ concentrations and flow rates. This indicates its adaptability for treating diverse types of Cs^+-contaminated wastewater. Additionally, the practical applicability of Cs^+ removal was assessed through experiments using naturally complex water samples containing Cs^+. As a result, the stable and readily separable PBA@ZnTi-LDH/CaALG demonstrated high efficiency, selectivity, and reusability when removing Cs^+. This makes it a very promising option for the large-scale treatment of actual wastewater contaminated with Cs^+ [223]. Furthermore, inspired by the structural characteristics of corn, a nickel-iron PBA nanocage-decorated magnesium hydroxide composite was successfully developed. In this novel design, rod-shaped magnesium hydroxide (RMH) played the role of the “corn cob,” while PBAs served as the “corn kernels.” PDA acted as the binding layer that connected RMH and PBA. Subsequently, the RMH@PDA@PBA composite was incorporated into epoxy resin (EP) with the aim of enhancing its flame-retardant properties and mechanical performance. The EP composite containing RMH@PDA@PBA was thoroughly analyzed in terms of its composition, structure, and morphology. Furthermore, when compared to the pristine EP, there was a

reduction of 43.1%, 50.0%, 43.9%, and 56.3% in the PHRR, PSPR, THR200, and TSP200 for EP/3RMH@PDA@PBA, respectively [190]. Consequently, this research focusing on nature-inspired hierarchical nanostructures offers a novel approach for the effective development of fire-safe polymers [224]. In addition, PB is generally acknowledged as a pigment crystal that can selectively separate radioactive cesium ions released from aqueous solutions. This is because the cage size of PB is similar to that of the cesium ion. However, the small size of PB poses significant challenges in handling, leading to the development of PB-containing adsorbents primarily in composite forms, which inevitably compromises the efficiency of cesium isolation. Recently, PB nanocrystals have been successfully and stably anchored onto the surface of millimeter-sized porous polyacrylamide (PAAm) spheres (PB@PAAm) is formed via the crystallization of PB on PAAm that has pre-adsorbed Fe^{3+}. The securely immobilized PB nanocrystals have shown to be highly selective and efficient adsorbents for eliminating radioactive cesium. The PB@PAAm adsorbents possess a well-connected spherical pore structure and a millimeter-scale diameter. This structure not only enables the rapid penetration of Cs^+ into the material but also improves its handling convenience. Noteworthy is the fact that the highly interconnected spherical pores enable PB@PAAm to reach 90% of its maximum Cs^+ adsorption capacity in merely 30 min. In addition, PB@PAAm demonstrates an outstanding Cs^+ capture capacity of 374 mg/g. Even at low Cs^+ concentrations, it has a high removal efficiency that exceeds 85%. Moreover, in the presence of competing ions like Na^+, K^+, Mg^{2+}, and Ca^{2+}, it shows remarkable selectivity for Cs^+ [225]. Less than that, maintaining the structural integrity of electrode materials with high reversibility is critical for improving the long-term cyclic stability of battery systems. Nevertheless, during the charge–discharge cycles, the majority of electrode materials experience degradation. This is because of an unavoidable rise in entropy. To tackle this challenge, a self-healing strategy has been devised, enabling morphological restoration in PBA cathodes via cobalt doping. The electric field modulates the kinetic dynamics, diverging from traditional thermodynamics, and facilitates the "electrochemically driven dissolution–recrystallization process," which is responsible regarding the periodic self-healing behavior [226]. Moreover, to meet the current energy demands of society, there is an urgent need for extremely effective and uninterrupted generation related to renewable energy. One of the primary challenges in green hydrogen production lies in developing efficient and cost-effective electrocatalysts. PBAs, and their derivatives possess adjustable metal centers, which render them promising candidates as innovative photo- and electrochemical catalysts. This paper systematically reviews and synthesizes recent advancements in hollow structures based on PB/PBA, nanostructures supported by substrates, and their related derivatives, with a focus on their applications in sustainable water splitting. This study explores the synthesis techniques and formation processes of the materials in question. Finally, the paper underscores the existing constraints and major challenges within this domain. The authors are confident that this review will inspire additional research endeavors aimed at improving technologies that leverage these sophisticated PB/PBA structures and their derivatives for effective and eco-friendly water splitting [227]. Furthermore, tubular nanoreactors, renowned for their distinctive void-confinement effect, have attracted considerable attention in catalytic applications. However, achieving controllable synthesis and synergistically enhancing performance remains a significant challenge. In this research, scientists put forward a synthetic method guided by template polymerization to incorporate hollow PBA boxes within conductive polypyrrole nanotubes (H-CoFe PBA@PPy NTs). This structure functions as an effective activator for peroxymonosulfate in the catalytic oxidation process of toxic organic contaminants. According to experimental findings, the production of multiple reactive oxygen species within these nanotubes is crucial for the markedly improved catalytic efficiency observed in dye degradation processes. The outstanding catalytic activity is primarily due to the inherent bimetallic CoFe PBA, as it supplies a wealth of active sites (Figure 15). Moreover, the distinctive nanotubular structure enables the concentration of reactant molecules within a confined spatial domain, while the superior electron and mass transport characteristics further augment the catalytic efficiency [228].

9 | Summary and Outlook

The critical need for rechargeable batteries exhibiting high energy density, exceptional rate performance, extended cycling stability, and cost-effectiveness has spurred growing interest in exploring new cathode materials. Given the limitations associated with traditional cathode hosts like oxides and polyanionic compounds, PBAs have gained attention due to their unique open framework. Their principal benefits encompass simple synthesis routes, flexible chemical composition, and the capability to accommodate a range of alkali metal ions, notably inexpensive Na^+ and K^+. However, the insertion of multivalent cations (e.g., Mg^{2+}, Ca^{2+}, Zn^{2+}, Al^{3+}) poses a considerable difficulty, with limited successes to date. Additionally, the inherently low volumetric energy density of PBA-based electrodes may ultimately restrict their application scope to large-scale stationary battery systems. The PB compounds of these four elements as cathodes of multivalent ion batteries in aqueous solutions and aprotic electrolytes are listed in Table 2 below.

PBAs have garnered substantial interest in electrochemical energy storage applications are favored for their low cost, stable porous structure, straightforward synthesis methods, and environmental benignity. This review offers a thorough overview of the crystal arrangements and electrochemical reaction processes, and approaches to improving the evaluation of PBA material properties. Furthermore, we explore the potential applications of advanced PBAs as cathode substances utilized in proton, ammonium-ion, and multicharge batteries. Looking forward, several promising avenues for the advancement of PBA materials in energy storage and conversion technologies are outlined below:

1. The inherent electrochemical properties of PBA materials are significantly influenced by crystal vacancies, as these vacancies can increase the structural water content and consequently reduce the number of redox-active sites. Enhancing crystallinity is critical for developing high-performance PBA materials. We propose that carefully selecting complexing agents during synthesis offers the most practical method to improve the crystallization of PBA materials, especially for large-scale production. Furthermore, the low electrical conductivity of PBA

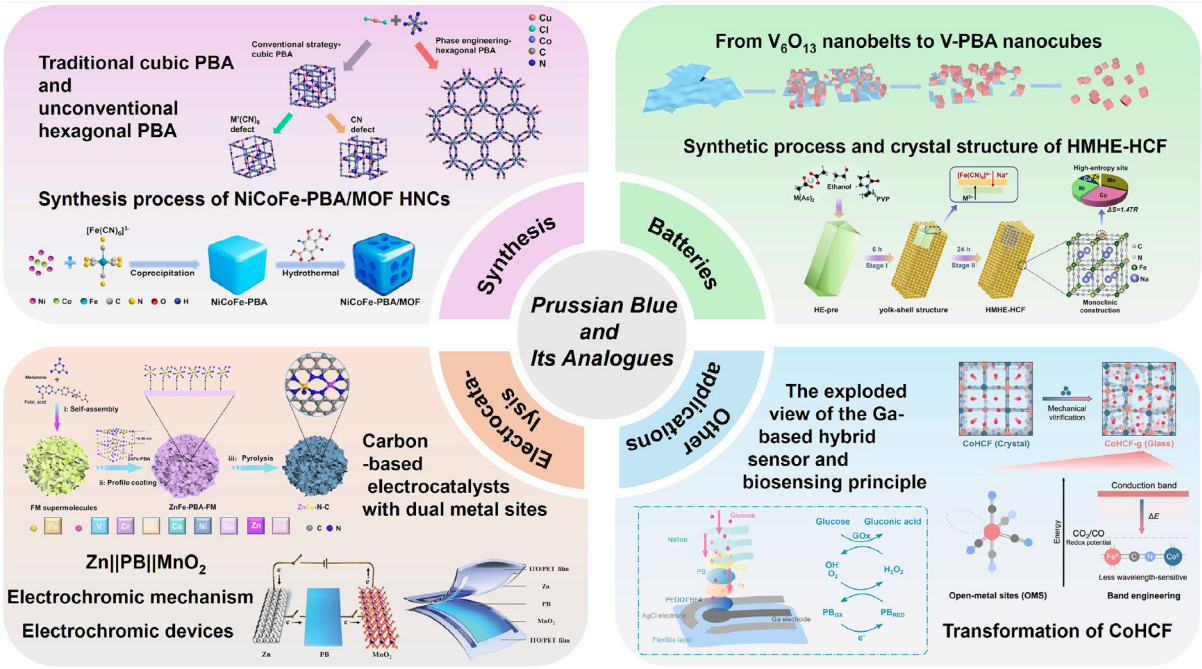

FIGURE 15 | Introduction the application of PBAs in synthesis, batteries, electrocatalysis, and other applications.

TABLE 2 | The PB compounds as cathodes for multivalent-ion batteries in aqueous and aprotic electrolytes.

Multivalent-ion		PB composition	Redox couple	Voltage, (V)	Capacity, (mAh g^{-1})
Mg	Aqueous electrolyte (vs. SHE)	$K_{0.6}Ni_{1.2}[Fe(CN)_6] \cdot 3.6H_2O$	L-Fe^{3+}/Fe^{2+}	0.6	52
Mg	—	$K_{0.1}Cu[Fe(CN)6]_{0.7} \cdot 3.6H_2O$	L-Fe^{3+}/Fe^{2+}	0.8	60
Mg	—	—	H-Cu^{2+}/Cu^{+}	—	—
Mg	—	$K_{1.6}Cu[Fe(CN)_6]_{0.9} \cdot 1.4H_2O$	L-Fe^{3+}/Fe^{2+}	0.6	60
Mg	—	—	H-Cu^{2+}/Cu^{+}	—	—
Mg		$Na_{1.4}Ni_{1.3}[Fe(CN)_6] \cdot 5H_2O$	L-Fe^{3+}/Fe^{2+}	0.7	65
Mg	Aprotic electrolyte (vs. Mg^{2+}/Mg)	$Na_{0.69}Fe[Fe(CN)_6]$	L-Fe^{3+}/Fe^{2+}	3.2	70
Mg	—	—	H-Fe^{3+}/Fe^{2+}	2.6	—
Mg	—	$Fe[Fe(CN)_6]_{0.95} \cdot 0.7H_2O$	L-Fe^{3+}/Fe^{2+}	2.6	125
Mg	—		H-Fe^{3+}/Fe^{2+}	2.1	—
Mg	—	$K_{1.6}Cu[Fe(CN)_6]_{0.9} \cdot 1.4H_2O$	L-Fe^{3+}/Fe^{2+}	3	/
Mg	—		H-Cu^{2+}/Cu^{+}	—	—
Ca	Aqueous electrolyte	$K_{0.6}Ni_{1.2}[Fe(CN)_6] \cdot 3.6H_2O$	L-Fe^{3+}/Fe^{2+}	0.59	50
Ca	—	$K_xCu[Fe(CN)_6]$	L-Fe^{3+}/Fe^{2+}	0.84	75
Ca	Aprotic electrolyte (vs. Ca^{2+}/Ca)	$K_2Ba[Fe(CN)_6]$	L-Fe^{3+}/Fe^{2+}	3.2	55.8
Ca	—	$Na_{0.45}Ni[Fe(CN)_6]$	L-Fe^{3+}/Fe^{2+}	2.6	60
Ca	—	$K_xNi[Fe(CN)_6]$	L-Fe^{3+}/Fe^{2+}	3.1	50
Ca	—	$KFe[Fe(CN)_6]$	H-Fe^{3+}/Fe^{2+}	3.3	150
Ca	—	$Na_{1.1}Mn[Fe(CN)_6]$	H-Mn^{3+}/Mn^{2+}	3.4	80
Zn	Aqueous electrolyte (vs. Zn^{2+}/Zn)	$KCu[Fe(CN)_6]$	L-Fe^{3+}/Fe^{2+}	1.7	56

(Continues)

TABLE 2 | (Continued)

Multivalent-ion		PB composition	Redox couple	Voltage, (V)	Capacity, (mAh g^{-1})
Zn	—	$K_{0.71}Cu[Fe(CN)_6]_{0.72} \cdot 3.5H_2O$	L-Fe^{3+}/Fe^{2+}	1.73	60
Zn	—	$Zn_3[Fe(CN)_6]_2$	L-Fe^{3+}/Fe^{2+}	1.7	73.7
Zn	—	$KCu[Fe(CN)_6]$	L-Fe^{3+}/Fe^{2+}	1.7	60
Zn	—	$Fe[Fe(CN)]_6$	L-Fe^{3+}/Fe^{2+}	1.5	120
Zn	—	—	H-Fe^{3+}/Fe^{2+}	—	—
Zn	—	$Na_{0.61}Fe_{0.94}[Fe(CN)_6]$	L-Fe^{3+}/Fe^{2+}	1.1	73.5
Zn	—	—	H-Fe^{3+}/Fe^{2+}	—	—
Zn	—	$Zn_2[Fe(CN)_6]$	L-Fe^{3+}/Fe^{2+}	1.5	78
Zn	—	$Na_{0.63}(VO)_{1.3}[Fe(CN)_6] \cdot 5.8H_2O$	H-V^{3+}/V^{4+}	1	187
Zn	—	—	H-V^{4+}/V^{5+}	—	—
Zn	—	—	L-Fe^{2+}/V^{3+}		—
Zn	Aprotic electrolyte (vs. Zn^{2+}/Zn)	$Na_{0.45}Ni[Fe(CN)_6]$	L-Fe^{3+}/Fe^{2+}	1.2	70
Zn		$K_{1.51}Ni[Fe(CN)_6]_{0.954} \cdot 0.766H_2O$	L-Fe^{3+}/Fe^{2+}	1.29	55.6
Al	Aqueous electrolyte (vs. SHE)	$KCu[Fe(CN)_6] \cdot 8H_2O$	L-Fe^{3+}/Fe^{2+}	0.84	62.9
Al	—	$K_{0.03}Cu[Fe(CN_6]_{0.65} \cdot 2.6H_2O$	L-Fe^{3+}/Fe^{2+}	0.76	50
Al	—	$K_{0.02}Cu[Fe(CN)_6]_{0.7} \cdot 3.7H_2O$	L-Fe^{3+}/Fe^{2+}	0.72	55
Al	Aprotic electrolyte (vs. Al^{3+}/Al)	$K_xCu[Fe(CN)_6]$	L-Fe^{4+}/Fe^{3+}	1.3	14
Al	—	—	L-Fe^{3+}/Fe^{2+}	0.85	—
Al	—	—	H-Cu^{2+}/Cu^{+}	0.45	—

materials constitutes another major barrier to their commercial application. Introducing various conductive carbon materials during synthesis represents an effective strategy to overcome this limitation.

2. Energy storage devices in the future demand next-generation PBA materials with enhanced operating voltages, superior rate performance, enhanced cycling stability, and increased capacity. To achieve these goals, various optimization strategies can be adopted, including minimizing crystal vacancies, conducting metal substitution, establishing concentration gradients or core–shell structures, and engineering advanced morphologies. Among these approaches, metal substitution stands out as it enables fundamental and modulation at the atomic level of the electrochemical characteristics of PBA electrodes. Furthermore, we highlight that high-throughput methods for optimizing the composition of PBA materials provide a feasible pathway to discover high-performance candidates.

3. It has been widely reported that PBA materials demonstrate exceptional electrochemical aqueous battery performance. Nevertheless, the energy storage principle of these materials continues to be a topic of active discussion. Beyond the traditional insertion and removal of charge carrier ions, experimental evidence has shown the concurrent insertion and the elimination of protons and metal ions, especially in aqueous zinc-ion batteries. In our opinion, the participation of proton intercalation in PBA materials can significantly enhance reaction kinetics. This is a crucial element for achieving high power density in aqueous batteries. Therefore, more systematic studies should be centered on exploring the electrochemical properties of PBA materials in aqueous electrolytes.

4. In the context of intercalating the incorporation of multivalent ions into PBA-based electrode materials. The main reason for the slow diffusion kinetics is the intense electrostatic interactions taking place between multivalent ions and the host lattice. Research has indicated that structural water is capable of promoting the diffusion of multivalent ions through a charge shielding mechanism. However, as stated earlier, the presence of structural H_2O in PBAs could promote

the formation of crystal vacancies. This, in consequence, reduces the cyclic stability of the electrode material. Therefore, attaining an optimal balance between the structural water content and the cycle life durability of PBA electrode materials is of great significance for improving PBA hosts designed for multivalent ion storage applications.

5. It is also essential to conduct further investigations into more sophisticated synthesis techniques in order to enhance crystal stability, improve the reversibility of oxidation-reduction reactions, optimize the carrier ion diffusion dynamics, increase electrical conductivity in ionic/electronic systems, elevate the working voltage of electrodes, minimize unwanted side reactions, and boost the contributions of capacitance to the electrode capacity. This review offers an in-depth overview of PBA materials and aims to guide future studies and advancements in the application of PBA materials within energy storage and conversion domains.

Acknowledgments

This work was supported by the National Natural Science Foundation of China (52371240).

Funding

This work was supported by National Natural Science Foundation of China (52371240).

Conflicts of Interest

The authors declare no conflicts of interest.

References

1. S. Yi, W. Zhou, Z. Wang, M. Yang, J.-F. Wu, and J. Liu, "Layered K2Mg2TeO6 Solid Electrolyte Enables Long-Life Solid-State Potassium Batteries," *ACS Energy Letters* 9, no. 6 (2024): 2626–2632.

2. K. Sun, J. C. Dong, H. Sun, et al., "Co(CN)3 Catalysts with Well-Defined Coordination Structure for the Oxygen Reduction Reaction," *Nature Catalysis* 6, no. 12 (2023): 1164–1173.

3. W. Wang, W. Zhang, R. Yu, et al., "Molecular Engineering to Construct MoS2 with Expanded Interlayer Spacing and Enriched 1T Phase for "Rocking-Chair" Aqueous Calcium-Ion Pouch Cells," *ACS Nano* 18, no. 52 (2024): 35286–35295.

4. Z. Tang, B. Hu, P. Nie, et al., "Ni-PBA on Hollow Graphite Tube for Capacitive Deionization with Exceptional Stability," *Chemical Engineering Journal* 466 (2023): 143216.

5. T. Z. Yang, D. Luo, X. Y. Zhang, et al., "Sustainable Regeneration of Spent Cathodes for Lithium-Ion and Post-Lithium-Ion Batteries," *Nature Sustainability* 7, no. 6 (2024): 776–785.

6. C. Gao, J. Li, T. Sun, et al., "Chemical Long-Range Disorder in Prussian Blue Analogues for Potassium Storage," *ACS Energy Letters* 9, no. 9 (2024): 4248–4254.

7. Z. Qian, R.-J. Luo, C. Ma, et al., "Six Element High-Entropy Prussian Blue Analogue Cathode Enabling High Cycle Stability for Sodium-Ion Batteries," *Chemical Engineering Journal* 500 (2024): 156767.

8. Z. He, G. Wang, R. Yu, et al., "Enhancing Proton Co-Intercalation in Iron Ion Batteries Cathodes for Increased Capacity," *ACS Nano* 18, no. 26 (2024): 17304–17313.

9. M. Chen, H. Meng, F. Wang, et al., "Dispersed Mn2Co2C Nanoparticles in Interconnected Nitrogen-Doped Carbon Framework as Cathode Catalysts for Efficient and Long-Life Li-CO2 Batteries," *Chemical Engineering Journal* 455 (2023): 140564.

10. Y. Li, J.-P. Qu, J.-Y. Wang, et al., "Unlocking the Electrochemical Ammonium Storage Performance of Copper Intercalated Hexacyanoferrate," *Chemical Engineering Journal* 503 (2025): 158266.

11. Z. Chen, Y. Wang, J. Wang, et al., "A MXene Modification Strategy of Prussian Blue Cathodes toward a Stable Cathode Electrolyte Interphase and Suppressed Mn Dissolution," *Chemical Engineering Journal* 505 (2025): 159519.

12. P. A. Shinde, N. R. Chodankar, H.-J. Kim, et al., "Ultrastable 1T-2H WS2 Heterostructures by Nanoarchitectonics of Phosphorus-Triggered Phase Transition for Hybrid Supercapacitors," *ACS Energy Letters* 8, no. 10 (2023): 4474–4487.

13. H. Ma, R. Chen, B. Liu, et al., "Synthesis of Ultrasmall Vanadium Ferricyanide Nanocrystallines with the Aidance of Graphene Self-Assembled Fibers towards Reinforced Zinc Storage Performance," *Chemical Engineering Journal* 489 (2024): 151112.

14. S.-W. Ma, S.-L. Wang, X.-L. Yang, et al., "Prussian Blue Analog-Based Ionic Liquid for Highly Efficient Cesium Removal From Wastewater," *Chemical Engineering Journal* 504 (2025): 158803.

15. W. Wang, X. Yu, H. He, et al., "Electrochemical Reconstitution of Prussian Blue Analogue for Coupling Furfural Electro-Oxidation with Photo-Assisted Hydrogen Evolution Reaction," *Chemical Engineering Journal* 465 (2023): 142865.

16. J. Peng, W. Hua, Z. Yang, et al., "Structural Engineering of Prussian Blue Analogues Enabling All-Climate and Ultralong Cycling Sodium-Ion Batteries," *ACS Nano* 18, no. 30 (2024): 19854–19864.

17. Q. Zhou, H. K. Liu, S. X. Dou, and S. Chong, "Defect-Free Prussian Blue Analogue as Zero-Strain Cathode Material for High-Energy-Density Potassium-Ion Batteries," *ACS Nano* 18 (2024): 7287–7297.

18. A. J. Mayer, O. T. Beynon, A. J. Logsdail, et al., "Direct Monitoring of the Potassium Charge Carrier in Prussian Blue Cathodes Using Potassium K-Edge X-Ray Absorption Spectroscopy," *Journal of Materials Chemistry A* 11, no. 37 (2023): 19900–19913.

19. J. Dai, S. Tan, L. Wang, et al., "High-Voltage Potassium Hexacyanoferrate Cathode via High-Entropy and Potassium Incorporation for Stable Sodium-Ion Batteries," *ACS Nano* 17, no. 21 (2023): 20949–20961.

20. Y. Huang, W. Mu, J. Meng, X. Bi, X. Lei, and S. Luo, "Modification of Prussian Blue Analogues as High-Performance Cathodes for Sodium-Ion Batteries," *Chemical Engineering Journal* 499 (2024): 156410.

21. P. Hong, C. Xu, C. Yan, Y. Dong, H. Zhao, and Y. Lei, "Prussian Blue and Its Analogues for Commercializing Fast-Charging Sodium/Potassium-Ion Batteries," *ACS Energy Letters* 10, no. 2 (2025): 750–778.

22. Z. Wang, K. Nie, M. T. Sougrati, et al., "Charge Transfer Induced Highly Active Low-Spin Iron of Prussian Blue Cathode through Calcination Strategy for High Performance Sodium-Ion Batteries," *Chemical Engineering Journal* 488 (2024): 151090.

23. J. Ning, J. Hu, M. Zhou, et al., "In-Situ Pre-Sodiation of Prussian Blue for the Construction of High-Performance Sodium-Ion Batteries," *Chemical Engineering Journal* 489 (2024): 151531.

24. J. Chen, Z. Bai, X. Yu, W. Zhang, T. Jiang, and M. Wu, "Separator of Polyacrylonitrile Modified with Prussian Blue Analogs for High-Efficiency Aqueous Zinc-Ion Batteries," *Journal of Materials Chemistry A* 12, no. 25 (2024): 15486–15493.

25. J. Liu, Z. Shen, and C.-Z. Lu, "Research Progress of Prussian Blue and Its Analogues for Cathodes of Aqueous Zinc Ion Batteries," *Journal of Materials Chemistry A* 12, no. 5 (2024): 2647–2672.

26. F. Liu, S. Xu, W. Gong, et al., "Fluorescent Fiber-Shaped Aqueous Zinc-Ion Batteries for Bifunctional Multicolor-Emission/Energy-Storage Textiles," *ACS Nano* 17, no. 18 (2023): 18494–18506.

27. G. Yang, Z. Liang, Q. Li, Y. Li, F. Tian, and C. Wang, "Epitaxial Core-Shell MnFe Prussian Blue Cathode for Highly Stable Aqueous Zinc Batteries," *ACS Energy Letters* 8, no. 10 (2023): 4085–4095.

28. F. M. Maddar, D. Walker, T. W. Chamberlain, et al., "Understanding Dehydration of Prussian White: From Material to Aqueous Processed Composite Electrodes for Sodium-Ion Battery Application," *Journal of Materials Chemistry A* 11, no. 29 (2023): 15778–15791.

29. L. Ge, Y. Song, P. Niu, et al., "Elaborating the Crystal Water of Prussian Blue for Outstanding Performance of Sodium Ion Batteries," *ACS Nano* 18, no. 4 (2024): 3542–3552.

30. V. G. Panferov, W. Zhang, N. D'Abruzzo, S. Wang, and J. Liu, "Kinetic Profiling of Oxidoreductase-Mimicking Nanozymes: Impact of Multiple Activities, Chemical Transformations, and Colloidal Stability," *ACS Nano* 18 (2024): 34870–34883.

31. B. Bornamehr, V. Presser, A. J. G. Zarbin, Y. Yamauchi, and S. Husmann, "Prussian Blue and Its Analogues as Functional Template Materials: Control of Derived Structure Compositions and Morphologies," *Journal of Materials Chemistry A* 11, no. 20 (2023): 10473–10492.

32. S. Eun, E. Cho, J. Ryu, et al., "Enhanced Cesium Adsorption and Desorption Mechanisms in ZnFe Prussian Blue Analogs: Structural Transformation and Reusability," *Chemical Engineering Journal* 505 (2025): 159161.

33. Y. Wang, N. Jiang, C. Yang, et al., "High-Entropy Prussian Blue Analogs with 3D Confinement Effect for Long-Life Sodium-Ion Batteries," *Journal of Materials Chemistry A* 12, no. 9 (2024): 5170–5180.

34. G. Ma, X. Zhou, Y. Cao, et al., "Sulfonated Polyaniline Coated Prussian Blue Analog Derived Mn-Fe Oxide Composite Electrode for All-Solid-State Flexible Supercapacitors," *Chemical Engineering Journal* 508 (2025): 160942.

35. L. Chen, S. Tang, J. Zhang, et al., "Prussian Blue Nanohybridized Multicellular Spheroids as Composite Engraftment for Antioxidant Bone Regeneration and Photoacoustic Tomography," *ACS Nano* 18, no. 36 (2024): 24770–24783.

36. J. Yao, J. Xing, Y. Yao, et al., "Ytterbium Doping-Retooled Prussian Blue for Tumor Metabolism Interference Therapy," *ACS Nano* 18, no. 52 (2024): 35758–35770.

37. J. Yao, Y. Qiu, J. Xing, et al., "Highly-Efficient Gallium-Interference Tumor Therapy Mediated by Gallium-Enriched Prussian Blue Nanomedicine," *ACS Nano* 18, no. 7 (2024): 5556–5570.

38. Q. Ke, K. Jiang, H. Li, L. Zhang, and B. Chen, "Hierarchically Micro-, Meso-, and Macro-Porous MOF Nanosystems for Localized Cross-Scale Dual-Biomolecule Loading and Guest-Carrier Cooperative Anticancer Therapy," *ACS Nano* 18 (2024): 21911–21924.

39. Y. Guo, Z. Chen, D. Jiang, et al., "Evolution of CuCoFe Prussian Blue Analogues with Open Nanoframe Architectures for Enhanced Capacitive Deionization," *Chemical Engineering Journal* 495 (2024): 153714.

40. Q. Zhong, T. Zhang, Z. Huang, et al., "In-Situ Immobilization of Fe PBA in the Zeolite Structure for Efficient Degradation of Benzalkonium Chloride: Towards Compressed Reaction Site Loss and Promoted PMS Utilization," *Chemical Engineering Journal* 501 (2024): 157655.

41. R. Yang, D. Zhang, H. Gao, Y. Wang, N. Li, and H. Zhang, "Size-Progressively-Reduced FeCoNi@C Nanoparticles Spatially Confined Within Polypyrrole-Derived Hollow Carbon Nanoboxes against Electromagnetic Contamination," *Chemical Engineering Journal* 495 (2024): 153114.

42. X. Ding, Q. Zhou, Z. Wang, et al., "An Ultra-Stable Mn-Based Prussian Blue Compound Effectively Suppresses Jahn-Teller Distortion as a Superior Cathode Material for Sodium-Ion Batteries," *Journal of Materials Chemistry A* 12, no. 40 (2024): 27598–27609.

43. H. Li, X. Ding, J. Shi, et al., "Crystal Face Dominated Fabrication of Prussian Blue Analogue with Oriented Growth and Naturally Nonpreferred Unsaturated Coordination Center," *Small* 19, no. 15 (2023): 2207525.

44. A. Simonov, T. De Baerdemaeker, H. L. B. Boström, et al., "Hidden Diversity of Vacancy Networks in Prussian Blue Analogues," *Nature* 578, no. 7794 (2020): 256.

45. G. X. Zhang, Y. Li, G. Y. Du, et al., "Spiral-Concave Prussian Blue Crystals with Rich Steps: Growth Mechanism and Coordination Regulation," *Angewandte Chemie-International Edition* 64 (2025): e202414650.

46. R. Fukushima, Y. Sekine, Z. Zhang, and S. Hayami, "Assembling Smallest Prussian Blue Analogs Using Chiral Hydrogen Bond-Donating Unit toward Complete Phase Transition," *Journal of the American Chemical Society* 146, no. 35 (2024): 24238–24243.

47. J. W. Yin, J. Wang, M. Z. Sun, et al., "Unconventional Hexagonal Open Prussian Blue Analog Structures," *Nature Communications* 16, no. 1 (2025): 370.

48. G. X. Zhang, Y. B. Lu, Y. Yang, et al., "Dynamic Phase Transformations of Prussian Blue Analogue Crystals in Hydrotherms," *Journal of the American Chemical Society* 146, no. 24 (2024): 16659–16669.

49. W. L. Wang, Y. Gang, Z. Hu, et al., "Reversible Structural Evolution of Sodium-Rich Rhombohedral Prussian Blue for Sodium-Ion Batteries," *Nature Communications* 11, no. 1 (2020): 980.

50. X. Y. Liu, Y. Cao, and J. Sun, "Defect Engineering in Prussian Blue Analogs for High-Performance Sodium-Ion Batteries," *Advanced Energy Materials* 12, no. 46 (2022): 2202532.

51. H. C. Yi, R. Z. Qin, S. X. Ding, et al., "Structure and Properties of Prussian Blue Analogues in Energy Storage and Conversion Applications," *Advanced Functional Materials* 31, no. 6 (2021): 2006970.

52. D. Baster, L. Kondracki, E. Oveisi, S. Trabesinger, and H. H. Girault, "Prussian Blue Analogue-Sodium-Vanadium Hexacyanoferrate as a Cathode Material for Na-Ion Batteries," *ACS Applied Energy Materials* 4, no. 9 (2021): 9758–9765.

53. Z. H. Zhou, Y. T. Dong, Y. Ma, et al., Innovative High-Entropy Strategy Extending Traditional Metal Substitution for Optimizing Prussian Blue Analogues in Rechargeable Batteries," *Susmat* 5, no. 2 (2025): e265.

54. J. Cattermull, M. Pasta, and A. L. Goodwin, "Structural Complexity in Prussian Blue Analogues," *Materials Horizons* 8, no. 12 (2021): 3178–3186.

55. M. W. Jiang, Z. D. Hou, L. B. Ren, Y. Zhang, and J. G. Wang, "Prussian Blue and Its Analogues for Aqueous Energy Storage: From Fundamentals to Advanced Devices," *Energy Storage Materials* 50 (2022): 618–640.

56. M. Hu, S. Furukawa, R. Ohtani, et al., "Synthesis of Prussian Blue Nanoparticles with a Hollow Interior by Controlled Chemical Etching," *Angewandte Chemie-International Edition* 51, no. 4 (2012): 984–988.

57. X. Wang, A. R. Dong, Z. Y. Zhu, et al., "Surfactant-Mediated Morphological Evolution of MnCo Prussian Blue Structures," *Small* 16, no. 43 (2020): e2004614.

58. Z. X. Cai, Z. L. Wang, J. Kim, and Y. Yamauchi, "Hollow Functional Materials Derived From Metal-Organic Frameworks: Synthetic Strategies, Conversion Mechanisms, and Electrochemical Applications," *Advanced Materials* 31, no. 11 (2019): 1804903.

59. J. W. Nai and X. W. Lou, "Hollow Structures Based on Prussian Blue and Its Analogs for Electrochemical Energy Storage and Conversion," *Advanced Materials* 31, no. 38 (2019): e1706825.

60. E. Mamontova, F. Salles, Y. Guari, J. Larionova, and J. Long, "Post-Synthetic Modification of Prussian Blue Type Nanoparticles: Tailoring

the Chemical and Physical Properties," *Inorganic Chemistry Frontiers* 9, no. 15 (2022): 3943–3971.

61. N. Kitchamsetti, J. S. Cho, and C. S. Chakra, "Prussian Blue Analogue Derived Porous Hollow Nanocages Comprising Polydopamine-Derived N-Doped C Coated CoSe2/FeSe2 Nanoparticles Composited with N-Doped Graphitic C as an Anode for High-Rate Na-Ion Batteries," *Chemical Engineering Journal* 495 (2024): 153353.

62. Y. C. Pi, H. Lin, Z. Y. Meng, et al., "Self-Template Synthesis of PBA/MOF Hollow Nanocubes for Aqueous Battery," *Chemical Engineering Journal* 499 (2024): 155618.

63. P. Zhou, X. L. Tang, Z. Q. Ren, et al., "Oriented Assembled Prussian Blue Analogue Framework for Confined Catalytic Decomposition of Ammonium Perchlorate," *Small (weinheim an Der Bergstrasse, Germany)* 19, no. 20 (2023): 2207023.

64. P. Wan, H. Xie, N. Zhang, et al., "Stepwise Hollow Prussian Blue Nanoframes/Carbon Nanotubes Composite Film as Ultrahigh Rate Sodium Ion Cathode," *Advanced Functional Materials* 30, no. 38 (2020): 2002624.

65. Y. J. Ma, Y. Ma, S. L. Dreyer, et al., "High-Entropy Metal-Organic Frameworks for Highly Reversible Sodium Storage," *Advanced Materials* 33, no. 34 (2021): 2101342.

66. J. D. Lu, H. Y. Duan, Y. Zhang, et al., "Directional Growth of Conductive Metal-Organic Framework Nanoarrays along 001 on Metal Hydroxides for Aqueous Asymmetric Supercapacitors," *ACS Applied Materials & Interfaces* 14, no. 22 (2022): 25878–25885.

67. C. S. Wu, P. B. Geng, G. X. Zhang, X. R. Li, and H. Pang, "Synthesis of Conductive MOFs and Their Electrochemical Application," *Small* 20, no. 17 (2024): 2207023.

68. J. Estelrich and M. A. Busquets, "Prussian Blue: A Nanozyme with Versatile Catalytic Properties," *International Journal of Molecular Sciences* 22, no. 11 (2021): 5993.

69. S. Sun, Y. J. Zhang, M. Wang, et al., "Design and Fabrication of Glass Metal-Organic Framework Membrane for Gas Separation," *Industrial & Engineering Chemistry Research* 64, no. 30 (2025): 14771–14788.

70. Z. C. Jiang, S. X. Wang, Y. Y. Lu, Z. Y. Meng, and H. Pang, "Conductive Metal-Organic Framework as an Emerging Platform with Electrochemical Energy Storage," *Coordination Chemistry Reviews* 544 (2025): 216983.

71. Y. Y. Cheng, X. C. Yin, Y. C. Li, et al., "Multiple-Readout Lateral Flow Immunoassay for the Sensitive Detection of Nitrofurazone Metabolites through Ultrabright AIE-MOF Coupled in-Situ Growth Strategy," *Biosensors & Bioelectronics* 262 (2024): 116556.

72. Q. Y. Ye, E. X. Yuan, J. Shen, et al., "Amphiphilic Polymer Capped Perovskite Compositing with Nano Zr-MOF for Nanozyme-Involved Biomimetic Cascade Catalysis," *Advanced Science* 10, no. 31 (2023): e2304149.

73. R. M. Rego, K. V. Ajeya, H. Y. Jung, et al., "Nanoarchitectonics of Bimetallic MOF@Lab-Grade Flexible Filter Papers: An Approach Towards Real-Time Water Decontamination and Circular Economy," *Small* 19, no. 45 (2023): 2302692.

74. Y. X. Shi, G. J. Song, B. Yang, et al., "Prussian Blue Analogues "Dressed" in MXene Nanosheets Tightly for High Performance Lithium-Ion Batteries," *Advanced Materials* 37, no. 8 (2025): 2416665.

75. R. C. Lian, Q. Y. Gao, Z. X. Zhao, et al., "Hierarchical MXene@PBA Nanohybrids towards High-Efficiency Flame Retardancy and Smoke Suppression of Robust yet Tough Polymer Nanocomposites at Ultra-Low Additions," *Composites Part B-Engineering* 267 (2023): 111074.

76. Y. B. Zhao, B. L. Liang, X. J. Wei, K. X. Li, C. C. Lv, and Y. Zhao, "A Core-Shell Heterostructured CuFe@NiFe Prussian Blue Analogue as a Novel Electrode Material for High-Capacity and Stable Capacitive Deionization," *Journal of Materials Chemistry A* 7, no. 17 (2019): 10464–10474.

77. Q. Hu, X. F. Liu, B. Zhu, et al., "Crafting MoC2-Doped Bimetallic Alloy Nanoparticles Encapsulated Within N-Doped Graphene as Roust Bifunctional Electrocatalysts for Overall Water Splitting," *Nano Energy* 50 (2018): 212–219.

78. N. M. Umesh, J. A. A. Jesila, and S. F. Wang, "Amperometric Detection of Antibiotic Drug Ciprofloxacin Using Cobalt-Iron Prussian Blue Analogs Capped on Carbon Nitride," *Microchimica Acta* 189, no. 1 (2022): 31.

79. X. Zhuang, S. Zhang, Y. Tang, F. Yu, Z. Li, and H. Pang, "Recent Progress of MOF/MXene-Based Composites: Synthesis, Functionality and Application," *Coordination Chemistry Reviews* 490 (2023): 215208.

80. C. L. Liu, Y. Bai, W. T. Li, F. Y. Yang, G. X. Zhang, and H. Pang, "In Situ Growth of Three-Dimensional MXene/Metal-Organic Framework Composites for High-Performance Supercapacitors," *Angewandte Chemie-International Edition* 61, no. 11 (2022): e202116282.

81. P. B. Li, Y. Z. Zhao, Y. Zhao, et al., "Trimetallic Prussian Blue Analogue Derived FeCo/FeCoNi@NPC Composites for Highly Efficient Microwave Absorption," *Composites Part B-Engineering* 246 (2022): 110268.

82. L. Li, H. T. Zhao, P. B. Li, et al., "Rough Porous N-Doped Graphene Fibers Modified with Fe-Based Prussian Blue Analog Derivative for Wide-Band Electromagnetic Wave Absorption," *Composites Part B-Engineering* 243 (2022): 110121.

83. J. M. Wang, B. B. Wang, X. J. Liu, J. T. Bai, H. Wang, and G. Wang, "Prussian Blue Analogs (PBA) Derived Porous Bimetal (Mn, Fe) Selenide with Carbon Nanotubes as Anode Materials for Sodium and Potassium Ion Batteries," *Chemical Engineering Journal* 382 (2020): 123050.

84. D. W. Jeong, K. Kim, G. Lee, et al., "Electrochemical Transparency of Graphene," *ACS Nano* 16, no. 6 (2022): 9278–9286.

85. F. Y. Meng, Z. B. Ding, X. T. Xu, Y. Liu, T. Lu, and L. K. Pan, "Metal Organic Framework-Derived Nitrogen-Doped Porous Carbon Sustained Prussian Blue Analogues for Efficient and Fast Hybrid Capacitive Deionization," *Separation and Purification Technology* 317 (2023): 123899.

86. X. Q. Xu, J. H. Xie, B. Liu, et al., "PBA-Derived FeCo Alloy with Core-Shell Structure Embedded in 2D N-Doped Ultrathin Carbon Sheets as a Bifunctional Catalyst for Rechargeable Zn-Air Batteries," *Applied Catalysis B-Environment and Energy* 316 (2022): 121687.

87. E. Mamontova, M. Rodríguez-Castillo, E. Oliviero, et al., "Designing Heterostructured Core@satellite Prussian Blue Analogue@Au-Ag Nanoparticles: Effect on the Magnetic Properties and Catalytic Activity," *Inorganic Chemistry Frontiers* 8, no. 9 (2021): 2248–2260.

88. M. Cheng, Y. Liu, D. L. Huang, et al., "Prussian Blue Analogue Derived Magnetic Cu-Fe Oxide as a Recyclable Photo-Fenton Catalyst for the Efficient Removal of Sulfamethazine at near Neutral pH Values," *Chemical Engineering Journal* 362 (2019): 865–876.

89. J. S. Chen, H. Li, Z. X. Pei, et al., "Catalytic Activity Atlas of Ternary Co-Fe-V Metal Oxides for the Oxygen Evolution Reaction," *Journal of Materials Chemistry A* 8, no. 31 (2020): 15951–15961.

90. X. Xu, H. F. Liang, F. W. Ming, Z. B. Qi, Y. Q. Xie, and Z. C. Wang, "Prussian Blue Analogues Derived Penroseite (Ni, Co)Se2 Nanocages Anchored on 3D Graphene Aerogel for Efficient Water Splitting," *ACS Catalysis* 7, no. 9 (2017): 6394–6399.

91. X. H. Xu, T. Wang, L. Su, Y. J. Zhang, L. J. Dong, and X. Y. Miao, "In Situ Synthesis of Superhydrophilic Amorphous NiFe Prussian Blue Analogues for the Oxygen Evolution Reaction at a High Current Density," *ACS Sustainable Chemistry & Engineering* 9, no. 16 (2021): 5693–5704.

92. H. Xu, H. Y. Shang, L. J. Jin, C. Y. Chen, C. Wang, and Y. K. Du, "Boosting Electrocatalytic Oxygen Evolution over Prussian Blue Analog/Transition Metal Dichalcogenide Nanoboxes by Photo-Induced Electron Transfer," *Journal of Materials Chemistry A* 7, no. 47 (2019): 26905–26910.

93. X. S. Guo, X. G. Yu, Z. J. Feng, et al., "Intercalation Synthesis of Prussian Blue Analogue Nanocone and Their Conversion into Fe-Doped CoxP Nanocone for Enhanced Hydrogen Evolution," *ACS Sustainable Chemistry & Engineering* 6, no. 7 (2018): 8150–8158.

94. C. J. Xuan, J. Wang, W. W. Xia, et al., "Porous Structured Ni-Fe-P Nanocubes Derived From a Prussian Blue Analogue as an Electrocatalyst for Efficient Overall Water Splitting," *ACS Applied Materials & Interfaces* 9, no. 31 (2017):26134–26142.

95. G. X. Zhang, Y. L. Li, X. Xiao, et al., "In Situ Anchoring Polymetallic Phosphide Nanoparticles Within Porous Prussian Blue Analogue Nanocages for Boosting Oxygen Evolution Catalysis," *Nano Letters* 21, no. 7 (2021): 3016–3025.

96. X. Q. Wang, J. H. Zhou, W. G. Cui, et al., "Electron Manipulation and Surface Reconstruction of Bimetallic Iron-Nickel Phosphide Nanotubes for Enhanced Alkaline Water Electrolysis," *Advanced Science* 11, no. 26 (2024): 2401207.

97. J. Wang, L. P. Wang, Z. Y. Li, et al., "Fe-Doped Phosphide Nanosheet Array Derived From Prussian Blue Analogues for High-Efficient Electrocatalytic Water Splitting," *International Journal of Hydrogen Energy* 88 (2024): 52–61.

98. J. J. Jing, X. Wang, X. Q. Hao, and Z. L. Jin, "Strong Electron Coupling Effect of Prussian Blue Analogs Derived Ultrathin Nitrogen-Doped Carbon Wrapped Fe-CoP for Enhanced Wide Spectrum Photocatalytic H2 Evolution," *Advanced Sustainable Systems* 8, no. 12 (2024): 2400639.

99. J. Shi, W. Peng, Y.-F. Yang, et al., "A General Strategy for Synthesis of Binary Transition Metal Phosphides Hollow Sandwich Heterostructures," *Small* 19, no. 30 (2023): 2302906

100. Y. Chen, S. Zhang, F. Sun, et al., "Upgrading Electron Transfer with High Conductivity MOF Composites for Supercapacitors," *Chemistry-a European Journal* 31, no. 22 (2025): e202500090.

101. H. T. Xie, L. M. Mao, and J. Mao, "Structural Evolution of Ce Fe(CN) 6 and Derived Porous Fe-CeO2 with High Performance for Supercapacitor," *Chemical Engineering Journal* 421 (2021): 127826.

102. Y. M. Shi, P. H. Chen, J. Z. Chen, et al., "Hollow Prussian Blue Analogue/g-C3N4 Nanobox for All-Solid-State Asymmetric Supercapacitor," *Chemical Engineering Journal* 404 (2021): 126284.

103. L. J. Kong, M. Zhong, W. Shuang, Y. H. Xu, and X. H. Bu, "Electrochemically Active Sites inside Crystalline Porous Materials for Energy Storage and Conversion," *Chemical Society Reviews* 49, no. 8 (2020): 2378–2407.

104. Y. Q. Lin, L. H. Zhang, Y. Xiong, T. Wei, and Z. J. Fan, "Toward the Design of High-Performance Supercapacitors by Prussian Blue, Its Analogues and Their Derivatives," *Energy & Environmental Materials* 3 (2020): 323–345.

105. E. S. Goda, S. Lee, M. Sohail, and K. R. Yoon, "Prussian Blue and Its Analogues as Advanced Supercapacitor Electrodes," *Journal of Energy Chemistry* 50 (2020): 206–229.

106. J. Y. Xing, Y. S. Zhang, Y. Jin, and Q. Z. Jin, "Active Cation-Integration High-Entropy Prussian Blue Analogues Cathodes for Efficient Zn Storage," *Nano Research* 16, no. 2 (2023): 2486–2494.

107. Y. Shi, B. Yang, G. Song, et al., "Intelligent Synthesis of Nano Prussian Blue Analogue Based Hybrids for High Performance in Lithium-Ion Batteries," *Science China-Chemistry* 68, no. 9 (2025): 4194–4204.

108. B. Li, P. Gu, G. X. Zhang, et al., "Ultrathin Nanosheet Assembled Sn0.91Co0.19S2 Nanocages with Exposed (100) Facets for High-Performance Lithium-Ion Batteries," *Small* 14, no. 5 (2018): 1702184.

109. J. W. Liu, D. X. Xie, W. Shi, and P. Cheng, "Coordination Compounds in Lithium Storage and Lithium-Ion Transport," *Chemical Society Reviews* 49, no. 6 (2020): 1624–1642.

110. X. L. Gao, Y. H. Zheng, J. Chang, et al., "Universal Strategy for Preparing Highly Stable PBA/Ti3C2Tx MXene toward Lithium-Ion Batteries via Chemical Transformation," *ACS Applied Materials & Interfaces* 14, no. 13 (2022): 15298–15306.

111. Y. F. Cai, B. Qin, J. H. Lin, et al., "Self-Assembly Lightweight Honeycomb-Like Prussian Blue Analogue on Cu Foam for Lithium Metal Anode," *ACS Applied Materials & Interfaces* 13, no. 20 (2021): 23803–23810.

112. S. Q. Feng, J. F. Wang, N. S. Gao, J. F. Wen, X. Y. Li, and J. R. Xiao, "Heterogeneous Interface of Ni-Mn Composite Prussian Blue Analog-Coated Structure Modulates the Adsorption and Conversion of Polysulfides in Lithium-Sulfur Batteries," *Electrochimica Acta* 433 (2022): 141218.

113. X. X. Chen, S. Y. Zeng, H. Muheiyati, et al., "Double-Shelled Ni-Fe-P/N-Doped Carbon Nanobox Derived From a Prussian Blue Analogue as an Electrode Material for K-Ion Batteries and Li-S Batteries," *ACS Energy Letters* 4, no. 7 (2019): 1496–1504.

114. M. Du, P. B. Geng, C. X. Pei, et al., "High-Entropy Prussian Blue Analogues and Their Oxide Family as Sulfur Hosts for Lithium-Sulfur Batteries," *Angewandte Chemie-International Edition* 61, no. 41 (2022): e202209350.

115. M. Du, X. Y. Wang, P. B. Geng, et al., "Polypyrrole-Enveloped Prussian Blue Nanocubes with Multi-Metal Synergistic Adsorption toward Lithium Polysulfides: High-Performance Lithium-Sulfur Batteries," *Chemical Engineering Journal* 420 (2021): 130518.

116. X. C. Jiao, J. Hu, Y. Z. Zuo, J. Qi, W. Yan, and J. J. Zhang, "Self-Recovery Catalysts of ZnIn2S4@In2O3 Heterostructures with Multiple Catalytic Centers for Cascade Catalysis in Lithium-Sulfur Battery," *Nano Energy* 119 (2024): 109078.

117. Z. Liu, B. Li, H. Xu, et al., "Synergistic Effect of Multi-Metallic and Dual-Functional Groups of a MOF@rGO Layer for the Catalytic Transfer and Shuttle Inhibition of Lithium-Sulfur Batteries," *Chemical Communications* 61, no. 83 (2025): 16258–16261.

118. S. Kim, K. Yang, K. W. Yang, M. De Volder, and Y. Lee, "Permselective Ionic-Shield for High-Performance Lithium-Sulfur Batteries," *Nano Letters* 23, no. 22 (2023): 10391–10397.

119. T. B. Huang, Y. B. Niu, Q. J. Yang, W. T. Yang, and M. W. Xu, "Self-Template Synthesis of Prussian Blue Analogue Hollow Polyhedrons as Superior Sodium Storage Cathodes," *ACS Applied Materials & Interfaces* 13, no. 31 (2021): 37187–37193.

120. B. Kuang, W. Feng, Y. Shi, et al., "Balance Control of Capacity and Stability of the Bimetallic Prussian Blue Cathode for High-Performance Sodium-Ion Batteries," *Inorganic Chemistry* 64, no. 30 (2025): 15392–15401.

121. L. X. Shen, Y. Jiang, Y. Jiang, et al., "Monoclinic Bimetallic Prussian Blue Analog Cathode with High Capacity and Long Life for Advanced Sodium Storage," *ACS Applied Materials & Interfaces* 14, no. 21 (2022): 24332–24340.

122. P. Hu, W. B. Peng, B. Wang, et al., "Concentration-Gradient Prussian Blue Cathodes for Na-Ion Batteries," *ACS Energy Letters* 5, no. 1 (2020): 100–108.

123. A. J. Zhou, W. J. Cheng, W. Wang, et al., "Hexacyanoferrate-Type Prussian Blue Analogs: Principles and Advances Toward High-Performance Sodium and Potassium Ion Batteries," *Advanced Energy Materials* 11, no. 2 (2021): 2000943.

124. Y. X. Huang, L. Z. Zhao, L. Li, M. Xie, F. Wu, and R. J. Chen, "Electrolytes and Electrolyte/Electrode Interfaces in Sodium-Ion Batteries: From Scientific Research to Practical Application," *Advanced Materials* 31, no. 21 (2019): 1808393.

125. J. Peng, Y. Gao, H. Zhang, et al., "Ball Milling Solid-State Synthesis of Highly Crystalline Prussian Blue Analogue Na2-xMnFe(CN)6 Cathodes for All-Climate Sodium-Ion Batteries," *Angewandte Chemie-International Edition* 61, no. 32 (2022): e202205867.

126. B. X. Xie, L. G. Wang, H. F. Li, et al., "An Interface-Reinforced Rhombohedral Prussian Blue Analogue in Semi-Solid State Electrolyte for Sodium-Ion Battery," *Energy Storage Materials* 36 (2021): 99–107.

127. G. Song, Y. Shi, B. Yang, Y. Yang, and H. Pang, "Unsaturated Coordination Co-BDC Nanosheets with Numerous Potential Binding Sites for Sodium Ions," *Inorganic Chemistry* 64, no. 12 (2025): 6265–6274.

128. Y. Xu, J. Wan, L. Huang, et al., "Dual Redox-Active Copper Hexacyanoferrate Nanosheets as Cathode Materials for Advanced Sodium-Ion Batteries," *Energy Storage Materials* 33 (2020): 432–441.

129. M. W. Jiang, Z. D. Hou, J. J. Wang, L. B. Ren, Y. Zhang, and J. G. Wang, "Balanced Coordination Enables Low-Defect Prussian Blue for Superfast and Ultrastable Sodium Energy Storage," *Nano Energy* 102 (2022): 107708.

130. H. Cheng, H. Xu, J. Shang, et al., "Simultaneous Tailoring of Chemical Composition and Morphology Configuration in Metal Hexacyanoferrate for Ultrafast and Durable Sodium-Ion Storage," *Angewandte Chemie-International Edition* 64, no. 2 (2025): e202414302.

131. Z. X. Jing, M. Mamoor, L. T. Kong, et al., "Rational Design of Cobalt-Based Prussian Blue Analogues via 3 d Transition Metals Incorporation for Superior Na-Ion Storage," *Angewandte Chemie-International Edition* 64 (2025): e202423356.

132. J. H. Liu, Y. C. Wang, N. Jiang, B. Wen, C. Yang, and Y. Liu, "Vacancies-Regulated Prussian Blue Analogues through Precipitation Conversion for Cathodes in Sodium-Ion Batteries with Energy Densities over 500 Wh/Kg," *Angewandte Chemie-International Edition*, 63, no. 39 (2024): e202400214.

133. X. Z. Zhou, X. M. Chen, W. X. Kuang, et al., "Entropy-Assisted Anion-Reinforced Solvation Structure for Fast-Charging Sodium-Ion Full Batteries," *Angewandte Chemie-International Edition* 63, no. 42 (2024): e202410494.

134. C. Xu, Y. Liu, S. Han, et al., "Rational Design of Aqueous Na Ion Batteries Toward High Energy Density and Long Cycle Life," *Journal of the American Chemical Society* 147, no. 8 (2025): 7039–7049.

135. H. Wu, J. N. Hao, Y. L. Jiang, et al., "Alkaline-Based Aqueous Sodium-Ion Batteries for Large-Scale Energy Storage," *Nature Communications* 15, no. 1 (2024): 575.

136. Y. Wang, J. Liu, N. Jiang, J. Yang, C. Yang, and Y. Liu, "Highly Crystalline Multivariate Prussian Blue Analogs via Equilibrium Chelation Strategy for Stable and Fast Charging Sodium-Ion Batteries," *Small* 20, no. 44 (2024): 2403211.

137. T. Meng, Z. Chen, X. Lai, J. Xing, C. Chen, and D. Sun, "Dehydration Achieving the Iron Spin State Regulation of Prussian Blue for Boosted Sodium-Ion Storage Performance," *Small* 20, no. 46 (2024): 2405822.

138. J. Liu, C. Yang, B. Wen, B. Li, and Y. Liu, "Ultra-Long Cycle of Prussian Blue Analogs Achieved by Equilibrium Electrolyte for Aqueous Sodium-Ion Batteries," *Small* 19, no. 46 (2023): 2303896.

139. W. Wang, Z. Xing, H. Ren, et al., "MnFe Prussian Blue Analogue Open Cages for Sodium-Ion Batteries: Simultaneous Evolution of Structure Morphology, and Energy Storage Properties," *Small* 20, no. 38 (2024): 2402072.

140. B. Yuan, S. Qiao, L. Yuan, B. Chen, and S. Chong, "Zero-Strain Sodium Nickel Ferrocyanide as Cathode Material for Sodium-Ion Batteries with Ultra-Long Lifespan," *Small* 21, no. 1 (2025): 2407570.

141. Y. Liu, S. Fan, Y. Gao, et al., "Isostructural Synthesis of Iron-Based Prussian Blue Analogs for Sodium-Ion Batteries," *Small* 19 (2023): 43.

142. J. Peng, J. Huang, Y. Gao, et al., "Defect-Healing Induced Monoclinic Iron-Based Prussian Blue Analogs as High-Performance Cathode Materials for Sodium-Ion Batteries," *Small* 19, no. 36 (2023): 2300435.

143. M. T. Ahsan, Z. Ali, D. Qiu, Z. Biao, J. J. Wang, and Y. Hou, "A Strategy to Mitigate Jahn Teller Effect of Mn-Rich NASICON Framework for Sodium-Ion Batteries," *Small* 20 (2024): 43.

144. A. Zhou, C. Guo, J. Jiang, et al., "The Pillar Effect of Large-Size Alkaline Ions on the Electrochemical Stability of Sodium Manganese Hexacyanoferrate for Sodium-Ion Batteries," *Small* 19, no. 50 (2023): 2304887.

145. Y. Y. Hu, H. W. Fu, Y. H. Geng, et al., "Chloro-Functionalized Ether-Based Electrolyte for High-Voltage and Stable Potassium-Ion Batteries," *Angewandte Chemie-International Edition* 63, no. 23 (2024): e202403269.

146. Z. Zhang, X. F. Wang, J. C. Zhu, et al., "Electrolyte Design Enables Stable and Energy-Dense Potassium-Ion Batteries," *Angewandte Chemie-International Edition* 64 (2025): e202415491.

147. S. Dhir, J. Cattermull, B. Jagger, et al., "Characterisation and Modelling of Potassium-Ion Batteries," *Nature Communications* 15, no. 1 (2024): 7580.

148. Z. H. Wang, J. Ren, G. Q. Ling, J. J. Guo, Y. K. Lv, and R. P. Ren, "Prussian Blue-Derived Atomic Fe/Fe3C@N-Doped C Catalysts Supported by Carbon Cloth as Integrated Air Cathode for Flexible Zn-Air Batteries," *Advanced Science* 12, no. 1 (2025): 2407631.

149. L. B. Wang, N. B. Liu, Q. Q. Li, et al., "Dual Redox Reactions of Silver Hexacyanoferrate Prussian Blue Analogue Enable Superior Electrochemical Performance for Zinc-Ion Storage," *Angewandte Chemie-International Edition* 64, no. 4 (2025): e202416392.

150. X. K. Zhang, J. W. Zhang, H. X. Yu, et al., "Dual Ion Co-Insertion Induced Spontaneous and Reversible Phase Conversion Chemistry for Unprecedented Zn2+ Storage," *Angewandte Chemie-International Edition* 64, no. 2 (2025): e202414479.

151. Y. Shi, B. Yang, G. Song, et al., "Ambient Synthesis of Vanadium-Based Prussian Blue Analogues Nanocubes for High-Performance and Durable Aqueous Zinc-Ion Batteries with Eutectic Electrolytes," *Angewandte Chemie-International Edition* 63, no. 45 (2024): e202411579.

152. A. Q. Sun, W. Chen, J. Yang, et al., "Layered Double Hydroxides/Prussian Blue Analogs toward Improved Capacitive Performances," *Journal of Colloid and Interface Science* 699 (2025): 138287.

153. Y. Wang, Q. F. Zheng, Y. P. Pang, Y. X. Zhang, T. Yuan, and S. Y. Zheng, "Tailored Core-Shell PW@PB Cathodes for Enhanced Sodium-Ion Battery Stability and Rate Capability," *Journal of Energy Storage* 111 (2025): 115424.

154. Y. Zhang, Q. Li, W. Feng, et al., "Valence Engineering via Polyoxometalate-Induced on Vanadium Centers for Efficient Aqueous Zinc-Ion Batteries," *Angewandte Chemie-International Edition* 64, no. 19 (2025): e202501728.

155. S. Dilwale, P. P. Puthiyaveetil, A. Babu, and S. Kurungot, "Phytic Acid Customized Hydrogel Polymer Electrolyte and Prussian Blue Analogue Cathode Material for Rechargeable Zinc Metal Hydrogel Batteries," *Small* 20, no. 34 (2024): 2311923.

156. Y. Su, Y. Zhang, G. Yuan, et al., "Activation of the Microstructures in Nickel-Based Bimetallic Complexes for Aqueous Batteries," *Science China-Chemistry* 68, no. 7 (2025): 2958–2966.

157. Z. X. Liu, Y. Huang, Y. Huang, et al., "Voltage Issue of Aqueous Rechargeable Metal-Ion Batteries," *Chemical Society Reviews* 49, no. 1 (2020): 180–232.

158. A. I. Komayko, S. V. Ryazantsev, I. A. Trussov, et al., "The Misconception of Mg2+ Insertion into Prussian Blue Analogue Structures From Aqueous Solution," *Chemsuschem* 14, no. 6 (2021): 1574–1585.

159. C. W. Gao, Y. Lei, Y. J. Wei, et al., "Coexistence of Two Coordinated States Contributing to High-Voltage and Long-Life Prussian Blue Cathode for Potassium Ion Battery," *Chemical Engineering Journal* 431 (2022): 133926.

160. Y. Su, Y. Zhang, W. Feng, et al., "Monocarboxylic Acid Structural Analogues Facilitate In Situ Composite of Functional Complexes for Aqueous Batteries," *Angewandte Chemie-International Edition* 64, no. 21 (2025): e202502752.

161. C. Ye, Y. Chen, R. Wang, et al., Ion-Selective Capacitive Deionization Enabled by Codoped Core-Shell Carbon Architectures for Efficient Uranium Recovery," *Inorganic Chemistry Frontiers* (2025): https://doi.org/10.1039/d5qi01520k.

162. Y. X. Zeng, J. Z. Xu, Y. Wang, S. Li, D. Y. Luan, and X. W. Lou, "Formation of CuMn Prussian Blue Analog Double-Shelled Nanoboxes Toward Long-Life Zn-Ion Batteries," *Angewandte Chemie-International Edition* 61, no. 48 (2022): e202212031.

163. Y. C. Su, G. Q. Yuan, J. L. Hu, et al., "Thiosalicylic-Acid-Mediated Coordination Structure of Nickel Center via Thermodynamic Modulation for Aqueous Ni-Zn Batteries," *Advanced Materials* 36, no. 32 (2024): 2406094.

164. B. Cui, Y. Chen, H. Xu, et al., "Bimetallic Synergy and Interlayer π-π Modulation in Nickel-Cobalt Metal-Organic Frameworks Enhancement of the Performance of Nickel-Zinc Batteries," *Science China-Chemistry* (2025): https://doi.org/10.1007/s11426-025-2767-0.

165. Y. X. Zeng, X. F. Lu, S. L. Zhang, D. Y. Luan, S. Li, and X. W. Lou, "Construction of Co-Mn Prussian Blue Analog Hollow Spheres for Efficient Aqueous Zn-Ion Batteries," *Angewandte Chemie-International Edition* 60, no. 41 (2021): 22189–22194.

166. S. K. Chong, J. Yang, L. Sun, S. W. Guo, Y. N. Liu, and H. K. Liu, "Potassium Nickel Iron Hexacyanoferrate as Ultra-Long-Life Cathode Material for Potassium-Ion Batteries with High Energy Density," *ACS Nano* 14, no. 8 (2020): 9807–9818.

167. K. F. Huang, B. H. Qu, X. Shen, et al., "A Novel Asymmetric Diffusion Path for Superior Ion Dynamic in High-Voltage Mg-Based Hybrid Batteries," *Advanced Science* 11, no. 41 (2024): 2406451.

168. Y. N. Liu, J. L. Yang, Z. Y. Gu, et al., "Entropy-Regulated Cathode with Low Strain and Constraint Phase-Change Toward Ultralong-Life Aqueous Al-Ion Batteries," *Angewandte Chemie-International Edition* 63, no. 12 (2024): 2406451.

169. M. W. Cui, Y. L. Zhu, H. Lei, et al., "Anion-Cation Competition Chemistry for Comprehensive High-Performance Prussian Blue Analogs Cathodes," *Angewandte Chemie-International Edition* 63, no. 23 (2024): e202405428.

170. Z. Z. Zhao, W. Zhang, D. Wang, et al., "Ostwald-Ripening Induced Interfacial Protection Layer Boosts 1,000,000-Cycled Hydronium-Ion Battery," *Angewandte Chemie-International Edition* 63, no. 50 (2024): e202414420.

171. Y. Lee, J. Theerthagiri, N. Yodsin, et al., "Mitigating Intraphase Catalytic-Domain Transfer via CO2 Laser for Enhanced Nitrate-to-Ammonia Electroconversion and Zn-Nitrate Battery Behavior," *Angewandte Chemie-International Edition* 63, no. 47 (2024): e202413774.

172. L. L. Feng, N. H. Li, S. Y. Tang, Y. R. Guo, J. Zheng, and X. G. Li, "Photoelectrochemical Performance of Titanium Dioxide/Prussian Blue Analogue Synthesized by Impregnation Conversion Method as Photoanode," *Inorganic Chemistry Communications* 125 (2021): 108349.

173. C. Y. Zhang, J. W. Chen, J. Zhang, et al., "The Activation of Inert NiFe Prussian Blue Analogues to Boost Oxygen Evolution Reaction Activity," *Journal of Colloid and Interface Science* 607 (2022): 967–977.

174. Y. Y. Wang, Y. Wang, L. Zhang, C. S. Liu, and H. Pang, "PBA@POM Hybrids as Efficient Electrocatalysts for the Oxygen Evolution Reaction," *Chemistry-An Asian Journal* 14, no. 16 (2019): 2790–2795.

175. H. G. Xu, C. Zhu, H. Y. Lin, et al., "Oxygen Plasma Triggered Co-O-Fe Motif in Prussian Blue Analogue for Efficient and Robust Alkaline Water Oxidation," *Angewandte Chemie-International Edition* 64 (2024): e202415423.

176. F. Y. Diao, M. R. Kraglund, H. L. Cao, et al., "Moderate Heat Treatment of CoFe Prussian Blue Analogues for Enhanced Oxygen Evolution Reaction Performance," *Journal of Energy Chemistry* 78 (2023): 476–486.

177. L. J. Mao, J. Liu, R. Lin, et al., "Tailoring the Compositions and Nanostructures of Trimetallic Prussian Blue Analog-Derived Carbides for Water Oxidation," *Advanced Science* 11, no. 42 (2024): 2402916.

178. H. Zhang, Q. F. Jiang, J. H. L. Hadden, F. Xie, and D. J. Riley, "Pd Ion-Exchange and Ammonia Etching of a Prussian Blue Analogue to Produce a High-Performance Water-Splitting Catalyst," *Advanced Functional Materials* 31, no. 10 (2021): 2008989.

179. H. Y. Yang, J. X. Liu, Z. L. Chen, et al., "Unconventional Bi-Vacancies Activating Inert Prussian Blue Analogues Nanocubes for Efficient Hydrogen Evolution," *Chemical Engineering Journal* 420 (2021): 127671.

180. M. Zhang, Y. F. Chen, J. N. Chang, et al., "Efficient Charge Migration in Chemically-Bonded Prussian Blue Analogue/CdS with Beaded Structure for Photocatalytic H2 Evolution," *Jacs Au* 1, no. 2 (2021): 212–220.

181. M. Sadangi and J. N. Behera, "Ruthenium-Doped Cobalt Sulphide Electrocatalyst Derived From a Ruthenium-Cobalt Prussian Blue Analogue (RuCo-PBA) for an Enhanced Hydrogen Evolution Reaction (HER)," *Dalton Transactions* 53, no. 15 (2024): 6667–6675.

182. Y. M. Gong, Y. Xu, Y. P. Que, et al., "Prussian Blue Analogues Derived Electrocatalyst with Multicatalytic Centers for Boosting Oxygen Reduction Reaction in the Wide pH Range," *Journal of Colloid and Interface Science* 612 (2022): 639–649.

183. M. Q. Ren, J. C. Lei, J. B. Zhang, B. I. Yakobson, and J. M. Tour, "Tuning Metal Elements in Open Frameworks for Efficient Oxygen Evolution and Oxygen Reduction Reaction Catalysts," *ACS Applied Materials & Interfaces* 13, no. 36 (2021): 42715–42723.

184. X. Y. Meng, J. Y. Yang, C. C. Zhang, et al., "Light-Driven CO2 Reduction over Prussian Blue Analogues as Heterogeneous Catalysts," *ACS Catalysis* 12, no. 1 (2022): 89–100.

185. B. Jin, T. Ouyang, Z. E. Zhang, et al., "Prussian Blue Derived Ca-Fe Bifunctional Materials for Chemical Looping CO2 Capture and in-Situ Conversion," *Separation and Purification Technology* 320 (2023): 123975.

186. K. Singh, G. Li, J. Lee, et al., "Divalent Ion Selectivity in Capacitive Deionization with Vanadium Hexacyanoferrate: Experiments and Quantum-Chemical Computations," *Advanced Functional Materials* 31, no. 41 (2021): 2105203.

187. G. Xu, W. Zhang, G. J. Zhu, et al., "Potential Gradient-Driven Dual-Functional Electrochromic and Electrochemical Device Based on a Shared Electrode Design," *Advanced Science* 11, no. 28 (2024): 2401948.

188. Z.-L. Xie, Y. Zhu, J.-Y. Du, et al., "Reconfiguring the Hydrogen Networks of Aqueous Electrolyte to Stabilize Iron Hexacyanoferrate for High-Voltage pH-Decoupled Cell," *Angewandte Chemie-International Edition* 63, no. 42 (2024): e202400916.

189. X. Shu, D. Tan, Y. Wang, J. Ma, and J. Zhang, "Bimetal-Bridging Nitrogen Coordination in Carbon-Based Electrocatalysts for pH-Universal Oxygen Reduction," *Angewandte Chemie-International Edition* 63, no. 8 (2024): e202316005.

190. Z. W. B. Iton, Z. Irving-Singh, S.-J. Hwang, et al., "Modular MPS3-Based Frameworks for Superionic Conduction of Monovalent and Multivalent Ions," *Journal of the American Chemical Society* 146, no. 35 (2024): 24398–24414.

191. J. Yang, W. Hou, L. Ye, G. Hou, C. Yan, and Y. Zhang, "Vanadium Hexacyanoferrate Prussian Blue Analogs for Aqueous Proton Storage: Excellent Electrochemical Properties and Mechanism Insights," *Small* 20, no. 2 (2024): 2305386.

192. S. Pal, S. Jana, D. K. Singh, V. Ganesan, U. P. Azad, and R. Prakash, "Engineered Ni-Fe Prussian Blue Analogue Nanocubes and Their

Transformation into Nanocages and Mixed Oxide for Applications as Bifunctional Electrocatalyst," *International Journal of Hydrogen Energy* 50 (2024): 52–65.

193. D. Li, S. Xie, H. Dong, et al., "Prussian Blue Analog-Derived FeCo Alloy for Enhanced Alkaline Hydrogen Evolution Reaction," *International Journal of Hydrogen Energy* 87 (2024): 401–408.

194. A. Ren, B. Yu, M. Huang, and Z. Liu, "Encapsulation of Cobalt Prussian Blue Analogue-Derived Ultra-Small CoP Nanoparticles in Electrospun N-Doped Porous Carbon Nanofibers as an Efficient Bifunctional Electrocatalyst for Water Splitting," *International Journal of Hydrogen Energy* 51 (2024): 490–502.

195. Q. Wang, G.-C. Xu, D. J. Liu, H. Ding, and L. Zhang, "Nitrogen-Doped Carbon Confined NiFe-NiFeP Nanocubes Immobilized on Carbon Nanotube as an Efficient Electrocatalyst for Oxygen Evolution Reaction," *International Journal of Hydrogen Energy* 48, no. 34 (2023): 12712–12722.

196. M. Khairy, K. G. Mahmoud, and H. M. El-Sagher, "Amorphization of Nanostructured Prussian Blue Analogues for Boosting Oxygen Evolution Reaction toward Design of Efficient Electrocatalysts," *International Journal of Hydrogen Energy* 48, no. 77 (2023): 29887–29897.

197. Z. H. Su, Z. H. Li, X. J. Yang, X. S. Li, L. Y. Wang, and W. Lu, "In Situ Balanced Synthesis of High-Activity Low-Spin Iron Cathode Prussian Blue for Enhanced Sodium-Ion Storage," *Nano Letters* 25, no. 3 (2025): 957–965.

198. Y. Zheng, Y. Jiao, M. Jaroniec, and S. Z. Qiao, "Advancing the Electrochemistry of the Hydrogen-Evolution Reaction through Combining Experiment and Theory," *Angewandte Chemie-International Edition* 54, no. 1 (2015): 52–65.

199. S. C. Cho, J. H. Seok, H. N. Manh, J. H. Seol, C. H. Lee, and S. U. Lee, "Expanding the Frontiers of Electrocatalysis: Advanced Theoretical Methods for Water Splitting," *Nano Convergence* 12, no. 1 (2025): 4.

200. C. Chen, D. K. Xiong, M. L. Gu, C. X. Lu, F. Y. Yi, and X. H. Ma, "MOF-Derived Bimetallic CoFe-PBA Composites as Highly Selective and Sensitive Electrochemical Sensors for Hydrogen Peroxide and Nonenzymatic Glucose in Human Serum," *ACS Applied Materials & Interfaces* 12, no. 31 (2020): 35365–35374.

201. Y. Huang, D. X. Ye, J. Yang, H. Lu, L. Li, and Y. P. Ding, "A Novel Dual-Signal Molecularly Imprinted Electrochemical Sensor Based on NiFe Prussian Blue Analogue and SnS2 for Detection of p-Hydroxyacetophenone," *Chemical Engineering Journal* 435 (2022): 134981.

202. W. Y. Zhou, R. Sun, S. S. Li, et al., "Engineering Surface Electron and Active Site at Electrochemical Sensing Interface of CN Vacancy-Mediated Prussian Blue Analogue for Analysis of Heavy Metal Ions," *Applied Surface Science* 564 (2021): 150131.

203. Y. Matos-Peralta and M. Antuch, "Review-Prussian Blue and Its Analogs as Appealing Materials for Electrochemical Sensing and Biosensing," *Journal of the Electrochemical Society* 167, no. 1 (2019): 037510.

204. C. J. Zhai, C. K. Xu, Y. P. Cui, L. Wojtas, and W. Q. Liu, "Dynamic Approach to Synthetic Lectin for Glucose with Boosted Binding Affinity through C-H Hydrogen Bonds," *Chemistry-a European Journal* 29, no. 32 (2023): e202300524.

205. Q. Zhang, J. Yan, X. Ma, L. Zhao, P. Song, and L. Xia, "Self-Calibrated Paper-Based Nanoarrays for Background-Free Quantitative Detection of Pesticides Using Self-Assembly and Mask-Assisted Techniques," *Journal of Hazardous Materials* 480 (2024): 136195.

206. Q. Wang, C. Jiao, W. Chen, et al., "Reusable Gallium-Based Electrochemical Sensor for Efficient Glucose Detection," *Biosensors & Bioelectronics* 268 (2025): 116858.

207. D. Jiang, Y. Zhu, Z. Sun, et al., "A Silver Nanowires@Prussian Blue Composite Aerogel-Based Wearable Sensor for Noninvasive and Dynamic Monitoring of Sweat Uric Acid," *Chemical Engineering Journal* 486 (2024): 150220.

208. X. Y. Meng, S. Y. Wang, C. C. Zhang, et al., "Boosting Hydrogen Evolution Performance of a CdS-Based Photocatalyst: In Situ Transition From Type I to Type II Heterojunction during Photocatalysis," *ACS Catalysis* 12, no. 16 (2022): 10115–10126.

209. A. W. Wang, R. Wang, Y. H. Pan, et al., "High Conductive Polymer PANI Link Bi2MoO6 and PBA to Establish "tandem Hybrid Catalysis System" by Coupling Photocatalysis and PMS Activation Technology," *Applied Catalysis B-Environment and Energy* 344 (2024): 123621.

210. M. J. Qiu, F. W. Zhou, P. Sun, X. B. Chen, C. X. Zhao, and W. J. Mai, "Unveiling the Electrochromic Mechanism of Prussian Blue by Electronic Transition Analysis," *Nano Energy* 78 (2020): 105148.

211. Y. An, T. Cai, W. Jiang, T. Lei, and H. Pang, "Research Progress on Photocatalytic Production of Hydrogen Peroxide over MOFs and COFs," *Green Chemistry* 27, no. 35 (2025): 10478–10509.

212. M. Cammarata, S. Zerdane, L. Balducci, et al., "Charge Transfer Driven by Ultrafast Spin Transition in a CoFe Prussian Blue Analogue," *Nature Chemistry* 13, no. 1 (2021): 10.

213. M. Kim, J. H. Park, J. M. Lim, H. Kim, and S. Kim, "Conventional and Photoinduced Radioactive 137Cs Removal by Adsorption on FeFe, CoFe, and NiFe Prussian Blue Analogues," *Chemical Engineering Journal* 405 (2021): 126568.

214. P. Zhang, D. Y. Luan, and X. W. Lou, "Fabrication of CdS Frame-in-Cage Particles for Efficient Photocatalytic Hydrogen Generation under Visible-Light Irradiation," *Advanced Materials* 32, no. 39 (2020): 2004561.

215. J. W. Nai, S. Wang, and X. W. Lou, "Ordered Colloidal Clusters Constructed by Nanocrystals with Valence for Efficient CO2 Photoreduction," *Science Advances* 5, no. 12 (2019): 2375.

216. S. Kosasang, N. Ma, S. Impeng, et al., "Prussian Blue Analogue Glasses for Photoinduced CO2 Conversion," *Journal of the American Chemical Society* 146, no. 26 (2024): 17793–17800.

217. N. S. Peighambardoust, S. S. Akbari, R. Lomlu, U. Aydemir, and F. Karadas, "Tunable Photocatalytic Activity of CoFe Prussian Blue Analogue Modified SrTiO3 Core-Shell Structures for Solar-Driven Water Oxidation," *ACS Materials Au* 4, no. 2 (2023): 214–223.

218. M. Gautam, K. Poudel, C. S. Yong, and J. O. Kim, "Prussian Blue Nanoparticles: Synthesis, Surface Modification, and Application in Cancer Treatment," *International Journal of Pharmaceutics* 549, no. 1–2 (2018): 31–49.

219. Y. H. Wang, Z. H. Liang, Z. Y. Liang, W. F. Lv, M. Chen, and Y. Zhao, "Advancements of Prussian Blue-Based Nanoplatforms in Biomedical Fields: Progress and Perspectives," *Journal of Controlled Release* 351 (2022): 752–778.

220. K. Lu, X. Y. Zhu, Y. Li, and N. Gu, "Progress in the Preparation of Prussian Blue-Based Nanomaterials for Biomedical Applications," *Journal of Materials Chemistry B* 11, no. 24 (2023): 5272–5300.

221. Q. Tang, J. Liu, Y. Jiang, M. N. Zhang, L. Q. Mao, and M. Wang, "*Cell-Selective Messenger RNA Delivery and CRISPR/Cas9 Genome Editing by Modulating the Interface of Phenylboronic Acid-Derived Lipid Nanoparticles and Cellular Surface Sialic Acid. Acs Applied Materials & Interfaces*, 11, no. 50 (2019): 46585–46590.

222. Z. J. Xu, G. T. Liu, Q. Li, and J. Wu, "A Novel Hydrogel with Glucose-Responsive Hyperglycemia Regulation and Antioxidant Activity for Enhanced Diabetic Wound Repair," *Nano Research* 15, no. 6 (2022): 5305–5315.

223. S. Q. Chen, X. N. Yang, Z. Wang, et al., "Prussian Blue Analogs-Based Layered Double Hydroxides for Highly Efficient Cs plus Removal From Wastewater," *Journal of Hazardous Materials* 410 (2021): 124608.

224. F. Guo, Y. Z. Zhang, L. Cai, and L. J. Li, "NiFe Prussian Blue Analogue Nanocages Decorated Magnesium Hydroxide Rod for Enhancing Fire Safety and Mechanical Properties of Epoxy Resin," *Composites Part B-Engineering* 233 (2022): 109650.

225. Y. Jung, U. S. Choi, and Y. G. Ko, "Securely Anchored Prussian Blue Nanocrystals on the Surface of Porous PAAm Sphere for High and Selective Cesium Removal," *Journal of Hazardous Materials* 420 (2021): 126654.

226. J. P. Xie, L. Ma, J. L. Li, et al., "Self-Healing of Prussian Blue Analogues with Electrochemically Driven Morphological Rejuvenation," *Advanced Materials* 34, no. 44 (2022): 2205625.

227. J. Y. Xie and B. Dong, "Hollow and Substrate-Supported Prussian Blue, Its Analogs, and Their Derivatives for Green Water Splitting," *Chinese Journal of Catalysis* 42, no. 11 (2021): 1843–1864.

228. N. Song, S. Y. Ren, Y. Zhang, C. Wang, and X. F. Lu, "Confinement of Prussian Blue Analogs Boxes Inside Conducting Polymer Nanotubes Enables Significantly Enhanced Catalytic Performance for Water Treatment," *Advanced Functional Materials* 32, no. 34 (2022): 2204751.

Biographies

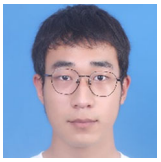

Wu Ke is currently an undergraduate student at the College of Chemistry and Materials Science, Yangzhou University, China, under the supervision of Professor Pang. The main research direction is based on metal-organic frameworks (MOFs) and their applications in electrochemistry and energy.

Guangxun Zhang is now a graduate student under Professor Pang' s supervision, Yangzhou University of chemistry and chemical engineering, China. His research mainly focuses on multifunctional materials based on MOFs and their applications in electrochemistry.

Huan Pang received his Ph.D. degree from Nanjing University in 2011. He is now a distinguished professor at Yangzhou University and a Young Changjiang Scholar of the Ministry of Education in China. He is the managing editor of EnergyChem and the editorial board member of National Science Review, FlatChem and Rare Metals. His research area mainly focuses on MOFs-related materials.